

Propagating Disturbances as a Prestall Instability in Axial Compressors

vorgelegt von
M.Sc.
Mario Eck

an der Fakultät V - Verkehrs- und Maschinensysteme
der Technischen Universität Berlin
zur Erlangung des akademischen Grades

Doktor der Ingenieurwissenschaften
- Dr.-Ing. -

genehmigte Dissertation

Promotionsausschuss:

Vorsitzender: Prof. Dr.-Ing. Julien Weiss
Gutachter: Prof. Dr.-Ing. Dieter Peitsch
Gutachter: Prof. Dr.-Ing. Ronald Mailach

Tag der wissenschaftlichen Aussprache: 25. Juni 2020

Berlin 2020

Acknowledgments

The present work has been written during my employment as a research assistant at the Department of Aero Engines at the Technische Universität Berlin. It is my utmost concern to point out that the majority of the results presented in this thesis has been obtained beyond the regular "day-to-day business" of my employment. In this regard, I am very indebted to my doctoral supervisor, Professor Dieter Peitsch, for giving me the necessary leeway that has contributed significantly to the diversity of this work. His unrestricted support is reflected in particular in the funding of many "spin-off projects", which have enriched this work.

I feel especially honored of being a member of a group of wonderful people who were passionately committed to the topic "Flow induced acoustics in turbomachinery - the Rotating Instability". I am indebted to Benjamin Pardowitz, Christian Beselt, Julija Peter, Lars Enghardt and Paul-Uwe Thamsen for paving the way for my thesis. I look back with great satisfaction on the time we spent together.

I sincerely appreciate the tremendous support and kindness of my dear colleagues Jan Mihalyovics, Alexander Heinrich, Christine Tiedemann, Christian Brück, Dirk Wieser and Maximilian Jüngst. Thank you for having me as your friend. Roland Rückert deserves special mention for his creative spirit and his enthusiastic dedication, which opened up perspectives that have given this work a special impetus. I was a winner of being the supervisor of your master thesis.

I am deeply indebted to my whole family for unexceptionally giving me the emotional support necessary to make the present work possible. Thank you for accepting me for who I am.

It is my great concern to address the utmost appreciation to Marc. You are not only my closest friend, but also my greatest supporter and the most valued critic of my work. By joining me on stunning motorcycle tours across Europe and most recently California, you have made the past decade a joy. You are truly my brother from another mother.

Kurzfassung

Die vorliegende Arbeit befasst sich mit der experimentellen Analyse von aerodynamischen Instabilitäten in Axialverdichtern. Eine besonders effektive Maßnahme zur Steigerung der Triebwerkseffizienz sowie zur Minderung von Lärmemissionen ist die Vergrößerung des Nebenstromverhältnisses. Bei modernen Flugzeugtriebwerken spiegelt sich diese Maßnahme sehr deutlich durch wachsende Fandurchmesser und kompaktere Kerntriebwerke wider. Baubedingt wachsen dadurch unvermeidlich die relativen Spalte zwischen den Schaufelspitzen der Verdichterschaukeln und der angrenzenden Seitenwand. Aus diesem Grund ist anzunehmen, dass ein besonders komplexes, instationäres Strömungsphänomen, die Rotierende Instabilität (RI), eine größere Rolle bei der Entwicklung zukünftiger Axialverdichter spielen wird. Es ist inzwischen allgemein bekannt, dass die RI eine Vorstufe einer Verdichterinstabilität darstellt. Bezugnehmend auf diese Erkenntnis soll die vorliegende Arbeit das Potential der RI zur präzisen Früherkennung von Verdichterinstabilitäten verdeutlichen, indem die sich während des Drosselprozesses verändernden Merkmale der RI systematisch und zielführend ausgewertet werden. In diesem Zuge leistet diese Arbeit einen erheblichen Beitrag zur Verbesserung des Verständnisses über die strömungsphysikalischen Eigenschaften der RI.

Die experimentellen Versuche wurden an zwei komplementären Verdichterprüfständen durchgeführt. Mittels wandbündig installierter Druckmesstechniken wurde das Strömungsfeld im Nabenspalt eines Verdichterstators sowie im Gehäusespalt eines Verdichterrotors untersucht. Zeitlich und räumlich hoch aufgelöste, ebene Druck- und Geschwindigkeitsfelder erlauben eine detaillierte Analyse des Ausbreitungsortes von kohärenten Strukturen, welche zweifelsfrei der RI zugeschrieben werden konnten. Im Zuge der Untersuchungen konnte eine Vorderkantenablösung als Ursache für jene Strukturen ausgeschlossen werden. Vielmehr bilden sich in der Scherschicht zwischen der Haupt- und der Spaltströmung diskrete Störungen aus, welche sich in Umfangsrichtung fortbewegen. Die Anzahl dieser über den Umfang verteilten Störungen, welche einer Umfangsmoden der RI entspricht, ändert sich stochastisch. Es konnte jedoch festgestellt werden, dass die Umfangsmoden unterschiedliche Wahrscheinlichkeiten aufweisen, wobei diejenige Mode mit den größten Druckamplituden am häufigsten auftritt. Darüber hinaus zeigt diese Arbeit erstmalig Ergebnisse über die Ausbildung der RI in exzentrischen Rotoren.

Schlagwörter:

Axialverdichter, Verdichterinstabilität, Rotierende Instabilität, Rotierende Ablösung, Schaufelspitzenspalt, Rotorexzentrität

Abstract

The present work deals with the experimental analysis of aerodynamic instabilities in axial compressors. A very effective measure for increasing engine efficiency and reducing noise emissions is to increase the bypass ratio. In modern aircraft engines, this measure is clearly reflected by increasing fan diameters and more compact core engines. This trend inevitably causes the relative gaps between the compressor blade tips and the adjacent side wall to grow. For this reason, a highly complex, unsteady flow phenomenon, the Rotating Instability (RI), is to be assumed to play an increasingly important role in the development of future axial compressors. It has been established by now that RI is a prestall phenomenon. Referring to this finding, the present thesis aims at clarifying the potential of RI as a stall precursor by systematically evaluating the characteristics of RI changing during the throttling process. In this context, this work makes a significant contribution in improving the fundamental understanding of the flow physics of RI.

The experiments have been carried out at two complementary compressor test facilities. The flow field in a hub clearance gap of a compressor stator and the tip clearance gap of a compressor rotor has been investigated using pressure measurement techniques installed flush with the surface. By means of temporally and spatially highly resolved pressure and velocity patterns, a comprehensive picture of the propagation area of coherent structures undoubtedly to be attributed to RI could be obtained. In the course of the investigations a leading edge separation could be excluded as the physical cause for those structures. Rather, discrete disturbances are seen to form in the shear layer between the main and the clearance flow while propagating in circumferential direction. The circumferential count of disturbances corresponding to the mode order of RI, changes stochastically in time. However, it was found that the predominant modes have different probabilities, with the mode inducing largest pressure amplitudes occurring most frequently. In addition, this work shows results on the formation of RI in eccentric rotors, which are the first of their kind.

Keywords:

Axial compressor, compressor instability, Rotating Instability, rotating stall, tip clearance, stall inception, rotor eccentricity

Contents

Abbreviations and symbols	ix
List of Figures	xi
List of Tables	xv
1 Introduction	1
2 Literature Review	5
2.1 Introduction to Compressor Performance	6
2.2 Stall Cell Structure	8
2.3 Stall Inception	10
2.3.1 Modal Stall Inception	10
2.3.2 Spike Stall Inception	11
2.4 Rotating Instability	14
2.4.1 Spectral Characteristics of Rotating Instability	17
2.4.2 Flow Physics Associated with RI	19
2.4.3 Rotating Instability in Transonic Compressors	21
2.5 Scope of Present Research	23
3 Stator Experiments	25
3.1 Introduction	26
3.2 Compressor Stator Cascade	26
3.3 Instrumentation	29
3.4 Frequency Analysis	31
3.4.1 Spectral Signature of RI	31
3.4.2 Time-Resolved Properties of RI	34
3.5 Static Pressure Maps on the Hub Wall	36
3.6 Detection of Modal Events	38
3.7 Phase-Averaged Static Pressure Maps	40
3.8 Sublayer Fence Probe	43
3.8.1 Calibration Procedure	44
3.8.2 Flow Angle Detection	46
3.9 Stator Over Tip Flow Maps	49
3.10 Time-Resolved Velocity Flow Maps	51
3.10.1 Methodology of Ensemble Averaged Results	51
3.10.2 The Ensemble Averaged Velocity Flow Map	52
3.10.3 Multi-Passage Velocity Maps for Different Modes	57

3.11	Conclusions	60
4	Rotor Experiments	63
4.1	Research Compressor	64
4.1.1	Instrumentation	67
4.1.2	Data Reduction	68
4.2	Compressor Performance	70
4.3	Inception of Prestall Instability RI	72
4.4	Spectral Characteristics	74
4.4.1	Propagation Speed	76
4.4.2	Study of Circumferential Modes	78
4.5	Effect of Eccentricity on RI	80
4.6	Study of Prestall Disturbances	85
4.7	Statistics of Prestall Disturbances	94
4.8	Rotating Stall - Rotating Instability	97
4.9	Transition Into Stall	103
4.10	Potential for Stall Warning	105
4.10.1	Influence of Rotor Eccentricity	106
4.10.2	Influence of Axial Measurement Position	108
4.11	Conclusions	114
5	Discussion and Recommendation for Future Work	117
A	Appendix	123
A.1	Analysis methods	124
A.1.1	Frequency Analysis	124
A.1.2	Mode Analysis	125
A.1.3	Statistics	125
A.2	Additional figures	127
	Bibliography	131

Abbreviations and symbols

AL	Alarm Level
BPF	Blade Passing Frequency
CN	Clearance Noise
CPM	Computational Preston Tube Method
CSC	Compressor Stator Cascade
DFT	Discrete Frouier Transformation
DP	Design Point
EO	Engine Order
ISA	International Standard Atmosphere
LE	Leading Edge
LG	Large Gap
MEMS	Mirco-Electro-Mechanical Systems
NG	Nominal Gap
OP	Operating Point
PA	Pressures from Axial transducer array
PC	Pressures from Circumferential transducer array
PIV	Particle Image Velocimetry
PR	Pressure Ratio
PSD	Power Spectral Density [mbar ² /Hz]
Q	Vortex Identification Criterion
RI	Rotating Instability
RMS	Root Mean Square
RS	Rotating Stall
SFP	Sublayer Fence Probe
S	Skewness
TCV	Tip Clearance Vortex
TE	Trailing Edge
VIGV	Variable Inlet Guide Vane

β	Flow Angle [°]
ε	Eccentricity [-]
γ^2	Coherence [-]
γ_m	Cross Correlation Coefficient [-]
ν	Kinematic Viscosity [m ² /s]
Ω	Vorticity Tensor [1/s]
ω	Probe Orientation [°]
ϕ	Flow Coefficient [-]

Π	Static-to-Static Pressure Ratio [-]
Ψ	Total-to-Static Pressure Rise Coefficient [-]
Ψ_m	Auto Correlation Coefficient [-]
ρ	Density [kg/s]
τ	Clearance Height [mm]
φ	Circumferential Angle [°]
\dot{m}	Mass Flow Rate [kg/s]
c	Chord Length [mm]
c_1	Inflow Velocity [m/s]
c_p	Pressure Coefficient [-]
d	Hub Diameter [mm]
f	Frequency [1/s]
h	Fence Height [mm]
i	Incidence [°]
k	Propagation Speed [m/s]
m	Mode Order [-]
Ma	Mach Number [-]
N	Rotational Speed [1/s]
p	Pressure [mbar]
R	Radius [mm]
Re	Reynolds Number [-]
S	Strain Tensor [-]
s	Clearance Height [mm]
T	Sequence Length [s]
t	Time [s]
T_t	Total Temperature [K]
u	Circumferential Velocity [m/s]
u_F	Flow Velocity obtained by the SFP [m/s]

List of Figures

2.1	Schematic compressor performance map, adopted by [14] . . .	7
2.2	Rotating stall - compressor performance	8
2.3	Stall cell propagation	9
2.4	Rotating stall in a multistage axial compressor	9
2.5	Modal type stall inception, Camp and Day (1998) [10]	11
2.6	Spike type stall inception, Camp and Day (1998) [10]	12
2.7	Spill forward of the clearance flow	13
2.8	Embryonic spike formation	13
2.9	Leading edge separation	14
2.10	"Blue holes" from Young	15
2.11	Spectral signature of Rotating Instability	16
2.12	RI in a compressor stator	18
2.13	Time-resolved mode amplitudes of RI in a rotor	19
2.14	Radial vortex structures in a compressor stator	20
2.15	Radial vortex structures in a transonic compressor rotor	21
3.1	Rendering of the annular Compressor Stator Cascade (CSC) .	27
3.2	CSC measurement domain	28
3.3	Cascade nomenclature	28
3.4	Hub instrumentation: piezo resistive pressure transducers evenly distributed around the circumference and concentrated array; setup no. 1	29
3.5	Hub instrumentation: Sublayer Fence Probe (SFP) and reference pressure sensor each traversable in circumferential direction, setup no. 2	30
3.6	CSC Fourier transforms as a function of incidence	31
3.7	CSC spectral analysis at high incidence	32
3.8	CSC mode analysis at high incidence	33
3.9	Auto-correlation of time-resolved mode amplitudes	34
3.10	CSC static hub wall pressures at 16 annular positions	35
3.11	CSC RMS and Skewness as a function of incidence	36
3.12	CSC static pressure contour maps as a function of incidence .	38
3.13	Detection of modal events	39
3.14	CSC phase-averaged pressure contour maps	41
3.15	CSC multi-passage pressure contour maps	42
3.16	Geometries of the sublayer fence probe all in [mm]	43
3.17	Frequency response of the SFP	44
3.18	Calibration of the SFP	45

3.19	Linearization approach for the SFP	47
3.20	SFP implementation and vector nomenclature	49
3.21	CSC mean vector fields	50
3.22	CSC phase-averaged streakline pattern	52
3.23	CSC phase-averaged vector fields	54
3.24	CSC vortex identification procedure	57
3.25	CSC multi-passage vector fields	58
4.1	Photographs of the test rig	65
4.2	Measurement domain of the compressor stage	65
4.3	Rotor and stator blade sections; NACA-65 series	66
4.4	Compressor stage over-tip instrumentation	67
4.5	Compressor stage data reduction	69
4.6	Compressor maps	71
4.7	Irregularity, skewness as a function of flow coefficient	73
4.8	Compressor stage Fourier Transforms	74
4.9	Compressor stage spectral analysis - NG	75
4.10	Compressor stage propagation speed of RI	76
4.11	Compressor stage time-resolved annular and axial pressures	77
4.12	Compressor stage mode analysis	79
4.13	Irregularity in an eccentric rotor	80
4.14	Skewness in an eccentric rotor	81
4.15	Compressor stage annular pressures in an eccentric rotor	82
4.16	Fourier Transforms in an eccentric LG rotor	83
4.17	Fourier Transforms in an eccentric NG rotor	84
4.18	Selected Fourier Transforms and circumferential shift of max. amplitudes	85
4.19	Phase-averaged static pressure, irregularity and skewness contour plots on the casing wall (NG)	86
4.20	Fourier Transforms at various axial positions (NG)	87
4.21	Trajectories of min skewness and max irregularity (NG)	88
4.22	Trajectories of min skewness and max irregularity (LG)	89
4.23	Quasi-instantaneous casing static pressure contours (NG)	91
4.24	Detailed propagation mechanism of prestall flow disturbances	92
4.25	Schematic of vortical structure	93
4.26	Variation of circumferential count of prestall disturbances	95
4.27	Statistics of prestall disturbances	96
4.28	Stall cell expansion at different operating points	98
4.29	Stall cell identification using the axial pressures	99
4.30	Stall cell and RI propagation	100

4.31	Redistribution of prestall disturbances interacting with stall cells	101
4.32	Schematic of interaction between stall cell and RI disturbances	102
4.33	Transient stall inception with RI present beforehand	104
4.34	Annular skewness in a concentric LG rotor	107
4.35	Annular skewness in a concentric NG rotor	108
4.36	Annular skewness in an eccentric LG rotor	109
4.37	Annular skewness in an eccentric NG rotor	109
4.38	Axial skewness in a concentric LG rotor	110
4.39	Axial relative skewness in a concentric LG rotor	111
4.40	Axial skewness in a concentric NG rotor	112
4.41	Axial relative skewness in a concentric NG rotor	113
5.1	Schematic illustration of the propagation mechanism of RI . . .	119
5.2	Development of RI while throttling of the compressor	120
5.3	Progression of RI in an eccentric rotor	121
A.1	Passage-to-passage variation	127
A.2	Compressor stage spectral analysis - LG	127
A.3	Quasi-instantaneous casing static pressure contours (LG) . . .	128
A.4	Phase-averaged static pressure contours on the casing wall (LG)	129
A.5	Fourier Transforms at various axial positions (LG)	130

List of Tables

3.1	Design specifications of the high-speed cascade	27
3.2	Propagation speed of circumferential modes	33
4.1	Design specifications of the test rig	66
4.2	Tested rotor configurations	67

1

Introduction

What is the background and motivation of this work and which objectives are derived?

The demand on aero engine manufacturers to assure reliability and safety in flight operation ultimately rests on operation at a safe distance to the stability limit of the compressor. Lowering emissions, however, depends on operation at improved efficiencies which on the contrary are mostly found close to the stability limit. Reducing the safety margin and at the same time guaranteeing aerodynamic instabilities to be avoided at all costs is therefore of major concern for the compressor designers. This need goes hand in hand with an improved understanding of any flow non-uniformity developing shortly before entering into stall.

Considerable amount of studies addressed a new type of prestall instability which turned out to be most likely when the tip gap between the blade tips and the adjacent wall is sufficiently large. This is why the flow phenomenon, also known as "Rotating Instability", is accused of being increasingly relevant if the trend towards smaller engine cores and larger tip clearances continues.

The present work is specifically aimed at improving the fundamental understanding of the flow physics of Rotating Instability (RI). This objective is achieved by experimental investigations carried out in complementary test facilities, a high speed compressor stator with hub clearance and a low speed compressor rotor. The first wind tunnel allows the unsteady flow field within the tip gap to be acquired at high temporal and spatial resolution using a new instrumentation. Results obtained in the stator were subsequently verified by measurements in the rotor. The latter was tested for the first time in a parametric study in which rotor eccentricity in particular was proven to have an effect on the development of RI.

Since RI is developing well before stall inception, it appears to be well suited to warn of an upcoming stall event. Based on this, a new stall warning indicator, also applicable for quantifying the deterioration in tip clearance height through the life time of an engine, will be presented and discussed at the end.

1.0**Structure of Thesis**

Chapter 2 shortly introduces compressor performance first. A literature review provides a context of the present subject by discussing different inception mechanisms of rotating stall before moving on to the current understanding of Rotating Instabilities.

Chapter 3 discusses the high speed compressor stator, instrumentation, data acquisition and methodology used in the first part of the investigations. This chapter additionally includes a newly designed probe for measuring the time-resolved boundary layer flow field on a wall. Data reduction for acquiring the flow vector in magnitude and direction is outlined in detail. The overtip flow field is then investigated based on static pressure contours and velocity flow maps. The results show the transient growth and decay of prestall disturbances.

Chapter 4 presents a parametric study carried out in a compressor stage. Again, the test rig used, overtip instrumentation and data reduction is presented first. Detailed investigations of quasi-instantaneous casing static pressure contours help identify the precise propagation area of prestall disturbances inside the rotor domain during stepwise throttling of the compressor, at transient maneuvers and allowing to track them in an eccentric rotor with a sinusoidal tip clearance. This chapter is closed by presenting a new algorithm for reliable stall warning.

Chapter 5 summarizes the findings from chapter 3 and 4 and discusses the physical mechanism of RI. The present work concludes with an outlook of how the inception of RI can be investigated proposefully.

2

Literature Review

What is important to know in order not to confuse Rotating Instability with Rotating Stall?

Contents

2.1	Introduction to Compressor Performance	6
2.2	Stall Cell Structure	8
2.3	Stall Inception	10
2.3.1	Modal Stall Inception	10
2.3.2	Spike Stall Inception	11
2.4	Rotating Instability	14
2.4.1	Spectral Characteristics of Rotating Instability . . .	17
2.4.2	Flow Physics Associated with RI	19
2.4.3	Rotating Instability in Transonic Compressors	21
2.5	Scope of Present Research	23

The following literature review provides an overview of rotating stall including its inception mechanisms and finally concludes with a prestall phenomenon developing prior to stall. Compressor performance is shortly introduced first to give a general background.

2.1

Introduction to Compressor Performance

The performance map of an axial compressor is composed of several pressure rise characteristics each corresponding to a certain reduced speed $N/\sqrt{T_t}$ (see Fig. 2.1). It basically shows how much pressure rise (or much more commonly represented by the total-to-total Pressure Ratio (PR)) can be achieved at a certain flow rate or corrected mass flow. The working line follows the path of steady operating points at different speeds. While keeping the speed constant, reducing the mass flow leads to an increase in pressure ratio. At the peak of the pressure rise characteristic, continuing the throttling process leads to an abrupt change in the flow pattern - the compressor enters into stall or surge. The line connecting the unique operating points of instability at different rotational speeds is known as the surge line. While surge is known by a flow rate pulsating in axial direction of the compressor, however, rotating stall is associated with a violent oscillation in tangential direction. As a rule of thumb, a compressor attached to a storage volume is most likely suffering from surge whereas a compressor having a short exit duct will primarily stall (Cumpsty (2004) [14]). The surge margin is introduced by keeping a safe distance between the surge line and the working line in order to avoid the risk of crossing the stalling limit especially during transient maneuvers. The distance is a stack-up of different uncertainties due to compressor degradation over life time or manufacturing inaccuracies, just to mention a few.

The following section will mainly focus on rotating stall. Surge is also known for its impact on the structural integrity of the whole machine, certainly even more than rotating stall. However the primary purpose of the present work is to improve the physical understanding of a prestall phenomenon whose features can clearly be put in a class of rotating stall. Following statements about the stalling process are always true for compressors which will stall at a certain flow coefficient or mass flow rate.

1. Stall occurs, in general, at the peak of the pressure rise characteristic (point "A" in figure 2.2 (a)) and will always be accompanied by a sudden drop in pressure rise Ψ and reduction of mass flow ϕ . Taking into account

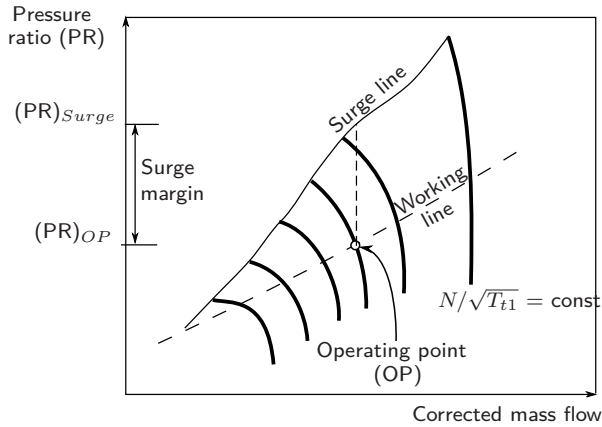


Figure 2.1: Schematic compressor performance map, adopted by [14]

the average flow rate through the compressor to be steady under stalled conditions, the corresponding operating point is located on the stalled branch of the pressure rise characteristic (point "B" in Fig. 2.2 (a)).

2. The flow has a circumferentially non-uniform pattern with clearly defined sectors of stalled and un-stalled flow whereby regions of stalled flow are usually referred to as "cells".
3. Compressor blades with a large aspect ratio (long blades) give rise to multiple part-span cells, short blades usually cause a single full-span stall cell (see Fig. 2.2 (c)).
4. Part-span cells rotate at approximately 50% of the rotor speed, full-span cells rotate more slowly.

Before moving on to the propagation mechanism of stall cells, the author would like to shortly introduce the impact of rotating stall on compressor performance. As mentioned above, entering into stall is accompanied by a sudden loss of pressure rise. A slight drop in overall performance or a smooth transition into stall without any discontinuity in the speed line is sometimes referred to as "progressive stall", whereas "abrupt stall" is indicated by a rapid and very large drop in pressure rise and flow rate (Cumpsty (2004) [14]). In both cases the operating point moves down along the throttle line to settle a new point "B", the un-stalled and stalled sectors operate separately at points "C" and "D" as can be seen in McKenzie's model (1973) in Figure 2.2 b) (Adapted and

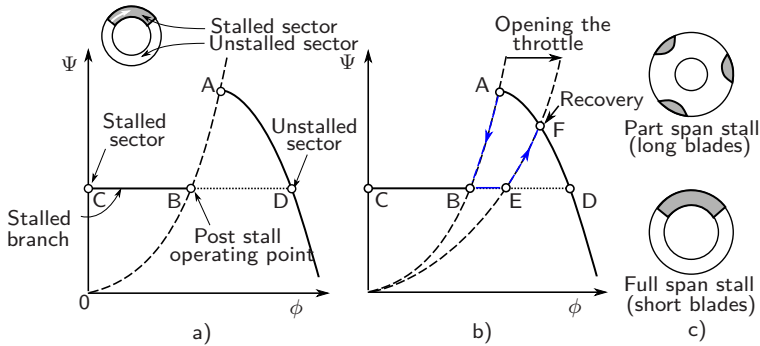


Figure 2.2: a) Operating point at stalled branch; b) hysteresis loop; c) part-span stall and full-span stall, adapted from Day (2015) [16]

extended by [36]). At this point, it is important to mention the "hung stall problem" or better known as the "hysteresis loop". When operating at post stall operation in point "B", opening the throttle will not immediately restore the initial pressure rise on the stable branch of the characteristic (point "A"). The compressor needs to be de-throttled to "E" until the flow recovers in operating point "F". Hence, the mass flow corresponding to the recovery of stable operation is larger than the mass flow at which stall has been initially triggered.

2.2

Stall Cell Structure

The illustration of stalled flow in a single-stage compressor represents an early model of part-span stall (Foley (1951) [23]) (see figure 2.3). Considering the fact that this picture was drawn on an assumption, it is therefore even more impressive that it contains features which later turned out to be valid. Iura and Rannie (1953) [34] noted rotating groups of stalled blades when the entire blade row approaches the "stalling incidence". Emmons et al. (1953) [22] introduced a model for the basic explanation of stall cell propagation in the course of which a famous sketch was drawn (see figure 2.3 upper, right). The illustration is known to be the very first of its kind. The simplicity of this picture seems to be one of the reasons why it is still used today.

At an initial stage of rotating stall the critical blade incidence is approached at discrete blades causing separation and blockage in corresponding passages.

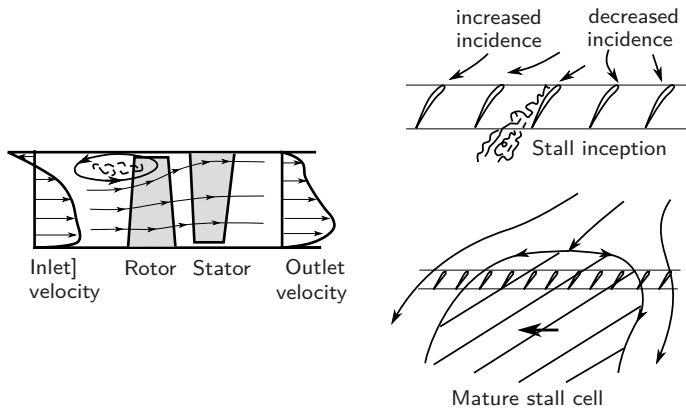


Figure 2.3: Part-span stall [23] and stall cell propagation [22]

McDougall (1988) [46] showed that not only one but several blades might be suffering from this initial process. The resulting blockage forces an increased incidence on the neighboring blade tending it to stall. Therefore, the stall propagates in the direction in which the incidence is increased. A fully developed stall cell covers multiple passages but regarding the propagation mechanism it has a quite similar impact on the incoming flow as the very flow separation involved during stall inception (see figure 2.3, bottom right).

Most models describing the structure of the flow inside a stall cell were based upon suggestions since there was no appropriate measurement technique at hand that was able to record the highly instationary process with sufficiently high temporal resolution.

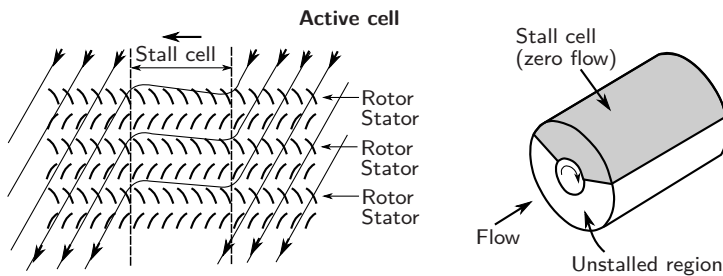


Figure 2.4: Stall cell structure in a multistage compressor [17], schematic adapted from Cumpsty (2004) [14]

An instrumentation addressing this challenge was used by Day and Cumpsty (1978) [17] providing a clear picture of the stall cell structure within a multistage axial compressor. The instrumentation applied was a fast response measurement technique that was revolutionary at the time - namely the hot wire anemometry. They found that the throughflow velocity is almost zero inside the stall cell (see figure 2.4). However, the circumferential component of the velocity might exceed the rotational speed resulting in a highly three-dimensional cell flow.

2.3 Stall Inception

After having introduced a detailed picture of a fully developed stall cell the following section is considering an earlier stage when rotating stall is initiated. For this purpose stall cell formation is tracked back in time shortly before flow separation is evident at any blade. The following literature review answers the question of how this separation is happening in detail and which mechanism is responsible for it. When focussing on the embryonic stage of flow separation, two inception types appeared to stand out, namely the spike-type stall inception and the modal stall inception.

2.3.1 Modal Stall Inception

One route to rotating stall is represented by long length-scale perturbations which occur as harmonical oscillations of the axial through flow. Theoretical work of the 1980's produced models providing evidence of "small amplitude circumferential perturbations" (Hynes and Greitzer (1987) [30], Moore (1983) [39]).

The actual existence of modal disturbances was later verified by McDougall, Cumpsty and Hynes (1990) [43] using six hot-wires equally arranged around the whole annulus (see figure 2.5). Plotting all signals over time allows to track modal disturbances shortly before a stall cell is formed. In this particular case, the mode speed was found to be much lower than the cell speed. These experiments were representing a milestone in the history of stall and surge investigations since purely analytical predictions haven been proven correct for the first time. Moore and Greitzer (1985) [40] found that modal oscillations do not necessarily evolve into a stall cell in their earliest form. However,

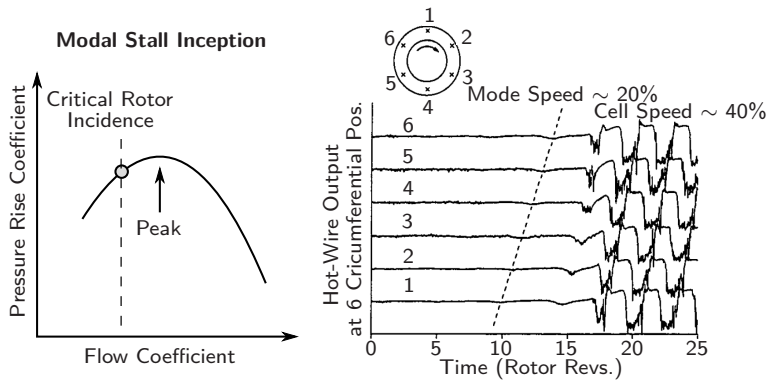


Figure 2.5: Modal type stall inception, Camp and Day (1998) [10]

associated velocity fluctuations increase the local incidence on certain blades and subsequently provoke flow separation when the blade row is operating close to its stalling limit. In general, modal stall inception might be present when the critical incidence is exceeded in the positively sloped part of the pressure rise characteristic (Camp and Day (1998) [10])(cf. Fig. 2.5, left).

2.3.2 Spike Stall Inception

The second stall inception pattern representing one of the most common in aero engine compressors is linked to short length-scale disturbances of large amplitudes. Several decades have passed and many research activities have been carried out until the physics behind these disturbances could be classified which were later referred to as "spike". The term "spike" is based on distinct low pressure spots which have been identified in closest proximity to the leading edge plane during stall inception using unsteady pressure transducers and hot-wire sensors (see figure 2.6). The abrupt formation of spike disturbances were first observed by Jackson (1986) [37]. About 30 years passed from this time until the embryonic spike formation has been widely understood.

During this period of time all proposed mechanisms of spike formation have been associated with blockage growth, critical incidence and forward spillage. From the current point of view each mechanism contains elements of truth. Day et al. (1993) [35] observed earliest signs of spike disturbances in the rotor tip region which is why all subsequently announced mechanisms mainly focused on the tip clearance flow. Suder and Celestina (1995) [42] assumed

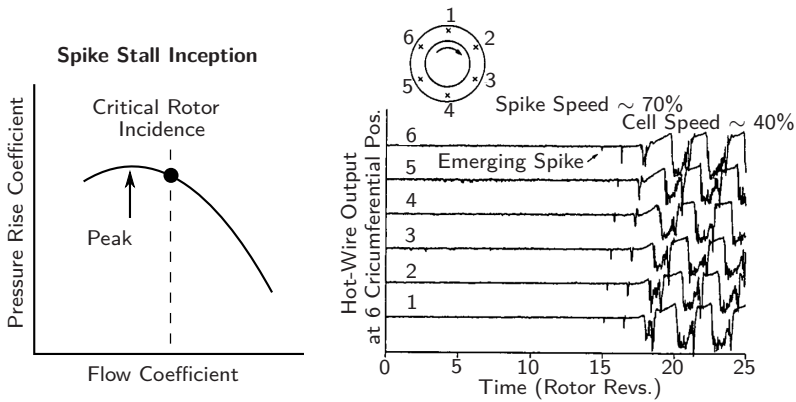


Figure 2.6: Spike type stall inception, Camp and Day (1998) [10]

that the tip leakage vortex causes blockage growth redirecting the incoming flow and consequently increasing the incidence on the blade tip when the rotor is approaching stall. This suggestion seemed to be plausible regarding the fact that the tip clearance vortex in general has the tendency to expand while being shifted towards the rotor inlet plane. The forward movement of the leakage vortex was also addressed in the "forward spillage" hypothesis by Bennington et al. (2008) [1] (cf. Fig. 2.7).

Primary content of this hypothesis is represented by a specific criterion that must be fulfilled for the spike stall inception. Accordingly, the latter occurs when the clearance vortex trajectory is aligned in parallel with the rotor leading edge plane, Hoying et al. (1999) [29]. The characteristic flow pattern appeared to be representing a critical constraint favoring spike stall inception. Later, spillage of the clearance flow around the trailing edge of the neighboring rotor blade ("rearward spillage") was identified as a complementary criterion to be additionally necessary for spike formation, Vo (2001) [60], Vo et al. (2008) [59] and Deppe (2005) [19].

In contrast other studies examined the breakdown of the tip clearance vortex to be involved in the onset of stall (Furukawa (1999) [24] and Schrapp (2008) [57]). Vortex breakdown is featured by an extreme unsteadiness of the flow and it was therefore presumed to be playing a crucial role in the stall inception process.

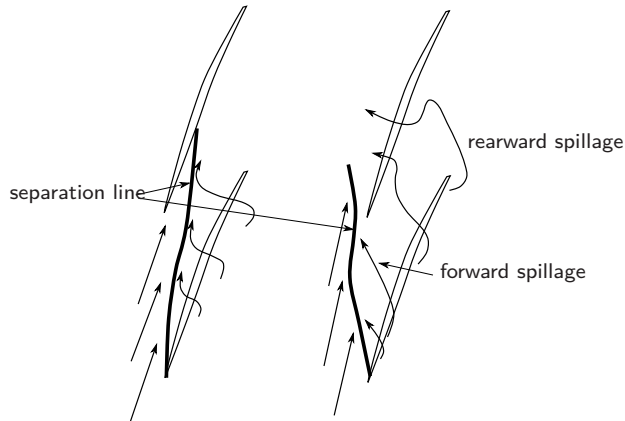


Figure 2.7: Streakline pattern at design conditions (left) and stall (right), Bennington et al. (2008) [1]

Weichert and Day (2014) [62] also found the tip leakage flow to be actually involved in the formation of an embryonic spike. The latter arises when the interface between the reversed clearance flow and the incoming flow becomes destabilized. The process is accompanied by a sudden breakdown of the tip clearance vortex. By this, a small disturbance "A" (see figure 2.8) is recognized by a low pressure spot forming at 10-25% chord just aft of the rotor inlet plane and then propagating towards the neighboring blade. Up to this point no forward spillage of the tip gap flow was present at any passage. It has even been shown that the disturbance arises first and forward spillage of the clearance flow is only present afterwards. Therefore, spillage was found to be rather a consequence of the spike inception process and not the cause of it. Also the low pressure spike has been ascribed to be linked to a radial vortex similar to an "Inoue-vortex" (Inoue et al. (2000) [32], Inoue et al. (2002) [33]).

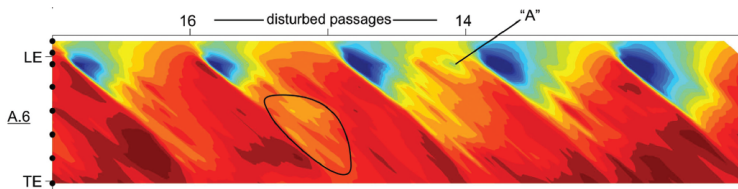


Figure 2.8: Embryonic spike formation (Weichert and Day (2014) [62])

Pullan et al. (2015) [54] disproved that tip clearance flow is necessary for spike formation since a low pressure spot near the leading edges of a compressor blade row was found to be forming without a tip gap and therefore without a clearance vortex present. Numerical simulations revealed the spike to be caused by a leading edge separation (Fig. 2.9, left).

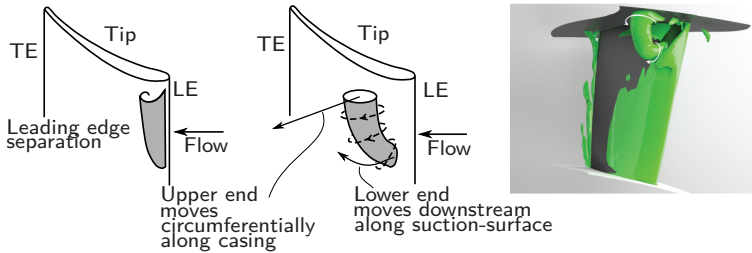


Figure 2.9: Embryonic spike formation (Pullan et al. (2015) [54])

During this process, radial vorticity is shed from the suction side evolving into a discrete vortex filament that spans from the blade suction surface to the casing wall (Fig. 2.9, center and right). While propagating in circumferential direction the nascent disturbance triggers a new separation on the leading edge of the neighboring blade. The pattern subsequently grows in amplitude and length-scale before transitioning into a stall cell. The findings have been additionally verified based upon experimental investigations carried out at the Cambridge Low Speed Compressor [54]. In general, a spike-type route to rotating stall is most likely if the critical incidence is exceeded *before* reaching the pressure rise peak (Camp and Day (1998) [10]) (cf. Fig. 2.5, right).

2.4

Rotating Instability

All of the aforementioned inception mechanisms describe a transitory process which is mostly completed within a few rotor revolutions. This property has been a great challenge for all researchers concentrating on stall warning assessment. Regarding this topic, usefull prestall activity was mainly taken into account when it could be noticed at least hundreds of revolutions before stall onset. One of the earliest studies on stall warning was made by Garnier, Epstein and Greitzer (1990) [26] by identifying prestall modal disturbances. Different corre-

lations and stall warning devices were established over the following 20 years by Inoue et al. (1990) [31], Hoenen and Gallus (1993) [27], Dhingra (2003) [20] and Christensen et al. (2008) [13]. In a work of similar nature, Young et al. (2013) [64] paid attention to the flow pattern behind the unsteadiness of non-repeatability of the blade passing signature which is continuously increasing before reaching the stall limit.

The footprint of "discrete prestall propagating disturbances" has been found by reporting areas of intense low pressure on the casing wall (figure 2.10 b). By this, the low pressure spots turned out to be one of the fundamental reasons for the rise in blade passing irregularity. Furthermore, Young et al. (2013) [64] focused on the level of irregularity affected by the tip clearance height and rotor eccentricity. They found that while increasing tip clearance the ramp-up in irregularity begins earlier and much faster. If the rotor is eccentric, the level of irregularity is highest in that part of the annulus where the clearance is largest.

Young et al. (2013) [64] pointed to another important feature of the unique disturbance pattern clearly observable at stable flow coefficients. The frequency spectrum obtained from pressure measurements on the casing wall shows a broad band peak centered on approximately 30% of the blade passing frequency when the compressor is operating at prestall conditions (figure 2.10 a). The spectral signature turned out to be an important identification feature in one of the most controversially discussed areas of research, namely the "Rotating Instability" (RI).

It is not clear when RI was first noticed. One reason might be the use of different analysis methods exposing different interpretations. In particular the analysis of purely time-resolved pressure data, as it has been practiced over

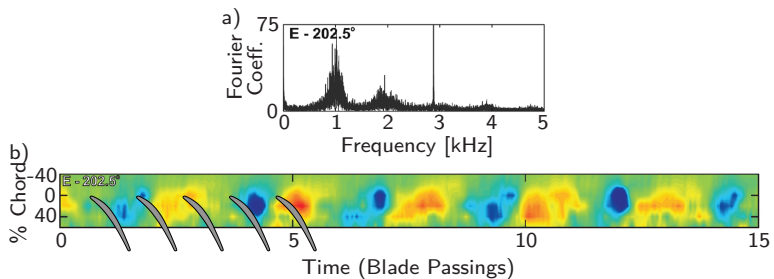


Figure 2.10: Fourier Transformation carried out in a low speed compressor rotor - identification of a broad band peak caused by areas of intense low pressures propagating around the annulus, Young et al. (2013) [64]

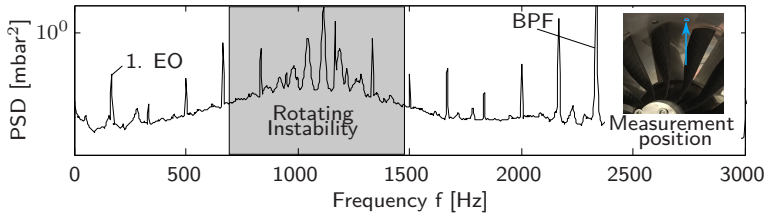


Figure 2.11: Rotating Instability in a compressor rotor - spectral signature of RI at around 35% of the blade passing frequency

many years, may lead to miss important informations which only becomes apparent in the frequency domain. Another reason might be the terminology used, especially taking into account that the term "Rotating Instability" was first used by Kameier in 1995 [41]. However, Mathioudakis and Breugelmann (1985) [45] observed "the simultaneous existence of disturbances of different wavelength" 10 years earlier. Inoue et al. (1990) [31] noted "propagating coherent disturbances" which neither fit the mode nor the spike stall model and which appear in a broad operating range before the compressor falls into stall.

All findings lead to the reasonable assumption that the knowledge about the prestall phenomenon is older than its term "Rotating Instability". Many features of RI have been established over the years. The general findings in this subject can be summarized as follows:

- Rotating Instability occurs when the compressor is operating at off-design conditions. In the earliest stage of RI, the nominally uniform and unstalled flow becomes unstable and transitions into a "prestall condition" which is significantly non-uniform. Meanwhile, the compressor is nominally unstalled.
- The prestall phenomenon RI can be tracked near the gap between the blade tips and the side wall, where RI is more likely to occur with larger tip gaps [4].
- RI can be identified by a broad banded chain of peaks in the frequency spectrum obtained by time-resolved pressure measurements near the rotor blade tips (see figure 2.11). The spectral signature is located at approximately 40% of the blade passing frequency (BPF) [41].

Meanwhile, all statements mentioned above have been accepted by the compressor community. In contrast, explanations on the flow physics causing the

very spectral signature still provide a basis for a lively debate. Early models attempting to explain the physical mechanism of propagating modal perturbations were based upon the unsteadiness of the flow field caused by the breakdown of the tip clearance vortex, Furukawa (1999) [24] or rather the interaction between fluctuating clearance vortices, Mailach et al. (2000) [44].

Later, it was found that these models do not provide a universal description of the formation mechanism of RI since Beselt et al. (2013) [4] proved the unique spectral signature being present in a compressor stator without clearance. The RI pattern could even be found in a shrouded rotor configuration without clearance vortices [51]. This led to a reasonable assumption: It is true that over-tip leakage has an impact on the intensity of pressure fluctuations induced by RI, however, the clearance vortex is not essential for RI's basic formation mechanism. Hence, existing models needed to be reconsidered. The attempt to find a generally valid model was complicated by the fact that RI was additionally found in radial compressors [12, 55] and even in steam turbines [7, 58]. The spectral signature shows a broad banded chain of peaks, each of which can be assigned to a specific wave number of circumferentially distributed pressure fluctuations which have the following properties:

- While running at steady off-design, the predominant flow non-uniformity was found to be characterized by a constantly changing circumferential mode.
- Furthermore, pressure fluctuations of specific modes become briefly amplified within stochastically distributed periods of time. The term "modal event" was introduced to adequately describe the highly unsteady nature of flow patterns with different mode numbers (Pardowitz et al. (2012) [50], Pardowitz et al. (2015) [53]).

Summarizing, the broad banded chain of peaks is linked to propagating disturbances continuously changing in circumferential count (mode numbers) and intensity (modal events).

2.4.1 Spectral Characteristics of Rotating Instability

A major improvement of understanding the spectral properties of RI was achieved by the fundamental support by experts in engine acoustics. The unique methods provided allowed the spectral characteristics of RI to be investigated in a profound way.

A set of pitchwise distributed pressure transducers flush mounted on the side wall above the blade tips is commonly used to prove RI by means of detecting specific features in coherence and phase spectra. The coherence γ^2 allows discrete perturbations to be traced between two sensor positions considered. In contrast to the classical cross-correlation, the coherence answers the question of how much specific frequency components are correlated. Applying the coherence to the data from sensors placed a certain amount of pitch apart, the spectral signature is clearly mirrored in the coherence spectrum. Turning to the phase spectrum, a stepwise slope of the phase distribution is seen to be located in the very frequency range where the spectral signature is present. The unique slope was found to be caused by the modal properties of RI. Exemplary spectra obtained by Pardowitz (2018) [49] in a rotor configuration is shown in figure 2.12. By applying a mode decomposition technique to the data from all pressure transducers, each peak within the spectral signature can be assigned to a certain circumferential mode.

Up to this point, unsteady flow features of RI could only be demonstrated in the frequency domain. Time-resolved properties of specific mode orders can be analyzed by applying a spacial Discrete Fourier Transform (DFT) to the data from a set of circumferentially installed pressure transducers. Depending on the

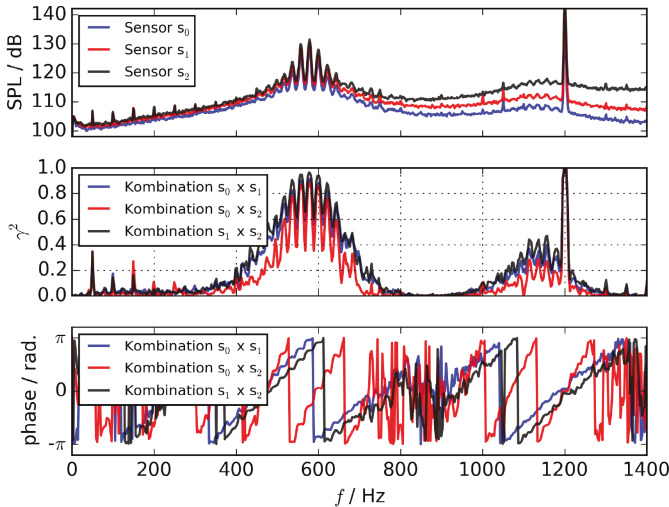


Figure 2.12: Spectral signature of RI obtained in a rotor configuration [49]

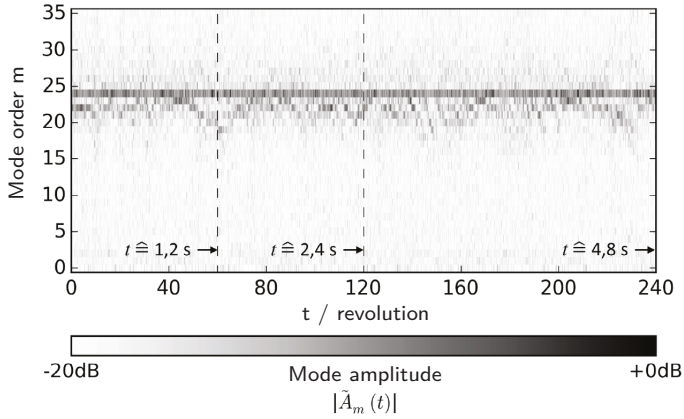


Figure 2.13: Spatial Discrete Fourier Transformation - Time-resolved mode amplitudes of RI in a rotor [49]

mode to be investigated, the DFT produces a continuous time resolved mode amplitude $\tilde{A}_m(t)$. Exemplary mode amplitudes between $m = 0 - 35$ have been processed individually and plotted against rotor revolution (see figure 2.13). It was found that increasing and subsequently decreasing mode amplitudes arise within stochastically distributed periods of time. Taking a specific mode amplitude and applying an autocorrelation to the signal allows to obtain a repeating pattern of characteristic amplitude bursts previously introduced as "modal events". A cross-correlation of an assortment of mode combinations proved modal events of different circumferential modes to be independent of each other.

Comparative measurements in a compressor stator cascade [4, 6] and an axial fan stage [49, 53] confirmed the spectral features identified to be very similar in both configurations. In the rotor, however, the modal flow pattern propagate at a speed 40-50% of the rotor speed. Also, based on measurements in the far field of the rotor it was shown that the interaction between RI and the moving blades might provoke the clearance noise (CN) if the corresponding acoustic mode is capable of propagation.

2.4.2 Flow Physics Associated with RI

Pardowitz et al. (2015) [52] developed a special triggering method allowing to improve the physical understanding of the flow field linked to one specific

peak in the signature. For this purpose, Pardowitz synchronized unsteady pressure measurements and a high speed stereo PIV system. The procedure of collecting data and their post-processing can be split into two steps. In the first step, a spacial Discrete Fourier Transformation (DFT) has been applied to the signals from a set of pressure transducers evenly distributed around the circumference. The results have been auto-correlated to extract the recurring pressure pattern from each modal event. The latter served as reference for the later to come synchronized PIV-pressure-measurements representing the second step. Here, the modal event has been cross-correlated with the data measured by pressure transducers additionally installed to the PIV system. High values of the correlation coefficient indicate the very periods of time at which a modal event is present. Simultaneously recorded data from the PIV setup have been read out at time intervals and then phase-averaged. By doing this, it was possible to visualize the time-resolved 3D flow field associated with a specific mode order as shown in figure 2.14. An alternating acceleration and deceleration of the flow has been observed at the cascade inlet over the entire blade pitch. Radial vortex structures arise within the interfaces between these

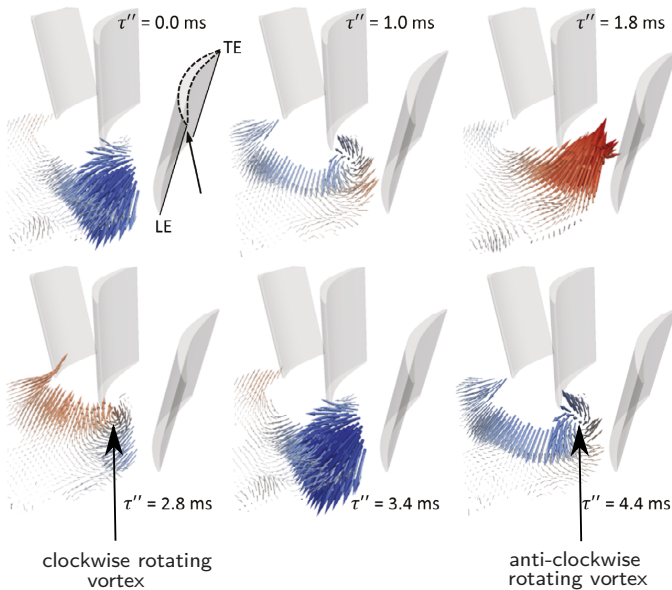


Figure 2.14: Unsteady 3D flow field related to one specific spectral peak in the broadband chain of peaks, Pardowitz et al. (2018) [49]

alternating flow parts, in which a clockwise rotating vortex is followed by an anti-clockwise rotating vortex.

Unfortunately, the limited amount of information from the stator inlet plane prevents the vortices from being properly tracked and their precise origin from being unambiguously located. Also, the cause and effect of the coherent flow structures was not sufficiently addressed in detail. Addressing this is one of the main objectives of the present work.

2.4.3 Rotating Instability in Transonic Compressors

In a work of similar nature to RI, Jüngst et al. (2015) [38] investigated aeroelastic instabilities in a transonic compressor rotor. Rotating pressure fluctuations clearly attributed to RI have been identified by applying Fourier Transforms to the pressure signals measured near the rotor blade tips. Strain gauges imbedded in the rotor blades helped identify structural vibrations in the rotating frame of reference. At stable operating conditions near stall onset, RI was found to be exciting distinct blade vibrations. The reasonable assumption is that RI might induce non-synchronous vibrations due to an aeroelastic coupling between a certain RI-frequency and the natural frequency of the blades. Holtzinger et al. (2015) [28] showed vibrations to be only excited when a specific mode

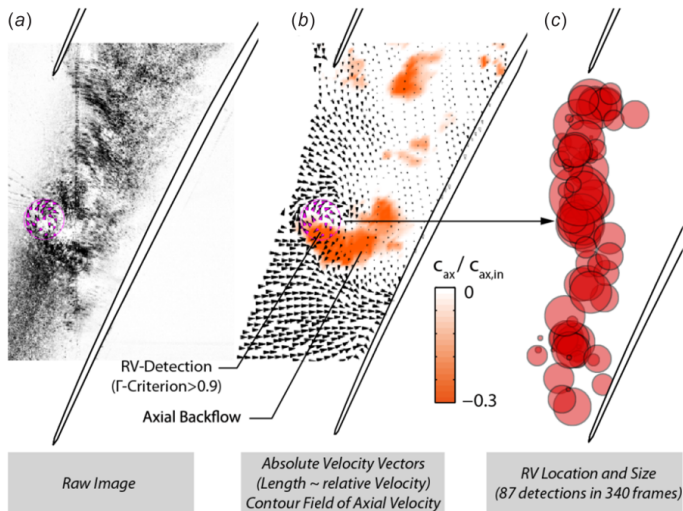


Figure 2.15: PIV measurements in a transonic compressor rotor; detection of radial vortex structures, Brandstetter et al. (2018) [8]

order of RI matches the resonance frequency of the rotor blades. In turn, blade vibrations were found to be capable of having a reverse effect on the aerodynamic fluctuation induced by RI. In general, the investigations are quite unique since the spectral signature found in the transonic compressor rotor is very similar to the one identified in a low speed configuration.

Based upon phase-locked PIV measurements in the vicinity of the rotor blade tips, Brandstetter et al. (2018) [8] proved the existence of radial vortex structures to be located in the front half of the passage and travelling in circumferential direction (see figure 2.15). These vortices arise well before stall onset and they have been linked to blockage associated with tip clearance vortex (TCV) breakdown and forward spilling clearance flow. During throttling, the vortices became locked to increased blade deflections corresponding to the first torsional eigenmode. All findings about coherent flow structures and their impact on non-synchronous vibrations apply for both transonic and subsonic speeds.

2.5 Scope of Present Research

The present work is concerned with improving the physical understanding of the prestall phenomenon RI. Novel instrumentation and methodology are used to achieve this objective in complementary test facilities.

The first wind tunnel is an annular compressor stator cascade allowing to obtain detailed measurements of the unsteady flow field at high spacial resolution in the clearance gap between the blade tips and the adjacent hub wall. During recent investigations it turned out that the compressor stator is prone to suffering from RI when the aerodynamic loading is high. Also, it has been shown that the prestall flow phenomenon is governed by a stochastic process which is why the unsteady behavior of the flow field was misunderstood over a long period of time since the properties of RI were initially suspected to be rather periodically. The examination of distinct flow patterns which need to be tracked first is of particular interest in **chapter 3**.

A special triggering method is used to identify the precise points in time in which the flow field of interest is most pronounced. Knowing the trigger times, additional instrumentation concentrated in the propagation area of RI is then used to examine the phase-averaged flow field in a chronological order. The expedient combination of new instrumentation and methodology used allows much more detail of the prestall flow field to be captured than previously possible.

In **chapter 4**, an axial compressor stage is used to verify the results obtained in the compressor stator amongst additional findings. The studies also serve for approving the phase-averaging methodology used in the compressor stator to be appropriate for investigating the prestall flow field. Current understanding of the flow physics is based on observing flow disturbances exclusively propagating inside the rotor passages. Up to now, the greatest barrier to entirely understand the propagation mechanism from one passage to the next is the lack of information from upstream of the rotor inlet plane. Considering this area is essential in the present work.

A further gain in knowledge is achieved by investigating the RI in an eccentric rotor. By proving the spectral signature absent within the minimum clearance sector, the reasonable conclusion is that the assumptions about a circumfer-

entially closed shear layer being necessary for the formation of RI need to be questioned. Taking into account the findings from stator and rotor experiments, another hypothesis about the inception and the propagation mechanism of RI will be presented.

3

Stator Experiments

Which experiments have been carried out in the annular compressor stator cascade? What are the approaches used to study the major flow structure assigned to a certain mode order of RI? Which measurement technique allows for recording the time-resolved velocity field between the hub wall and the stator blade tips? What is the actual propagation area of coherent flow structures?

Contents

3.1	Introduction	26
3.2	Compressor Stator Cascade	26
3.3	Instrumentation	29
3.4	Frequency Analysis	31
3.4.1	Spectral Signature of RI	31
3.4.2	Time-Resolved Properties of RI	34
3.5	Static Pressure Maps on the Hub Wall	36
3.6	Detection of Modal Events	38
3.7	Phase-Averaged Static Pressure Maps	40
3.8	Sublayer Fence Probe	43
3.8.1	Calibration Procedure	44
3.8.2	Flow Angle Detection	46
3.9	Stator Over Tip Flow Maps	49
3.10	Time-Resolved Velocity Flow Maps	51
3.10.1	Methodology of Ensemble Averaged Results	51
3.10.2	The Ensemble Averaged Velocity Flow Map	52
3.10.3	Multi-Passage Velocity Maps for Different Modes	57
3.11	Conclusions	60

3.1 Introduction

In the past, there has been a lot of confusion surrounding the subject of RI. Although officially accepted by the community as a prestall phenomenon, RI still remains the source of a lively debate. Recent findings about the flow physics of RI obtained in the present stator cascade have been questioned since they were accused of not being adaptable on compressor rotor flows. The following and the subsequent chapter will confirm that not only the spectral signature but the size and the propagation area of prestall flow disturbances are quite equal in the compressor stator and rotor.

An immense effort in post-processing the experimental data is necessary to impressively illustrate the unsteady flow field in that area where the spectral signature of RI is found to be most intense. A miniaturized probe has been designed and calibrated for this study: a so-called sublayer fence probe. This probe and another array of fast response pressure transducers were used to acquire the time-resolved velocity and static pressure fields on the hub wall. In this regard, special attention was devoted to the area upstream of the leading edges.

3.2 Compressor Stator Cascade

The annular compressor stator cascade used in the first part of the present work is a high speed open circuit wind tunnel, as shown in figure 3.1. The test rig is providing a high level of modularity, thus offering many advantages regarding adequate probe access. Of decisive importance is to employ different measurement techniques allowing to obtain the cascade performance and to record the flow field inside the stator blade passage at high temporal and spatial resolution. The major rig features are listed in table 3.1.

A settling chamber equipped with a honeycomb supported gauze filtering any dust and oil particles which might be introduced by the pressure supply system is located upstream of the measurement domain. A nozzle inside the settling chamber is guiding the flow into the 34 mm high parallel annulus where the blades are located. The first blade row is a variable inlet guide vane (VIGV) providing swirl for the downstream compressor stator cascade (CSC). The

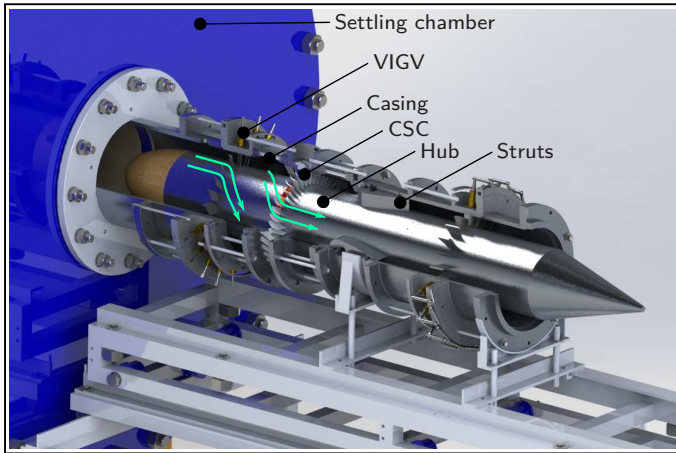


Figure 3.1: Rendering of the annular Compressor Stator Cascade (CSC)

stagger angle of the VIGV can be adjusted to simulate various incidence angles which the stator blades are exposed to further downstream. The CSC is mounted in the casing and a small gap between the stator blade tips and the adjacent stationary hub wall is intended to simulate an unshrouded stator of an embedded stage. The schematic shown in figure 3.2 is illustrating the details

Table 3.1: Design specifications of the high-speed cascade

Casing diameter	240 mm	
Hub diameter	172 mm	
Hub-to-tip ratio	0.717	
Overall length	2 m	
	VIGV	CSC
Blade count	20	20
Chord length	34 mm	34 mm
Stagger (DP)	36°	25°
Flow turning (DP)	45°	30°
deHaller (DP)		0.83
Tip clearance		3% chord
Reynolds number (chord based)		3×10^5
Mach number (CSC inlet)		0.4

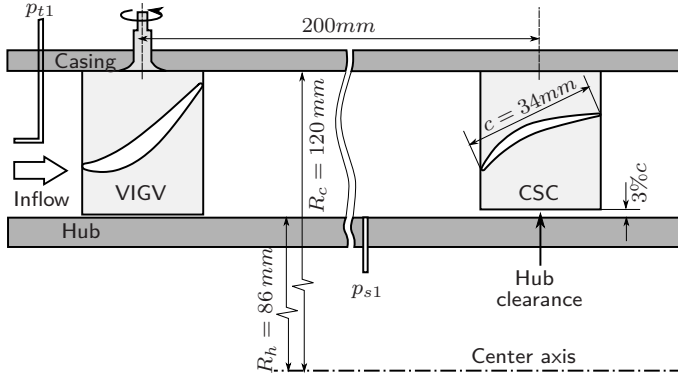


Figure 3.2: Geometry of the measurement domain including the VIGV and the CSC

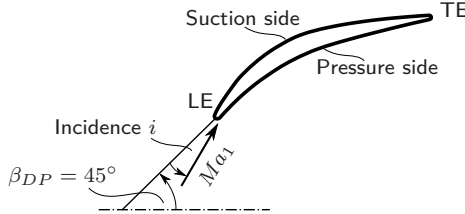


Figure 3.3: Cascade nomenclature

of the measurement domain including instrumentation for adjusting the inflow Mach number to the CSC. Knowing the total pressure loss across the VIGV, the Mach number can be calculated using the isentropic flow equation according to:

$$Ma_1^2 = 2/(\kappa - 1) \left[\left(\frac{p_{t1}}{p_{s1}} \right)^{\frac{\kappa-1}{\kappa}} - 1 \right] \quad (3.1)$$

The incidence angle to the CSC corresponds to the difference between the design inflow angle $\beta_{DP} = 45^\circ$ and the inflow angle obtained at mid span (see figure 3.3). The latter was determined by five-hole probe measurements carried out at 100% axial chord upstream of the CSC leading edges. Further properties of the inflow conditions, e.g. boundary layer thickness on the hub wall and turbulence intensity, can be found in Beselt (2016) [3].

Since the non-moving hub wall does not display a realistic feature of an axial compressor, the Chen-criterion is introduced to approve the clearance flow in

the present case to be still representative [11].

$$C_{chen} = s/c \sqrt{Re} \geq 2.3 \quad (3.2)$$

The criterion is assessing the velocity induced by the pressure difference across the tip gap and compares it to the shear stress induced velocity that would be specifically caused by the relative movement between blades and hub wall. The value of C_{chen} in the present study was about 18 at all times proving the stationary hub wall to be suitable for an appropriate investigation of clearance related secondary flows.

3.3 Instrumentation

Recent experiments carried out in the present CSC have shown that the propagation area of the prestall instability RI is to be located near the hub in closest proximity to the stator inlet plane. The instrumentation split into two different setups is therefore concentrated in that area.

The first setup consists of unsteady pressure transducers installed with the sensing screen being flush mounted with the surface of the hub wall. While 16 sensors are measuring the time-resolved static pressures evenly distributed around the annulus (PC-array), another array of miniature pressure transducers (Kulite sensors) is used to obtain instantaneous static pressure contours covering

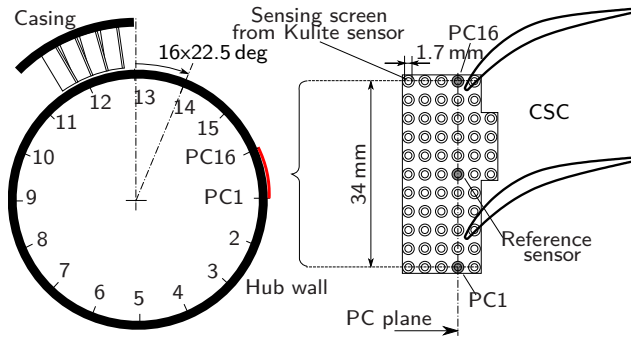


Figure 3.4: Hub instrumentation: piezo resistive pressure transducers evenly distributed around the circumference and concentrated array; setup no. 1

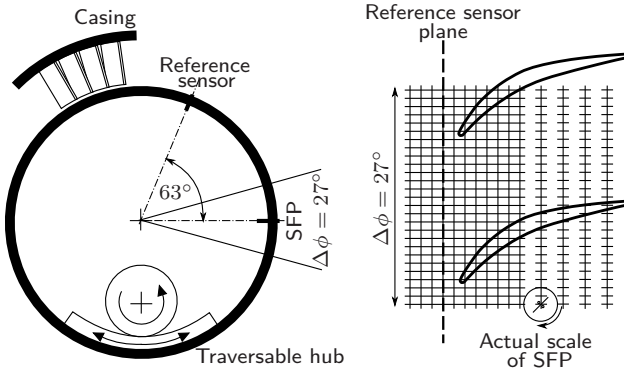


Figure 3.5: Hub instrumentation: Sublayer Fence Probe (SFP) and reference pressure sensor each traversable in circumferential direction, setup no. 2

about one-and-a-half pitches. A detailed arrangement of the transducers is shown in figure 3.4. The signals were sampled at 24 kHz with a low-pass filter set at 10 kHz to avoid aliasing.

The second setup includes a special probe (Sublayer Fence Probe - SFP) which has been designed at the Chair of Aero Engines for measuring the flow velocity near the hub wall. Detailed description of the probe, its calibration procedure and the algorithm to determine the velocity magnitude and direction is given in section 3.7. A custom traverse system installed inside the hub allows the probe to be moved in the circumferential direction covering one-and-a-half pitches by a total of 27 points (see figure 3.5). At each position the probe has been additionally rotated through 360 deg in 20 deg steps (18 probe orientations). In order to take different axial positions into account, the probe needed to be displaced repeatedly. The resulting mesh is covering an axial range between 30% axial chord upstream of the leading edges up to almost passage outlet in 15 steps. Investigating two different operating points of the compressor stator makes a total of 14580 data sets. The SFP has been synchronized with an additional fast response pressure transducer flush mounted in the hub wall near the stator leading edge. While measuring simultaneously, both probes have been moved synchronously in circumferential direction with a constant offset of $\Delta\phi = 63^\circ$. Data from the SFP and the reference probe were sampled at 20 kHz.

3.4 Frequency Analysis

This chapter discusses the fundamental nature of RI based upon frequency analyses applied to the 16 time-resolved static pressures from the circumferential array (setup no. 1). First, the operating range affected by RI can be precisely determined through identifying the unique spectral signature. Most importantly, using the pressures from around the whole annulus allows the modal and time-resolved features of RI to be properly obtained. The latter also serve as a basis for subsequent analysis of the unsteady pressure and velocity field. Detailed description of the data reduction is given in the appendix A.1.1 and A.1.2.

3.4.1 Spectral Signature of RI

The investigated parameter space should first be narrowed to allow the basic physics of RI to be studied in a certain operating point that is indicated by the most pronounced prestall activity. The level of activity is assessed by analyzing the level of pressure amplitudes from the spectral signature. Therefore, the first objective is to provide the signatures for each operating point considered. For this purpose, the Fourier transform has been individually applied to the data from each circumferential sensor and the mean from all spectra was then computed. The results are shown in figure 3.6.

Starting at $i = 10.7^\circ$, a broad peak centered on approximately 300 Hz shows increased pressure amplitudes until evolving into a broad banded chain of

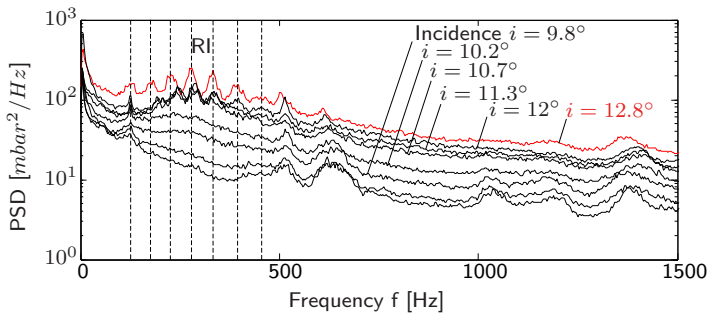


Figure 3.6: Fourier transforms as an average from the 16 circumferential pressures, operating range between design point $i = 0^\circ$ and high incidence $i = 12.8^\circ$, Mach number $Ma_1 = 0.4$

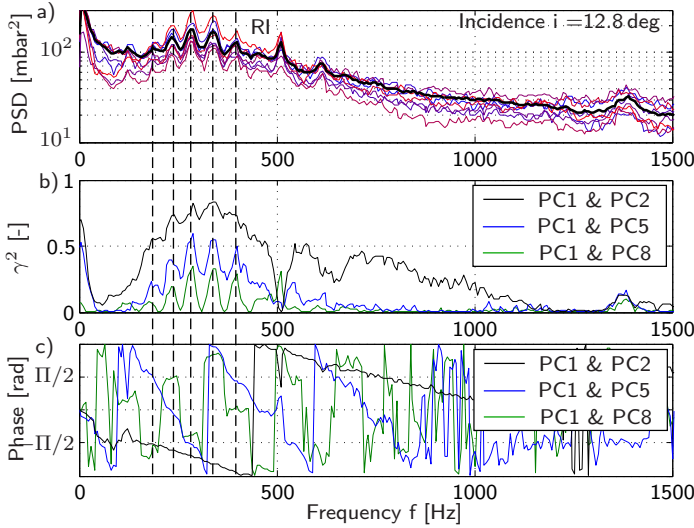


Figure 3.7: Fourier transforms, coherence and phase spectra for three selected sensor combinations from the circumferential transducer array, incidence $i = 12.8^\circ$, Mach number $Ma_1 = 0.4$

peaks from $i = 10.7^\circ$ onwards. As presented in chapter 2 this very signature is typical of this specific type of prestall instability. Hence, the transition into RI appears to be initiated at $i = 9.8^\circ$. Maximum RI amplitudes can be seen at an operating point corresponding to $i = 12.8^\circ$ which is why it has been considered for the following discussions on the flow physics of RI. To confirm the compressor stator to be undoubtedly operating with RI, coherence and phase spectra have been processed for three combinations of sensor pairs having various circumferential offsets. This approach was found to be providing a unique and widely used identification feature of RI as already presented in chapter 2. Fundamentally, the coherence indicates how much two signals are correlated concerning specific frequency components, while the phase spectrum displays the relative phase lag between these components. Results are shown in figure 3.7. Figure 3.7 a) shows each individual spectrum of all 16 circumferential sensors, as well as the averaged spectrum plotted as a solid black line. Turning to figure 3.7 b) the coherence clearly mirrors the aforementioned side-by-side peak signature within the affected frequency range. However, the coherence only exceeds values of 0.6 for the sensor combination installed the closest to each other where the signature comes out most explicitly when the sensors are further apart. This property, also seen by Pardowitz (2018) [49], is basically

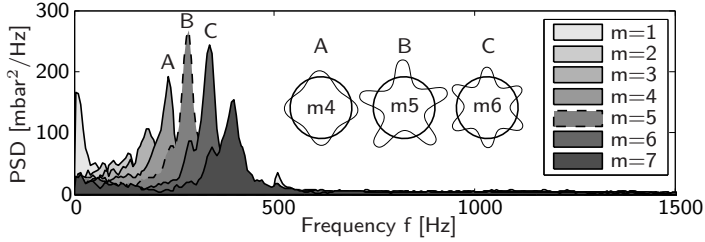


Figure 3.8: Modal pattern of RI with an ascending mode order between $m = 1 - 7$, incidence $i = 12.8^\circ$, Mach number $Ma_1 = 0.4$

indicating disturbances still being tracable while propagating around the annulus. Turning to figure 3.7 c) the phase distribution shows a step-wise slope for the combinations 1-5 and 1-8. This feature was found to be caused by the various circumferential counts of flow disturbances leading to the typical modal pattern of RI. The slope becomes more linear for the sensor combination 1-2 since any wavelength appears to be larger than the circumferential distance between the sensors.

An approach based upon cross spectral matrices considering any signal combination from the annular sensor ring has been used to find the actual circumferential mode pattern of RI (also, see equation A.6 for detailed information on this approach). The 16 evenly distributed sensors allow the modes to be resolved up to mode orders of $m = 7$ as can be seen in figure 3.8. The order of ascending modes is strongly coupled with a rising frequency where the mode of order $m = 5$ is found to be inducing the largest pressure fluctuations. For a better understanding, an exemplary schematic for three selected modes is illustrating how the corresponding modal pressure distributions look at an instant of time. Here, the pressure amplitudes have also been taken into account. Knowing the modal pattern allows to precisely calculate the speed of each mode by

$$k_m = \pi d_{hub} \cdot (f_m/m). \quad (3.3)$$

The speeds k_m summarized in table 3.2 show a slight variation with the mode of order $m = 6$ propagating the slowest. Summarizing, there is not only one

Table 3.2: Propagation speed of circumferential modes

mode m [-]	2	3	4	5	6	7
speed k_m [m/s]	34.85	33.7	31.6	31	30.6	30.7

circumferential count of flow disturbances propagating around the stator annulus but several, whereby one of them stands out to be dominating by inducing largest pressure amplitudes. This very count associated with the mode of order $m = 5$ is now examined in more detail.

3.4.2 Time-Resolved Properties of RI

Another approach allows to study how the modal pressure distribution is changing within a brief period of time. Considering the schematic distributions depicted in figure 3.8, it becomes clear that it is physically impossible for different modes to occur simultaneously. They must alternate over time and the question is how the change is happening in detail. Is there any unique temporal evolution of circumferential modes? Fortunately, an answer to this question can be provided by carrying out a spacial Discrete Fourier Transformation (spacial DFT). Depending on which mode is to be investigated, the output of this approach is a continuous signal whose magnitude is indicating the modal pressure amplitude \hat{A}_m at any specific time t . Applying an auto-correlation to this signal allows for identifying a repeating pattern of time-resolved mode amplitudes. The auto-correlation function $\Psi(t)$ for the dominating mode of order $m = 5$ is shown in figure 3.9.

The harmonical distribution, known as modal event, shows a rising and subsequently decreasing mode amplitude within a time period of about 8 ms . The schematic in the upper part of figure 3.9 serves to illustrate the temporal evolution of the modal pressure distribution. Not only does the amplitude briefly rise,

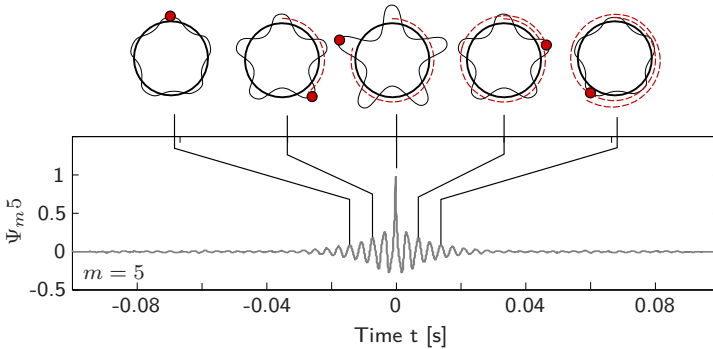


Figure 3.9: Auto-correlation of time-resolved mode amplitudes - "Modal event" of mode order $m = 5$, incidence $i = 12.8^\circ$, Mach number $Ma_1 = 0.4$

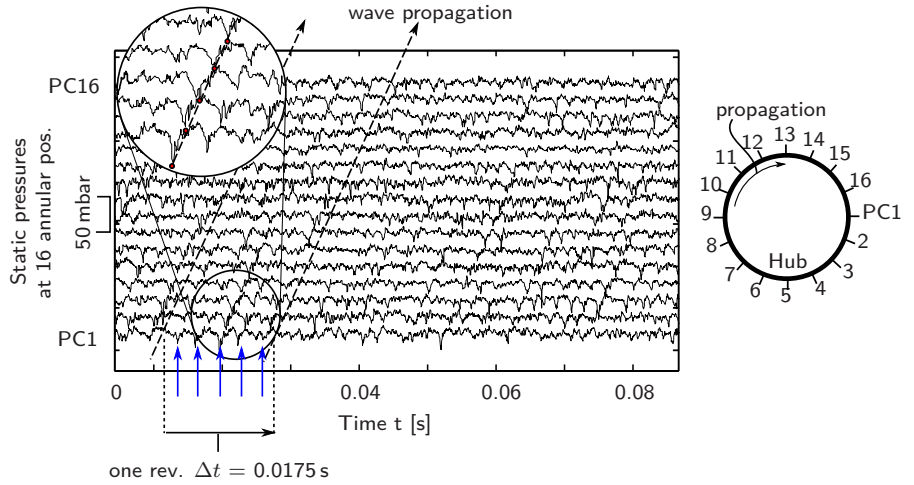


Figure 3.10: Static hub wall pressures at 16 annular positions, incidence $i = 12.8^\circ$, Mach number $Ma_1 = 0.4$

the modal distribution simultaneously moves in the circumferential direction whereby the modal event is completed within approximately two revolutions. Such a property has been found to be also applicable to other modes considered. What modal events all have in common, however, is that they always arise stochastically distributed over time. The phenomenon is neither periodic nor deterministic which is why detecting the actual flow topology associated with a specific circumferential mode of RI is such an ambitious challenge.

In order to get a first insight into the propagation of the discrete perturbations, each trace from the 16 circumferential sensors is plotted over time as shown in figure 3.10. Moreover, tracking the disturbances from one probe position to the next allows the previously estimated wave numbers (mode orders) to be properly confirmed. The dashed lines in figure 3.10 are tracking discrete perturbations travelling from the probe position PC1 towards PC16. The speed of the flow disturbance can be calculated via the hub circumference divided by the period of time the disturbance needs to complete an entire revolution ($\Delta t = 0.0175 \text{ s}$). The propagation speed is

$$k_{m5} = \pi d_{hub} / \Delta t = 30.88 \text{ m/s} \quad (3.4)$$

which is in good compliance with the speed k_{m5} presented in table 3.2. Beyond that, within an exemplary period of time of $\Delta t = 0.0175 \text{ s}$, probe PC1 is

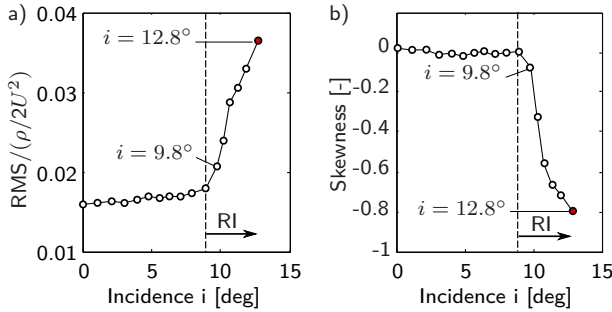


Figure 3.11: Non-dimensionalized root mean square (RMS) and skewness against CSC incidence, Mach number $Ma_1 = 0.4$

detecting a total of five disturbances (highlighted by blue arrows) coinciding with the mode of order $m = 5$ which was also found to be part of the spectral signature in figure 3.8. Also, not only the number of disturbances but also their pressure amplitudes appear to be constantly changing over time. The RI phenomenon is hereby confirmed to be subject to a highly dynamic process.

3.5 Static Pressure Maps on the Hub Wall

Before moving on to the pressure contour obtained by the concentrated sensor array, another approach of assessing the prestall instability is presented first. Based on evidence of increased pressure amplitudes in the spectral signature of RI, the statistical parameter "root mean square" (RMS) is assumed to be appropriately quantifying the intensity of RI as a single number at each operating point considered. For this purpose, the RMS

$$RMS = \sqrt{\frac{1}{N-1} \sum_{i=1}^N [p(t) - \bar{p}]^2} \quad (3.5)$$

has been applied to all data from the PC-array and the mean of all RMS was then non-dimensionalized by the inlet dynamic pressure (see figure 3.11 a). The quantity RMS is used again as "irregularity" throughout the rotor experiments in chapter 4. A clear ramp-up in RMS is seen to be initiated at $i = 9.8^\circ$ precisely coinciding with the inception of RI. At $i = 12.8^\circ$ where RI has been

found to be most pronounced, the pressure fluctuation is almost 4% of the dynamic pressure at inlet. Unsurprisingly, the prestall phenomenon is associated with a certain degree of flow unsteadiness.

More importantly, applying the third statistical moment - the skewness - to the data from the PC-array allows to obtain another property of the pressure fluctuations. Fundamentally, the skewness

$$S = \frac{1}{N} \sum_{i=1}^N \frac{[p(t) - \bar{p}]^3}{RMS^3} \quad (3.6)$$

is assessing as to which degree the probability distribution of a random quantity becomes asymmetric. To put it in the words of an aerodynamicist: In the present case, the skewness becomes negative if the pressure signal has distinct low pressure peaks significantly deviating from the median - the opposite is true for a positive skewness. In figure 3.11 b) the skewness is plotted against the incidence angle. Coinciding with the rise of RMS, the skewness drops below zero at $i = 9^\circ$. If the pressure fluctuation induced by the prestall instability RI was purely harmonic, the skewness would have been zero. Therefore, the flow disturbances propagating from one stator passage to the next are characterized by distinct peaks of low pressures.

In the following, the RMS and the skewness have been applied to each transducer signal from the passage array (cp. figure 3.4) individually to localize the affected regions within the 2D contour and to compare the results obtained for different operating points. The results are shown in figure 3.12 where the incidence is increased from left to right.

Just prior to RI inception, the overall level of RMS is low and the skewness is almost zero across the entire area covered by the sensors. Becoming recognizable for the first time at $i = 10.2^\circ$, a local patch of negative skewness is clearly seen just aft of the stator leading edges. At the same operating point, a narrow trace of slightly increased RMS originating from the leading edge extends in almost circumferential direction. While increasing the incidence angle, the trajectories of both, increased RMS and negative skewness, tend to be shifted slightly in the upstream direction. The flow in this particular region has very properly received considerable study [5, 6] which was summarized by Beselt (2016) [3]. The doctoral thesis provides a large amount of information on the secondary flow mainly developing inside the stator passage. Most importantly, however, his study confirmed the clearance flow to be separating from the hub wall close to the stator inlet plane when the aerodynamic blade loading

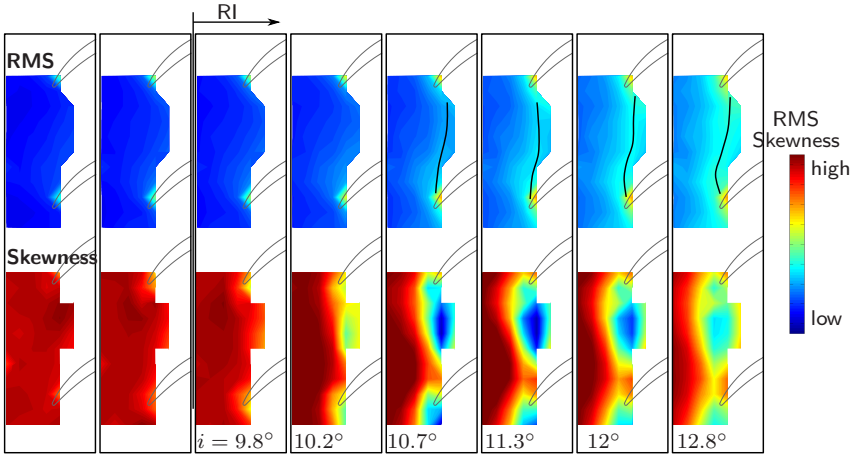


Figure 3.12: Static pressure contour maps of RMS (top) and skewness (bottom) for different operating points, Mach number $Ma_1 = 0.4$

is increased. Starting at $i = 9.8^\circ$ the convergence of the clearance flow and the main flow leads to the formation of a continuous separation line on the hub wall even extending over the whole annulus. A classic spill forward of the clearance flow is accompanied by this process hinting a necessary constraint for the formation of the prestall phenomenon RI. Already proven by Beselt (2016) [3] is the trajectory of increased RMS and negative skewness to be coinciding with the location of the continuous separation line.

3.6

Detection of Modal Events

Up to this point, existing knowledge about RI obtained in the present compressor stator has been successfully reproduced. However, there is a clear need for an improved understanding of the specific flow topology linked to the classical modal events. Taking into account the pure modal event itself representing a strongly simplified and condensed pattern, the precise times need to be sought first in which the pressure field at the cascade inlet shows a maximum correlation to the modal event. The underlying triggering method is adapted from [49] and evaluates a single reference pressure signal measured at the same axial location as the modal event itself has been obtained.

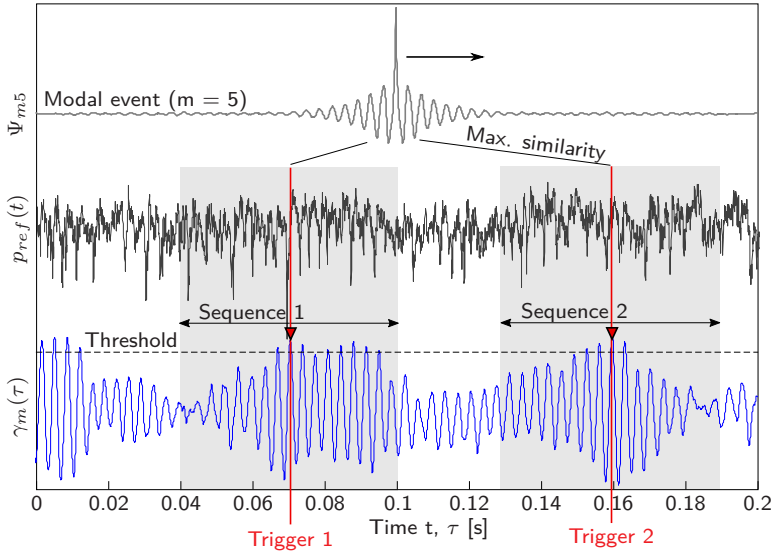


Figure 3.13: Detection of modal events using a single reference pressure signal (measurement location c.f. figure 3.4); Triggering procedure bases upon a cross-correlation between the modal event Ψ_{m5} and the raw reference static pressure $p_{ref}(t)$

In the present case, the reference pressure signal is taken from a pressure transducer placed in the center of the passage array (c.f. figure 3.4). The corresponding time-resolved reference pressure is shown in the center of figure 3.13. For the purpose of triggering, the modal event is basically shifted along the reference signal while both traces are being continuously monitored for a maximum similarity. Mathematically, this comparison is based upon a cross-correlation between $\Psi(t)$ and $p_{ref}(t)$ according to:

$$\gamma_m(\tau) = \lim_{T \rightarrow \infty} \frac{1}{2T} \int_{-T}^T \Psi(t) \cdot p_{ref}(t + \tau) d\tau. \quad (3.7)$$

The correlation coefficient $\gamma_m(\tau)$ is shown in blue in figure 3.13. At the times when the reference signal is most similar to the modal event, the coefficient reaches high values. Detecting these points in times is made possible by introducing a threshold level. Once the correlation coefficient has exceeded the

threshold, a trigger was found. The algorithm is continuously adjusting the threshold level until at least 100 trigger have been found in the signal which has a total length of $T = 20$ seconds. After that, sequences with a length of six milliseconds are defined in the reference signal, each of which is centered around the trigger times. A total of 100 sequences can then be used for phase-averaging of any data simultaneously recorded to the reference signal.

Another constraint in detecting the trigger times includes a minimum distance of 6 milliseconds between each trigger to avoid an overlapping of the sequences. Also, Pardowitz (2018) [49] confirmed the method to be producing sequences that are always in phase.

3.7 Phase-Averaged Static Pressure Maps

Knowing the precise points in time, where the modal event of $m = 5$ is actually present, measurements from the passage array of probes are used to produce phase-averaged static pressure contour maps. This requires the time-resolved static wall pressures to be simultaneously recorded to the reference signal. Since the latter is measured inside the array itself, phase-averaging is therefore even more simplified. Starting from the mode of order $m = 5$ to be dominating in the mode spectrum and turning to the corresponding time-resolved pressure distribution, discrete time steps within the modal event are now considered in the passage array (highlighted by A-J in figure 3.14). The first thing to notice in the pressure contour covering about one-and-a-half stator pitches is a flow structure clearly propagating in circumferential direction from bottom to top. By this, the flow appears to be characterized by alternating negative and positive pressure fluctuations. At the trigger time "D" ($t = 0$ s) a finite disturbance is recognized as a patch of low pressure located on the stator inlet plane. The local pressure minimum is of particular importance since it strongly reminds of the pressure pattern that has been associated with radial vortex structures. While moving towards the leading edge of the neighboring blade (at time step "E"), the discrete flow perturbation has become less distinct since a small fraction appears to be passing downstream through the passage. The lack of information from aft of the leading edges prevents the disturbance to be properly traced inside the passage. Addressing this is one of the challenges addressed by the measurements carried out with the sublayer fence probe.

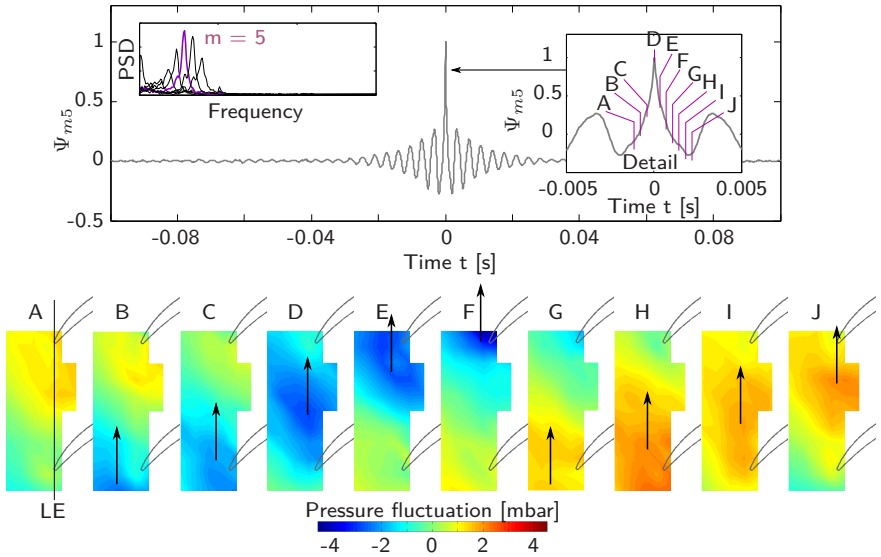


Figure 3.14: Phase-averaged pressure contour maps representing the flow field associated with the modal event of mode order $m = 5$, incidence $i = 12.8^\circ$, Mach number $Ma_1 = 0.4$

By means of analyzing the data across the single passage array, however, it is not possible to conclude a concrete relationship to the mode considered. One approach to overcome this is by producing quasi-instantaneous pressure contours in a multi-passage view. Only then can the circumferential distance between the local disturbances be proven to match the wavelength of the mode. First, using the mode speed obtained in section 3.4 allows to precisely calculate the period of time one disturbance needs to propagate from one passage to the next. Exactly those samples are now taken from the modal event sequence that have the previously calculated time offset. Merging the very single passage pressure contours along the circumferential extend allows to investigate the arrangement of prestall flow disturbances over the whole annulus. The preceding procedure has been repeated for the modes of order $m = 3 - 7$. Figure 3.15 is depicting the quasi-instantaneous pressure contours covering half of the cascade circumference while showing the trigger sample in the center. Only half of the circumference is shown, since the pressure amplitudes decrease considerably towards the edges which is due to the evaluation procedure. Turning to the mode of order $m = 5$, the circumferential spacing of the disturbances is seen to be four stator pitches which makes a total of five disturbances

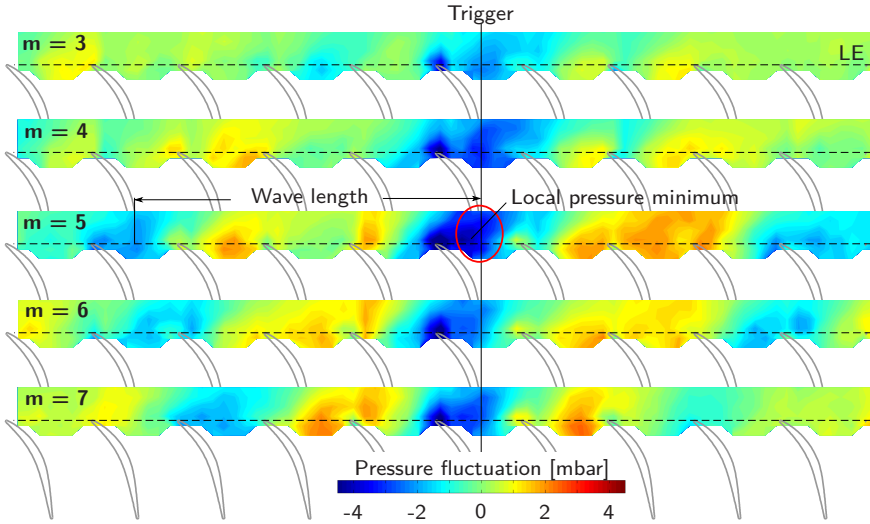


Figure 3.15: 180° static pressure contours on the hub wall for different mode orders $3 < m < 7$, incidence $i = 12.8^\circ$, Mach number $Ma_1 = 0.4$

evenly distributed around the annulus. The higher the mode, the closer the disturbances get to each other, however, the wavelength is always matching the mode order. Thus confirming the triggering method of delivering reliable and representative results. As mentioned in the beginning, when using the characteristic modal pattern to seek for a specific flow component of RI, it must be considered that a modal event produced by phase-averaging is to some extent artificial. However, the phase-averaged pressure contours, even though strongly idealized, can be used to properly investigate the flow physics of RI.

3.8 Sublayer Fence Probe

This section describes an unsteady miniature sublayer fence probe developed at the Chair of Aero Engines of the Technische Universität Berlin. The new probe allows for investigating the clearance flow in a level of detail that was previously hardly to be achieved by means of experimental measurements.

The sublayer fence probe is more commonly used for wall shear stress measurements in a two-dimensional flow. The measurement principle is based on introducing a microscopic obstacle into the boundary layer flow while measuring the static pressures up- and downstream. Here, the pressure difference is ascribed to be proportional to the flow velocity at half the height of the fence chosen to be the characteristic wall distance. Using the similarity law of the viscous sublayer this velocity is linked to the shear stress velocity and therefore to the shear stress itself. This dependency allows the differential pressure to be correlated empirically to the local wall shear stress by means of a calibration curve. The aim of the present work, however, is to measure the flow field close to the hub wall. That is why the aforementioned assumption is re-used to put the measured pressure difference into relation to the flow velocity at half the height of the fence. However, the latter needs to be determined by a reference calibration principle which is described in section 3.8.1.

The probes dimensions are summarized in figure 3.16. General dimensions regarding the pressure tap and fence geometries comply with the design rules for sublayer fence probes given by Nitsche und Brunn (2005) [47]. The circular

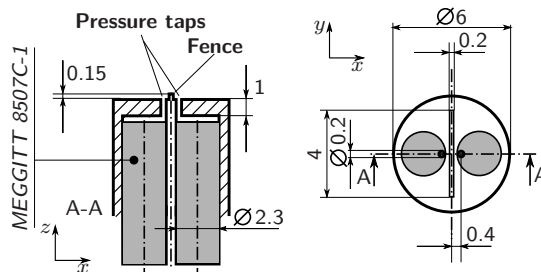


Figure 3.16: Geometries of the sublayer fence probe all in [mm]

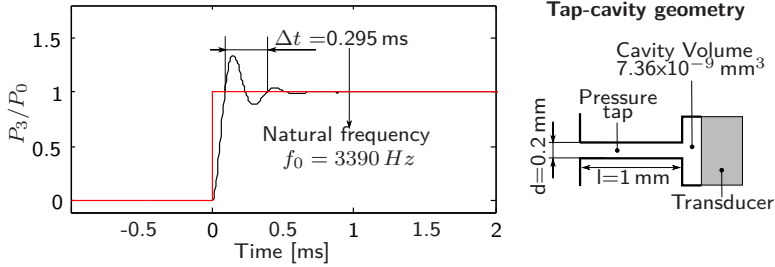


Figure 3.17: Frequency response of the combined pressure tap - cavity volume inside the SFP

probe, 6 mm in diameter, is equipped with a fence of 0.15 mm height. Two pressure taps allow the static pressures on either side of the fence to be captured individually. Each tap is connected to a miniature fast response pressure transducer embedded inside the probe in closest proximity to the measurement position to ensure high temporal resolution of the probes output signal without any dampening volume. To analytically study the frequency response of the probe, the natural frequency of the cavities can be estimated by solving a simplified linear analysis of unsteady pressure measuring systems. Detailed description of the underlying differential equations can be found in Eck et al. (2019) [21]. The resonance frequency of the connecting volume is found to be $f_0 = 3390 \text{ Hz}$ (see figure 3.17) which could be additionally verified by means of using a model assessing the frequency characteristics of a Helmholtz-Resonator. Since the natural frequency is exceeding the frequency to be resolved in the unsteady flow field by a factor of about 11, any post-processed amplification or dampening of the output signal can be excluded.

3.8.1 Calibration Procedure

The sublayer fence probe represents an indirect measuring approach. Therefore, the correlation between the measured differential pressure $\Delta p = p_1 - p_2$ and the flow velocity u_F at a wall distance of $h/2$ needs to be determined empirically and expressed through a calibration curve according to [47]:

$$u_F^+ = A (\Delta p^+)^B ; u_F^+ = \frac{u_F h^2}{4\nu^2}, \Delta p^+ = \frac{\Delta p h^2}{4\rho\nu^2} \quad (3.8)$$

The SFP calibration has been carried out in a high speed wind tunnel equipped with a flat plate. While the probes surface was installed flush mounted to the

surface of the flat plate and the fence positioned perpendicular to the flow, 15 differential pressures have been recorded at various inflow speeds (see figure 3.18 a). The flow velocities at a wall distance of half the height of the fence would then have to be recorded simultaneously using a reference system.

A Preston tube was used for this purpose. Applying the Computational Preston Tube method (CPM method) to the preston tube data allows to numerically obtain the velocity distribution close to the wall. Finally the velocity u_F has to be read out at the wall distance $h/2$. A detailed description of the calibration procedure including the CPM method is given by Eck et al. (2019) [21]. To appropriately take any density and temperature effects into account, the quantities Δp and u_F have been transferred into their non-dimensional form according to equation 3.8. A curve fit delivers the calibration function shown in figure 3.18 a). The average deviation between the regression and the data recorded was found to be less than 0.35%.

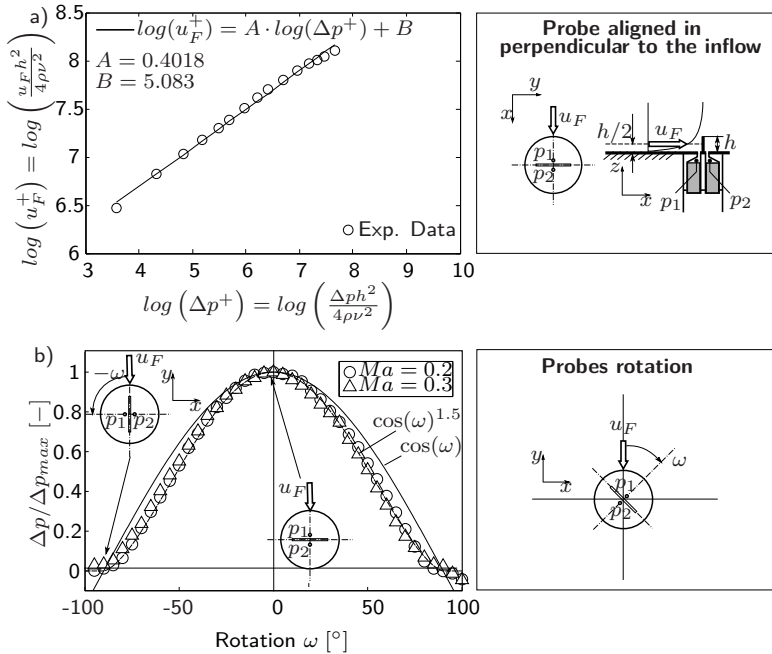


Figure 3.18: Velocity calibration of the SFP; a): non-dimensional fence velocity u_F^+ against non-dimensional pressure difference Δp^+ , b): probe rotation and resulting flow angle characteristic

The characteristic angular distribution shown in figure 3.18 b) can be achieved by rotating the SFP through 360° in 5° steps while keeping the inflow Mach number constant. If the fence is aligned perpendicular to the flow at $\omega = 0^\circ$, the stagnation is most intense and the pressure difference reaches a maximum. At $\omega = \pm 90^\circ$ the differential pressure is zero since the fence has no effect on pressure stagnation. The small deviation between the data and the cosine distribution is not a measurement error, but a quite typical property of the flow angle dependency of this probe type. An accurate approximation, however, can be established by introducing a $\cos^{1.5}$ function.

3.8.2 Flow Angle Detection

To properly obtain the flow angle, one approach would be to rotate the SFP until the very orientation had been found at which the pressure difference reaches a maximum. Since this procedure is not found to be target-oriented, a much more accurate approach is used in the present work. Given an angular dependent distribution at any flow angle β (see figure 3.19 a), the pressure difference Δp can be expressed through:

$$\Delta p = \Delta p_{max} \cos^{1.5}(\beta - \omega) \quad (3.9)$$

Using trigonometry, equation 3.9 can be linearized by transforming the tuplet Δp and ω according to:

$$\frac{\left(\sqrt[3]{\Delta p}\right)^2}{\cos(\omega)} = \left(\sqrt[3]{\Delta p_{max}}\right)^2 \sin(\beta) \tan(\omega) + \left(\sqrt[3]{\Delta p_{max}}\right)^2 \cos(\beta) \quad (3.10)$$

Equation 3.10 is linear in the form: $A = Bx + C$ where

$$A = \frac{\left(\sqrt[3]{\Delta p}\right)^2}{\cos(\omega)} \quad (3.11)$$

$$B = \left(\sqrt[3]{\Delta p_{max}}\right)^2 \sin(\beta) \quad (3.12)$$

$$C = \left(\sqrt[3]{\Delta p_{max}}\right)^2 \cos(\beta) \quad (3.13)$$

$$x = \tan(\omega) \quad (3.14)$$

After transforming the measured quantities (see figure 3.19 b), a linear curve fit applied to the data yields the slope B and the point of interception C . Rearranging the definitions given in equations 3.9 - 3.14 allows to calculate the flow angle β and the maximum pressure difference Δp_{max} .

$$\beta = \arctan(B/C), \Delta p_{max} = \left(\sqrt[4]{\frac{B \cdot C}{\sin(\beta)\cos(\beta)}} \right)^3 \quad (3.15)$$

By applying Δp_{max} to the calibration function depicted in figure 3.18 a), the fence velocity u_F can be finally determined.

Another study was carried out to estimate as to which degree the step resolution in probe orientation $\Delta\omega$ has an effect on the uncertainty in processing the flow angle β . Reducing the amount of orientations is of great concern since it is directly proportional to the measurement time. A trade-off is achieved

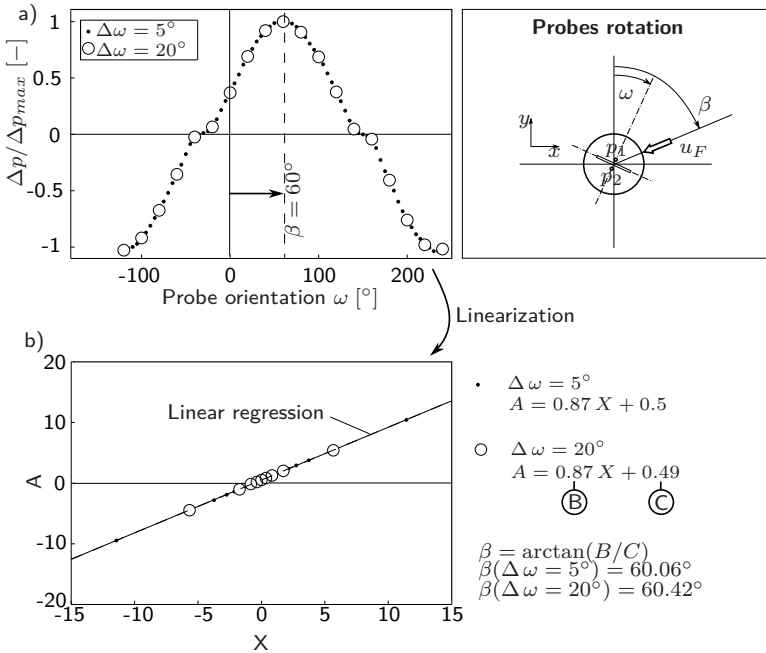


Figure 3.19: Linearization; a): probe output signal Δp against probe orientation ω for two different step widths $\Delta\omega$, b): Transforming the data into their linearized form and processing the flow angle β using linear regression

by choosing a step size $\Delta\omega$ as large as possible, with an algorithm producing tolerable uncertainties. For the stator over tip investigations, the probe has been rotated by 20° steps where the maximum uncertainty is estimated to be $\pm 0.5^\circ$.

The major advantage of this approach is that it is possible to use as few as two probe orientations to acquire the flow velocity both in magnitude and direction. By this, the improved linearization procedure is found to be much more accurate than the one described by Dambach and Hodson (1999) [15]. Of particular importance is that the procedure in general can be applied to other shear stress measuring techniques e.g. surface hot film, surface hot wire and Micro-Electro-Mechanical Systems (MEMS) [56]. The following results gained in the compressor stator based upon SFP measurements are thought to be the first of their kind since they represent a time-resolved streakline pattern.

3.9 Stator Over Tip Flow Maps

First, SFP measurements have been carried out to determine the time-averaged flow velocity in magnitude and direction and to produce flow maps on the hub wall for the design operating point and an operating point affected by RI. Using the basic assumption the measurement principle is based upon, the flow direction obtained must be equal to the direction of the local wall shear stress. Therefore, the generated flow maps can be seen as an equivalent to the streakline pattern derived from oil flow visualizations.

The integration of the SFP in the CSC hub wall and the definition of the velocity triangle is shown in figure 3.20. Considering one measurement position, the mean value of the time-resolved differential pressure Δp was calculated at each probe orientation and the 18 data sets (18 orientations) were then processed to determine the fence velocity magnitude and angle (sections 3.8.1 and 3.8.2).

Figure 3.21 a) shows the absolute velocity flow field at design conditions. To better distinguish between different components of the secondary flow field, the velocity vectors have been transferred into a streakline pattern where the streaklines originating from the inlet plane have been colored differently from the ones originating from the tip gap (see figure 3.21 b). The regions of interest can be split into the main flow (black colored streaklines) entering the stator passage relatively undisturbed and the clearance flow (blue colored streaklines) leaking over the blade tip from the pressure side to the suction side. Considering the axial velocity component v in figure 3.21 c), the passage is found to be

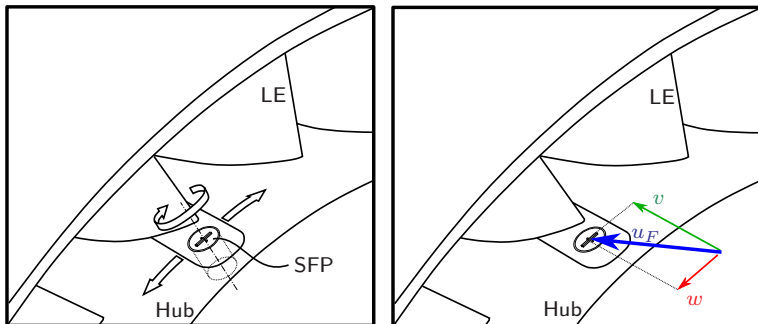


Figure 3.20: SFP implementation and vector nomenclature

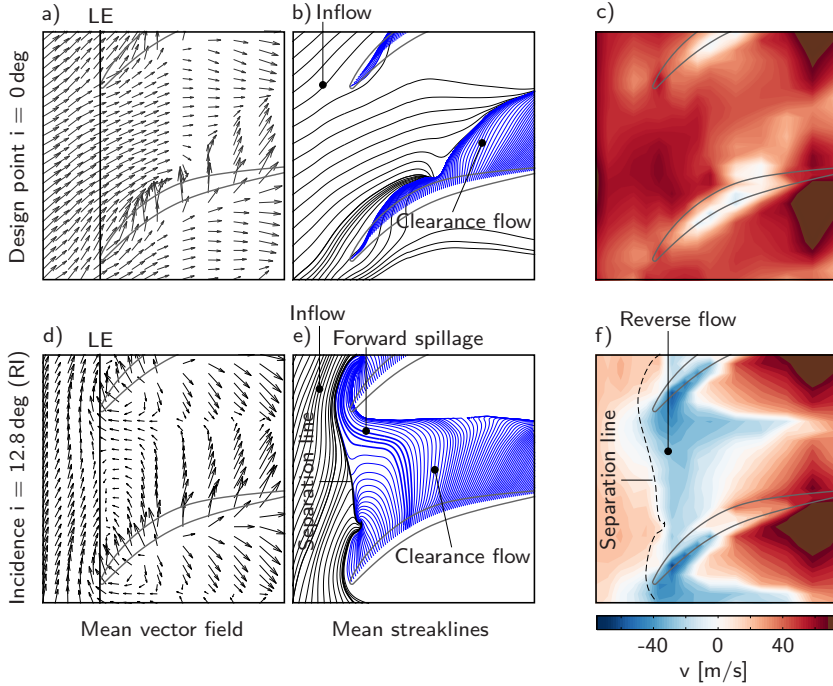


Figure 3.21: Mean vector field at design conditions ($i = 0^\circ$) and at an operating point affected by RI ($i = 12.8^\circ$), Mach number $Ma_1 = 0.4$

clear of any reversed flow that opposes the incoming main flow. Only the flow inside the gap driven by the pressure difference across the blade becomes more tangential.

In contrast, the mean flow field has changed considerably at $i = 12.8^\circ$ (figure 3.21 d). First, the incoming main flow is prevented from entering the stator passage at any location. Another important change is the clearance flow spilling around the leading edge of the neighboring blade (figure 3.21 e). The flow leaking the tip gap between the leading edge and 50% blade chord becomes entirely reversed converging with the incoming main flow at the separation line located closely to the stator inlet plane. The measurements allow the reversed flow to be precisely quantified for the first time (figure 3.21 f). While the axial expansion of $v < 0$ m/s varies in pitch wise direction, reversed flow is strongest on the pressure side near the blades leading edge.

It is worth noting that forward spillage, formerly ascribed to be a necessary boundary condition for stall inception, in the present case is clearly developing well before stall onset. More importantly, Weichert (2011) [61] and Weichert et al. (2014) [62] proved that forward spillage of the clearance flow is a unique flow feature that only becomes apparent after the formation of an embryonic disturbance. Flow visualization studies provided the experimental evidence of a radial vortex structure that is involved in this process. The question now arises as to whether the prestall instability RI is also characterized by propagating vortex structures and what role they actually play concerning the cause and effect of forward spillage.

3.10 Time-Resolved Velocity Flow Maps

This section describes the methodology used to appropriately obtain maps of velocity vectors representing the transitory process of a modal event. The approach basically combines the triggering method for detecting randomly arising modal events and the SFP vector algorithm.

3.10.1 Methodology of Ensemble Averaged Results

A necessary requirement for this approach is a reference sensor recording the time-resolved pressures near the stator leading edges simultaneously to the SFP data. The setup shown in figure 3.5 thus complies with this requirement. The algorithm for processing the flow velocity in magnitude and direction is described in section 3.8.2. The ensemble-averaged input to the algorithm is composed of data from repeated instances of the modal event. In detail, data from at least 100 modal events build an ensemble for each SFP orientation and the series of orientations are then passed to the linearization method to obtain the flow vector. The foregoing procedure must be carried out successively for each phase angle of the modal event individually. Starting from the trigger at phase 0° , any flow disturbance can be traced back chronologically up to the point in time at which the modal event has been initiated.

Since the reference sensor has a circumferential offset of 63° to the measurement location of the SFP, the phase angle from the SFP data needs to be adjusted by considering the propagation speed k_m of each mode m .

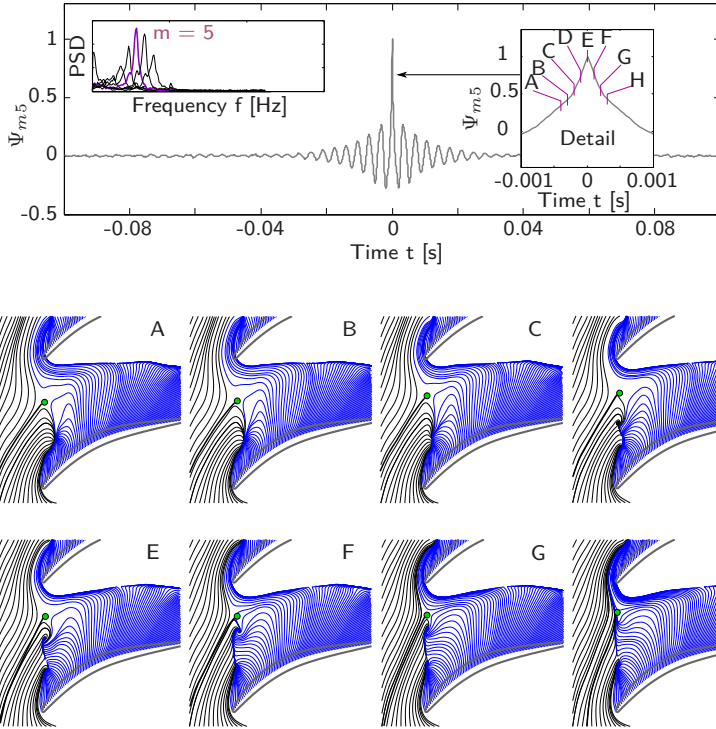


Figure 3.22: Development of the time-resolved streakline pattern during the modal event ($m = 5$), Formation of a coherent flow structure in the interface between the reversed flow (blue) and the incoming flow (grey).

3.10.2 The Ensemble Averaged Velocity Flow Map

The step-wise procedure presented in section 3.10.1 has been carried out for the dominating mode of order $m = 5$ first (see figure 3.22). Specific points in time (A-H) evenly arranged around the trigger ($t = 0$ s) have been considered for investigating the time-resolved velocity vectors. Again, the map of velocity vectors has been transferred into a streakline pattern. To better assess the direction of the incoming main flow, the very streakline terminating at the saddle point from the continuous separation line (green dot) is highlighted by a thick black line. When stepping even further back in time (before time step A), only the inflow direction is increasingly oscillating without any noticeable fluctuation of the clearance flow. However, a certain amount of clearance flow

is always observed to leak into the neighboring passage. From the period of time between A and C it is seen that the change in inflow direction accords to an increasing incidence to the compressor blade. The onset of a local disturbance is recognized at time step D when the interface between the reversed flow and the incoming flow appears to be destabilized. The coherent flow structure originates at almost 40% pitch apart from the stator leading edge. While propagating along the cascade inlet plane in circumferential direction, the vortex temporarily increases in size. When approaching the adjacent leading edge (E-H), the vortex is seen to be finally dissipating. Monitoring the inflow angle 5 mm upstream of the leading edges half way pitch between the blades allows to quantify the unsteadiness of the local flow field during the modal event. Variation of the flow direction is seen to occur in a range of about $\beta = \pm 10^\circ$ proving a significant level of flow unsteadiness.

It is quite interesting to note that the local disturbance found in the CSC strongly reminds of an embryonic spike formation reported by Weichert et al. (2014) [62]. However, there are substantial differences between spikes and prestall flow disturbances. First, the spike disturbance was found to be part of a highly transitional process. Stall is initiated immediately after the first sign of spike formation. In contrast, prestall disturbances arise in broad operating range before stall onset. They appear to be briefly amplified within stochastically distributed points in time without evolving into a stall cell. Another difference is forward spillage of the clearance flow present after the embryonic spike and prestall disturbances clearly forming in a flow regime with forward spillage present beforehand.

The shown streakline pattern phase locked to the modal event is thought to be the first of its kind since it is representing a time-resolved equivalent to the pattern from oilflow visualizations which in turn is inevitably time-averaged.

Another way of assessing the unsteadiness of the flow field is to carry out a classical Reynolds decomposition of each velocity vector according to:

$$\vec{c} = \bar{\vec{c}} + \vec{c}' \quad (3.16)$$

By this, the mean vector field from figure 3.21 d) has been removed from the time resolved velocity flow maps presented in figure 3.22 to get the fluctuation part \vec{c}' . Successive time steps up to $t = 0.001\text{ s}$ after the trigger time are shown in figure 3.23.

From the vector length it can be seen at each time step that the unsteadiness of the flow is mainly concentrated upstream of the leading edge plane. What is

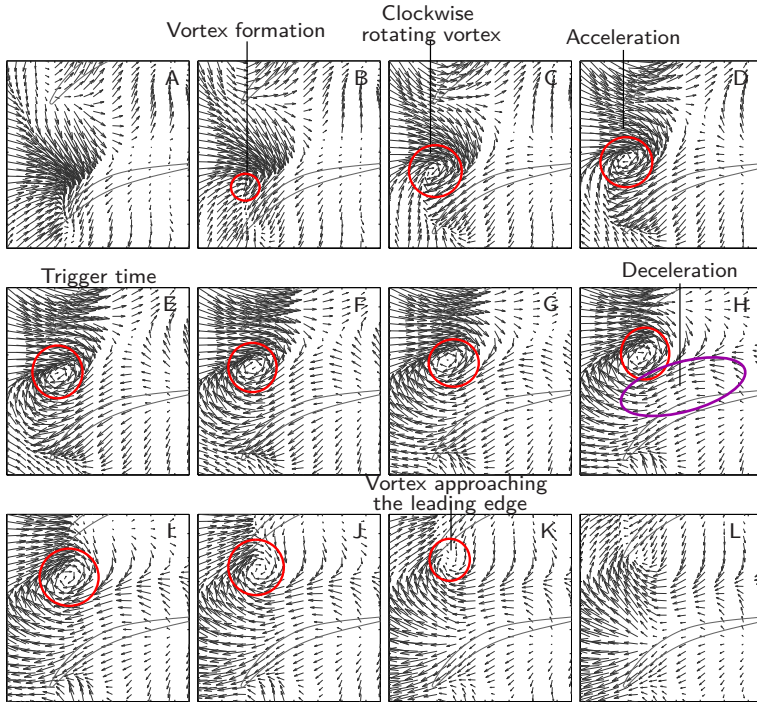


Figure 3.23: Vortex formation in the vector field of velocity fluctuations \vec{c}' during the modal event ($m = 5$)

shown from A to C is a detailed progression from an undisturbed passage to the formation of a discrete prestall flow disturbance. Shortly before the trigger time (E), the inflow is seen to be significantly accelerated, however, the flow close to the blades suction side becomes increasingly decelerated ending up in a vortex formation (circled in red). Once fully developed, the trajectory of the clockwise rotating vortex is coinciding with the separation line from the absolute streakline pattern in figure 3.21 e). Moreover, it is hereby confirmed that the local patch of low pressures obtained in figure 3.14 is linked to a vorticity disturbance developing in the shear layer between the main and the reversed clearance flow. Considering the period of time enclosed by B and K, the transitory growth and decay of local vorticity can be easily tracked. Also, the vortex induced velocities of the prestall disturbance appear to be causing a deceleration of the tip leakage flow across the entire chord length. Since the formation of vorticity is recognized first, deceleration of the clearance flow is

suggested to be an effect of a maturing disturbance rather than the origin of it. What can be clearly seen from time step L is a disturbance disappearing near the pressure side. More importantly, the disturbance is heading straight towards the leading edge without any hint of leaking into the neighboring passage. Therefore, the propagation mechanism around the annulus cannot be described by the propagation of a persistent disturbance itself. The transfer of information from one passage to the next must proceed in a different way.

A reasonable explanation of how the propagation might be possible anyway could be the following: An established disturbance is acting like a barrier to the incoming main flow. The latter is subsequently forced to be redirected into the neighboring passage. Right here, the inflow is more tangential to the stator inlet plane causing an increased incidence on the blade. Unfortunately, there are different plausible explanations of how the altered inflow to the neighboring blade is causing the formation of a new prestall disturbance. According to the classic spike formation described by Pullan et al. (2012) [54] the prestall disturbance would then be caused by a leading edge separation. A second explanation would include a vorticity disturbance changing the circulation of the neighboring blade which in turn causes an increased aerodynamic loading and a strengthened clearance flow resulting in a perturbed shear layer. What might be a much more logical assumption, however, is that the boundary between the incoming and reversed flow is destabilized by the altered main flow. Shear layers in general are expected to be responding most sensitively to small irregularities in the flow field when they are exposed to high pressure gradients. And the shear layer between the incoming and the axially reversed clearance flow is known to be one of the most vigorous ones in tubomachinery flows. Since the aerodynamic blade loading is increased anyway at $i = 12.8^\circ$ it is therefore possible that an altered inflow might destabilize the shear layer and finally ending up in a new vortex formation. This hypothesis will later be verified by experimental investigations discussed in chapter 4.

Another study has been carried out to prove whether the prestall flow disturbances do propagate along the same trajectory for all modes considered. A vortex identification method, namely the Q-criterion, was used for this purpose [9]. To process the Q pattern, the velocity gradient tensor must be decomposed into its symmetric and anti-symmetric part first. To do this, the second invariant of the gradient tensor can be expressed through:

$$Q = \frac{1}{2} [|\Omega|^2 - |S|^2] \quad (3.17)$$

where the vorticity tensor Ω_{ij} and the rate-of-strain tensor S_{ij} accord to:

$$\Omega_{ij} = \frac{1}{2} \left(\frac{\partial c_i}{\partial x_j} - \frac{\partial c_j}{\partial x_i} \right) \quad (3.18)$$

$$S_{ij} = \frac{1}{2} \left(\frac{\partial c_i}{\partial x_j} + \frac{\partial c_j}{\partial x_i} \right) \quad (3.19)$$

A vortex has been found in that area, where the magnitude of the vorticity dominates the shear strain rate or where Q shows increased positive values. Based on the nomenclature of velocity components used in the present work, equation 3.17 can be transformed into the following expression:

$$Q = -\frac{1}{2} \left(\frac{dv^2}{dx^2} + \frac{dw^2}{dy^2} \right) - \frac{dv}{dy} \frac{dw}{dx} \quad (3.20)$$

Modal event detection, phase-averaging, resembling the flow maps and processing the contours of velocity fluctuations has been repeatedly applied for each mode between $m = 3 - 7$. Five sequences of vector fields serve as a basis for the vortex identification method. The trigger vector field from the modal event of $m = 5$ is exemplarily illustrated in figure 3.24 a). Applying equation 3.20 to the vector field leads to the contour plot shown in figure 3.24 b). Increased values of Q are clearly seen to be concentrated in that particular area where the prestall vortex can be even visually detected in the vector field. Finding the global maximum in the Q pattern therefore allows for identifying the precise location of the vortex center which is indicated by a red cross in figure 3.24 c). The stepwise procedure has been repeated for each vector field from the modal event sequences between $-0.04 \text{ s} < t < 0.04 \text{ s}$ whereby any detected vortex location has been saved. Results from the different modes are shown in figure 3.24 d)- h). Generally, each modal event is found to be characterized by the same trajectory of vortex propagation mostly extending along the stator inlet plane (indicated by the magenta colored arrow). While vortex formation near the leading edges is found to be more distinct in concentrated areas, however, the trajectory shows an increased axially variation the further the disturbance approaches the neighboring blade. The latter feature tends to be more pronounced for higher mode orders.

The unique physical behaviour of vortex growth, propagation and decay applies for each mode found within the spectral signature of RI. However, proving of whether the circumferential distance between the vortices matches the wavelength of the mode order has yet to be carried out.

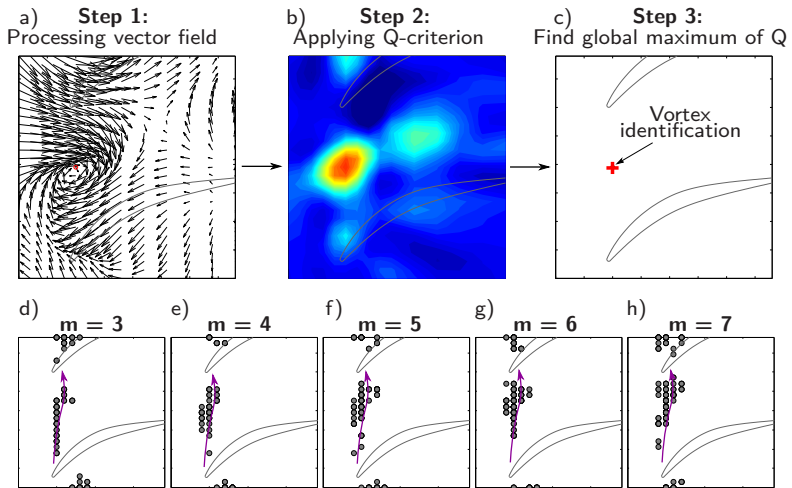


Figure 3.24: Vortex detection - positions of identified vortices during the progression of a modal event

3.10.3 Multi-Passage Velocity Maps for Different Modes

This section aims at improving the physical understanding of prestall disturbances and their impact on the flow field of the neighboring passages by examining the multi-passage vector fields over half the annulus.

The same methodology for processing the quasi-instantaneous picture was used for the velocity flow maps as for the static pressure contours in section 3.7. Given a sequence of vector fields phase locked to the modal event, only specific samples have been used for composing the multi-passage vector plots. The tangential displacement of the single-passage vector fields by one stator pitch can be easily calculated by the propagation speed of the prestall disturbances. Considering the mode $m = 5$, the speed was found to be $k_{m5} = d\phi/dt = 31 \text{ m/s}$. Using the stator pitch for $d\phi$ allows to obtain dt . The latter is specifying the equidistant time intervals within the modal event at which the vector fields are extracted to be finally attached to each other.

Figure 3.25 shows the 180° -vector flow maps for different mode orders starting with the smallest on top. In each flow map, the trigger passage is always on the same reference location. As mentioned earlier, the vector plot also includes a time domain. Looking onto the trigger passage, the passage on

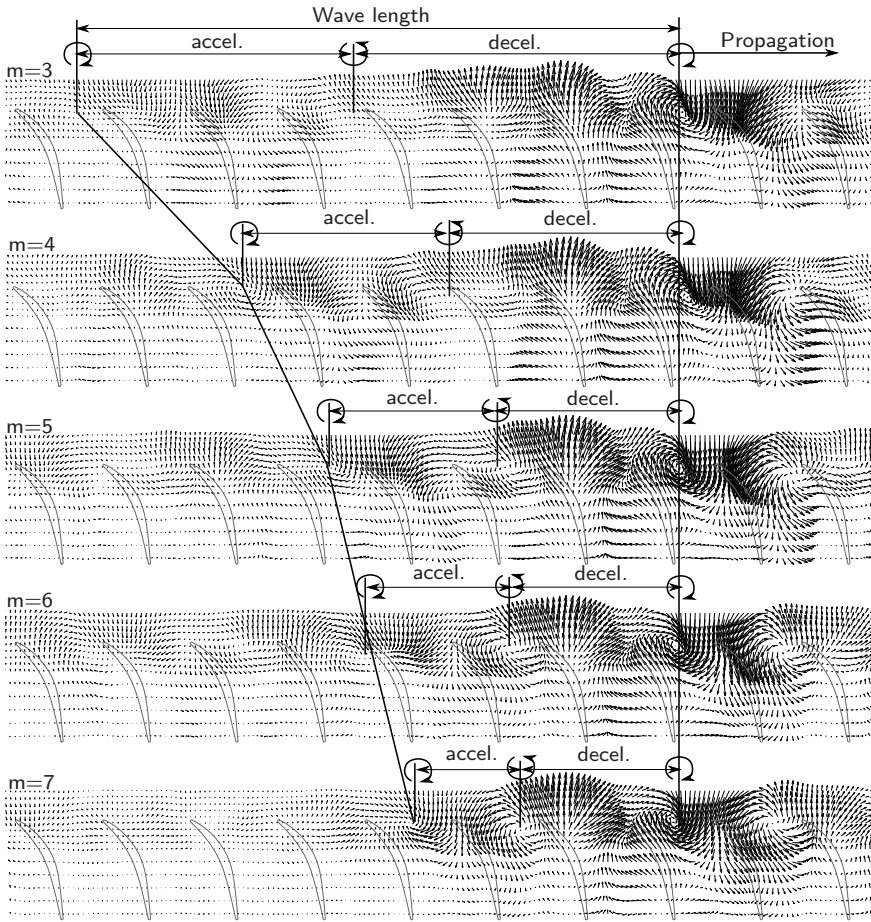


Figure 3.25: Quasi-instantaneous vector field of velocity fluctuations for different mode orders - half of the circumference shown; Circumferential count of vortices is in accordance with the respective mode order

the left side shows a flow field when the prestall disturbance was at an earlier stage of its development - the opposite is true for the passage on the right side. Therefore, the adjoined passages additionally show the progression of the modal event. Almost identical for each mode, the velocity fluctuations have quickly decreased after the disturbance has travelled about a quarter of the hub circumference. The trigger disturbance indicated by a clock-wise rotating

vortex induces an acceleration of the flow in the direction of propagation and a deceleration on the receding edge of the disturbance. Also, the areas of flow acceleration and deceleration cover differently sized sectors of the stator cascade. To balance the flow field in between the prestall disturbances, there must be an alternately rotating vortex structure. The latter, indicated by an anti-clockwise rotating vortex, therefore appears to be the consequence of the prestall disturbances interacting. Further to this, the wavelength of the flow field or the circumferential count of prestall flow disturbances (represented by clock-wise rotating vortices in the present perspective) precisely matches the mode order in each vector plot.

3.11 Conclusions

The prestall phenomenon RI is characterized by propagating flow perturbations neither fitting the mode nor the spike stall inception model. The nature of these disturbances was found to be highly intermittent and constantly changing in wave number and intensity which is why investigating them is such a challenging task. A target-oriented approach combining a recently established methodology with a novel instrumentation was successfully used to investigate the physical mechanism of RI nonetheless. The general findings can be summarized as follows:

1. Based upon static pressure measurements, flow disturbances of sub-pitch dimensions are seen to occur as patches of intense low pressure. They are found to be most likely arising just aft of the leading edges and propagating in circumferential direction of the stator cascade. Further to this, prestall disturbances are developing in groups where a certain circumferential count causes one specific peak within the spectral signature of RI.
2. It was found that the discrete patches of low static pressure can be associated with coherent flow structures. The vortex induced velocities cause a significant acceleration or deceleration of the flow in the neighboring passages.
3. There is strong evidence that the formation of prestall vortices occurs when the shear layer between the reversed clearance flow and the main flow is destabilized. Hereby the present assumption takes up a more recent idea of embryonic spike formation provided by Weichert (2011) [61]. Prestall vortices, even though disturbing the passage flow considerably, do not evolve in a stall cell. The progression of prestall vortices can rather be described by a sudden growth and decay within a brief period of time.
4. While propagating along the stator inlet plane, the prestall vortices increasingly cause the inflow to be redirected into the adjacent passage. Here, the altered inflow is ascribed to be subsequently destabilizing the interface between the reversed and main flow causing the formation of a new prestall vortex. This process is repeated from one passage to the next without any prestall vortex itself successfully entering the neighboring passage.

5. To obtain the above findings, a miniature probe was manufactured that is based on a well known and widely used measurement principle for wall shear stress measurements. However, the application, calibration and the methodology used for post-processing of the measurement data is new, allowing to obtain physical information of the boundary layer flow field in a meaningful and effective manner.

4

Rotor Experiments

Which experiments were carried out on the rotor configuration? Can the findings presented in chapter 3 be validated based upon the results from the compressor stage? What impact does rotor eccentricity have on RI characteristics? Is there an explicit indicator that can be used to predict an upcoming stall event?

Contents

4.1	Research Compressor	64
4.1.1	Instrumentation	67
4.1.2	Data Reduction	68
4.2	Compressor Performance	70
4.3	Inception of Prestall Instability RI	72
4.4	Spectral Characteristics	74
4.4.1	Propagation Speed	76
4.4.2	Study of Circumferential Modes	78
4.5	Effect of Eccentricity on RI	80
4.6	Study of Prestall Disturbances	85
4.7	Statistics of Prestall Disturbances	94
4.8	Rotating Stall - Rotating Instability	97
4.9	Transition Into Stall	103
4.10	Potential for Stall Warning	105
4.10.1	Influence of Rotor Eccentricity	106
4.10.2	Influence of Axial Measurement Position	108
4.11	Conclusions	114

The aim of this chapter is to introduce the axial compressor stage used as well as the instrumentation applied for assessing the compressor performance and recording the time-resolved pressures on the casing wall above the rotor blade tips. Data reduction applied for the purpose of phase-averaging the measurement data will be explained step by step. After that, operating ranges affected by RI will be identified for different rotor clearances and eccentricities. For selected operating points, a comprehensive analysis of the propagation speed, circumferential count and the trajectory of prestall flow disturbances explicitly ascribed to RI is carried out in detail. This chapter is closed by presenting several indicators which have the potential to reliably predict an imminent stalling event of the compressor.

4.1

Research Compressor ---

For the purpose of investigating RI developing in a rotor, a new single-stage, low speed axial compressor has been designed, constructed, assembled and brought into operation at the Department of Aeronautics and Astronautics of the Technische Universität Berlin. The compressor stage consisting of a rotor and a downstream stator is embedded in an open flow wind tunnel. Instrumentation to obtain the performance data has been conducted based upon standardized regulations listed in DIN EN ISO 5801 "Industrial fans - performance testing using standardized airways" [48]. While the inlet total pressure is measured using a Prandtl tube installed upstream of the rotor, static outlet pressure is determined using 16 static pressure taps equally arranged around the circumference. Rotational speed is adjusted and controlled by means of a photo optical sensor which additionally provides a trigger signal for phase-averaging of the pressure data recorded above the rotor blade tip.

A stepper motor driving the throttle allows for precise adjustments of the compressor's operating point. The rotor is powered by an electrical motor fitted in the hub. A flexible mounting of the motor enables the rotor to be shifted in radial direction allowing to consider eccentricity as an additional boundary condition especially for investigations on the prestall instability RI. The value of eccentricity is determined by measuring the shaft position relative to the casing wall at six equidistantly arranged positions.

The rotor has been designed for providing constant exit swirl based upon radial equilibrium with an 80% reaction at midspan. The 124-mm-diameter low hub-to-tip ratio rotor counts 14 carbon fibre blades designed with profiles from the

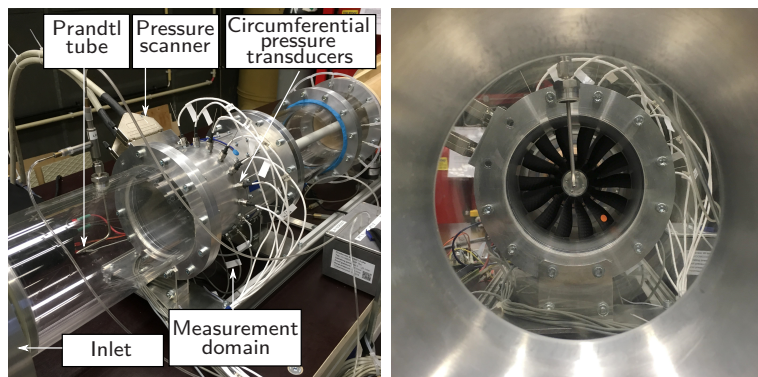


Figure 4.1: Photographs of the test rig

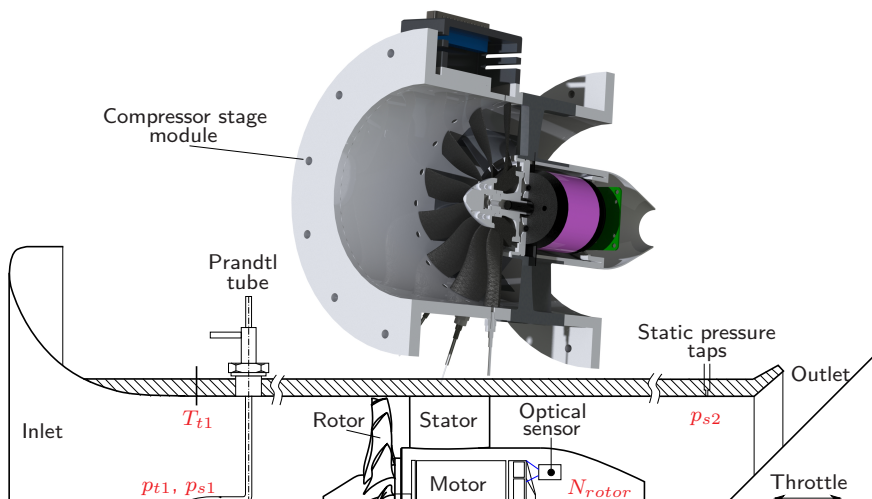


Figure 4.2: Rig schematic featuring instrumentation for determining the stage performance in accordance with DIN EN ISO 5901

NACA-65 series. Eight additive manufactured aluminium stator blades include the cabling for the electric motor, hence the large absolute chord leading to a sufficient blade thickness. By considering the slip factor being a function of aspect ratio and relative blade thickness, the required geometrical deflection of the rotor blade is adjusted via the lift coefficient C_A at 16 radial sections. Three of them (hub, midspan, tip) are shown in figure 4.3. General dimensions

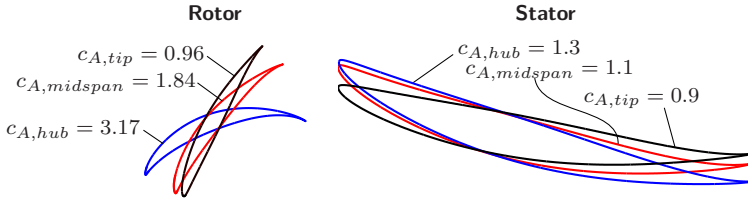


Figure 4.3: Rotor and stator blade sections; NACA-65 series

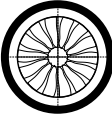

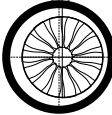
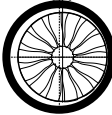
Table 4.1: Design specifications of the test rig

	Rotor	Stator
Casing diameter	124 mm	124 mm
Hub diameter	49 mm	63 mm
Hub-to-tip ratio	0.4	0.5
Blade count	14	8
Stagger (hub, tip)	17.9°, 62.4°	15.5°, 8.8°
Chord	20 mm	50 mm
Design speed	22000 rpm	-
Reynolds number	216000	-
Mach number	0.47	-
Design flow coefficient (inlet)		0.57
Design pressure rise coefficient		0.67

and performance data of the compressor stage are summarized in table 4.1. In the present work, the absolute clearance τ between the rotor blade tips and the casing has been varied by using different blade spans. Denton (1993) [18] ascribed the clearance flow and the associated clearance vortex to be rather depending on the clearance to chord ratio than on the clearance to blade height ratio. Since the flow field of interest is decisively affected by the clearance flow, the gap height is put in relation to the rotor tip chord. Throughout the following explanations, an average clearance of $\bar{\tau} = 2.8\%$ tip chord is denoted as nominal gap (NG) whereas the large gap setup (LG) has an average clearance of $\bar{\tau} = 5\%$ tip chord. In another parameter study, each rotor has been shifted in radial direction by the same value of 0.25 mm resulting in eccentricities of $\varepsilon = 90\%$ for NG and $\varepsilon = 50\%$ for LG. In this work, eccentricity ε is being expressed as a percentage of the average clearance size $\bar{\tau}$:

$$\varepsilon = (\tau_{max} - \tau_{min}) / \bar{\tau} \quad (4.1)$$

Table 4.2: Tested rotor configurations

	Concentric (CON)		Eccentric (ECC)	
	LG	NG	LG	NG
Average clearance $\bar{\tau}$	5%	2.8%	5%	2.8%
Min. clearance τ_{min}	5%	2.8%	3.75%	1.5%
Max. clearance τ_{max}	5%	2.8%	6.25%	4%
Eccentricity ε	0%	0%	50%	90%
Pictogram				

In-service eccentricities usually reaching values up to 50-75% may be a consequence of deterioration through blade-to-casing contacts, thermal deformation as a result of transient manoeuvres or manufacturing uncertainties just to mention a few. Thus, the eccentric NG setup is representing a case of rather exceptional fashion but also reasonable when emphasizing the limitations of potential stall warning approaches presented in section 4.10.

4.1.1 Instrumentation

The datum setup includes 20 fast response pressure transducers (PC1-PC20) being flush mounted in the casing wall 3 mm upstream of the rotor leading edges. Another array of transducers (PA1-PA13) is measuring the chord-wise static

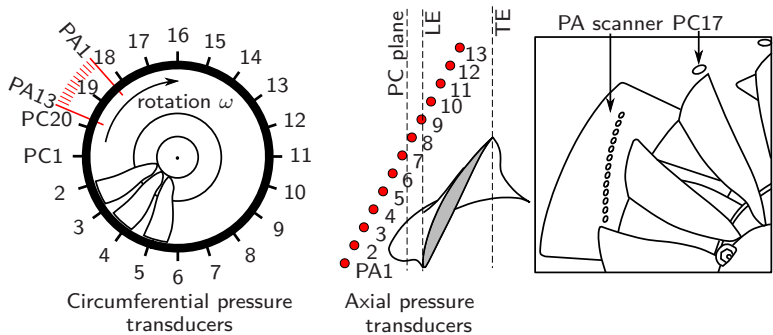


Figure 4.4: Piezoresistive pressure transducers flush-mounted in the casing wall

pressures between 1.2 axial chord upstream of the rotor inlet plane to half an axial chord downstream. However, transducers PC18-PC20 need to be replaced when using the axial sensor array. A schematic setup of the rotor overtip sensor installation is shown in figure 4.4. For the purpose of better assessing the resolution of the axial sensor array, the black circles are representing the actual scale between the transducers and the blade tip profile.

An additional signal from the optical sensor providing one trigger per rotor revolution allows for phase-averaging of the simultaneously recorded static wall pressures. Data has been sampled at 48 kHz giving approximately 12 samples per passage when running at a rotor speed of 10 000 rpm. To avoid aliasing, all signals have been low pass filtered with a cut-off frequency set to 24 kHz.

4.1.2 Data Reduction

The data reduction method presented in this section is mainly concerned with analyzing the time-resolved pressures recorded in the rotor section.

Given the trigger signal providing one trigger per rotor revolution each of the pressures is to be undergoing the step-wise procedure shown in figure 4.5. The aim of this procedure basically describing phase-averaging is to show how the repeatability in the blade passing signal changes when successively reducing the compressor flow coefficient. Any pressure fluctuation not to be ascribed to the blade passing itself becomes thereby visible. In other words, any fluctuation is extracted from the relative frame of reference. The data reduction consists of the following steps:

- (1) While leaving the flow coefficient constant, data from all 20 circumferential sensors (PC) are recorded separately for 100 rotor revolutions. One of those signals depicting the first revolution is plotted in figure 4.5 a) whereby just two of 14 blade passings are shown.
- (2) 100 signals are collected and the average blade passing is computed as shown by the red line in figure 4.5 b).
- (3) By taking the signal from the first revolution and comparing it to the average trace (see figure 4.5 c)) the difference is found as depicted in figure 4.5 d).
- (4) In the following, the difference across an entire revolution is used to compute the RMS and the skewness. By repeating the steps shown in

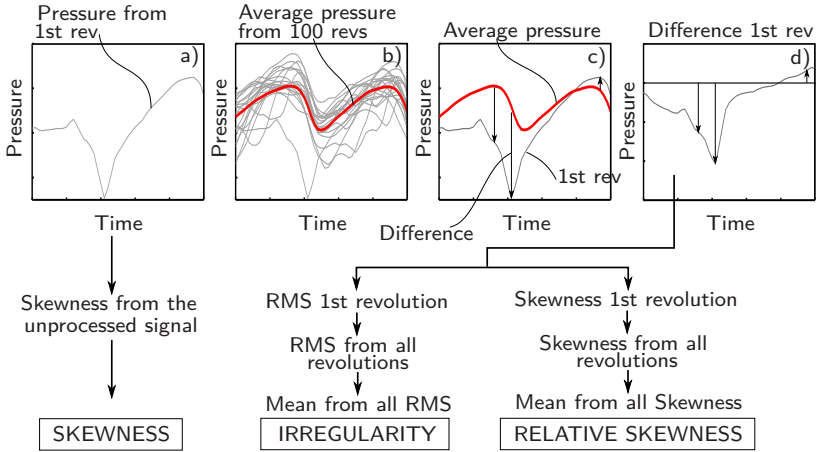


Figure 4.5: Data reduction of the time-resolved pressures recorded near the blade tips leading to the quantities "Skewness", "Irregularity" and "Relative Skewness" each representing a single number to be processed at a certain flow coefficient

c) and d) for the complete set of 100 revolutions, in sum 100 RMS and skewness values are calculated in the same manner.

- (5) The mean of both statistical moments is then processed. Finally, the single numbers each representing a scalar value for a certain flow coefficient are denoted as "irregularity" and "relative skewness" respectively. Following the path from step a) onwards, the absolute skewness is applied on the unprocessed signal without phase-averaging.

The process is also used when analyzing the casing static pressure contours phase-locked to the rotor. This allows flow disturbances to be investigated that are several orders of magnitude smaller than the peak suction of the blades. In doing so, the preceding process is applied on the pressures measured by the axially aligned array (PA).

The performance evaluation can be carried out based upon different types of compressor maps. In the first one used, the static-to-static pressure ratio Π_s is plotted against the corrected inlet mass flow rate \dot{m}_{corr} . The latter being proportional to the non-dimensional flow rate $\dot{m}_{red} = \dot{m} \sqrt{T_{t1}} / p_{t1}$ is the real mass flow that would enter the compressor inlet duct if the inlet total pressure and inlet total temperature corresponded to ambient conditions compliant with the International Standard Atmosphere (ISA). The static-to-static pressure ratio

has been utilized in this work since the total pressure rise across the stage is marginal. The aforementioned parameters are defined as:

$$\Pi_s = p_{s2}/p_{s1} \quad (4.2)$$

$$\dot{m}_{corr} = \dot{m} \frac{\sqrt{T_{t1}/T_{ISA}}}{p_{t1}/p_{ISA}} \quad (4.3)$$

where the static pressures p_{s1} has been obtained by the upstream Prandtl tube and p_{s2} by the downstream static pressure taps. The mass flow $\dot{m} = k_1 \cdot \rho c_{m1} A$ was determined by converting the dynamic pressure q from the Prandtl tube into the inflow velocity c_{m1} which was then multiplied with the density ρ and the cross-section A . The discharge coefficient $k_1 = 0.973$ specifically determined for the bellmouth intake has been used to consider the loss of momentum near the casing wall for precisely calculating the mass flow \dot{m} entering the wind tunnel.

The second map is the total-to-static pressure rise characteristic where the total-to-static pressure rise coefficient Ψ is plotted against the flow coefficient ϕ . Both parameters are non-dimensional and they can be expressed through:

$$\Psi = \frac{p_{s2} - p_{t1}}{u_{mid}^2 \cdot \rho / 2} \quad (4.4)$$

$$\phi = \frac{c_{m1}}{u_{mid}} \quad (4.5)$$

where u_{mid} is defined as the rotational speed at rotor mid span and c_{m1} is the inlet velocity.

4.2 Compressor Performance

The compressor maps are used to monitor and compare the performance of all stage configurations presented in table 4.2. While compressor maps containing several speed lines serve for comparing the different gap configurations (figure 4.6 a)), only the speed lines recorded at 10 000 rpm have been transferred into the total-to-static pressure rise characteristic (figure 4.6 b)) since the latter is more appropriate for assessing the stall inception type. Performance data from the eccentric compressors are additionally shown in the pressure rise characteristic. Each speed line was measured by continuously recording the inlet and casing pressures between open throttle and stall. While reducing the mass flow, the

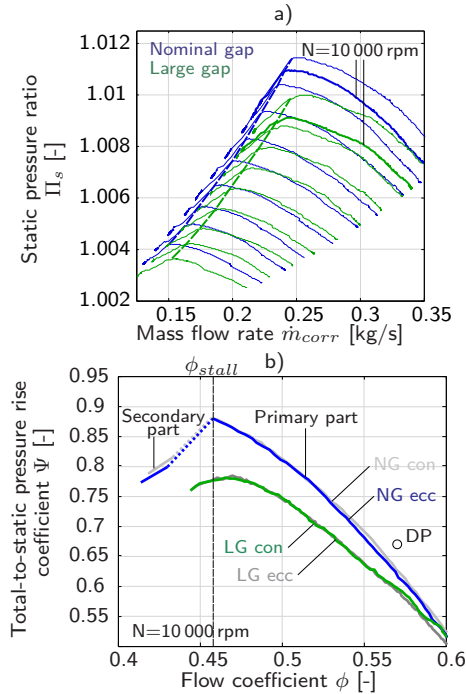


Figure 4.6: Compressor maps for the LG (a) and NG compressor stage (b); Total-to-static pressure rise characteristics for all gap size and eccentricity configurations each running at speed of 10 000 rpm (c)

pressure rise across the stage increases until the stability limit is reached. From this point onwards, the compressor enters into stall accompanied by a sudden loss of pressure rise and mass flow. Based on this, localizing the stalling limit is easier to distinguish for the NG configuration since the drop in pressure rise is much more pronounced. Comparing both gap configurations, the speed lines from the LG setup are shifted towards lower pressure ratios and mass flow rates. This seems plausible as secondary losses and viscous effects increasingly dominate the tip area of the compressor rotor when increasing the clearance. Please note that in some cases, an increased gap size had a beneficial effect on compressor performance as the clearance vortex was found to be reducing the predominant three-dimensional separation in the endwall-suction surface corner (Wisler (1985) [63]).

Considering the total-to-static pressure rise in figure 4.6 b) the stalling flow coefficient for the concentric NG setup is recognized on the negative slope leading to the assumption that stall is most likely initiated by the spike type inception. When operating on the in-stall part or the secondary part of the pressure rise characteristic, the average Fourier transform derived from the pressures recorded by the sensors PC shows an additional peak arising at about 45% of the blade passing frequency (BPF) indicating RS (cf. figure 4.8). This criterion was also applied on the LG setup allowing to precisely identify the stalling flow coefficient located on the positive slope of the pressure rise characteristic. In general, the eccentric case does not change the stall limit at all. This is in contradiction to the findings of Young et al. (2017) [65] who reported a slight shift towards increased mass flow rates but still being located on the initial speed line. Unfortunately the reason for this trend absent in the present case could not be answered in the scope of this thesis.

4.3

Inception of Prestall Instability RI

Young et al. (2013) [64] found that if the clearance is sufficiently large, an approaching stall event announces itself by growing irregularities in the blade passing signature near the rotor blade tips. This behavior was ascribed to a certain form of prestall instability. The rise in the level of pressure fluctuation could also be obtained in the compressor stator cascade. Since in this case the rise in RMS could be explicitly linked to the phenomenon RI, the equivalent parameter "irregularity" is used in the rotor to estimate the onset of RI at stable operation. Based upon the step-wise procedure presented in section 4.1.2 irregularity, skewness and relative skewness have been individually computed for about 30 flow coefficients between open throttle and in-stall condition. Results for the concentric LG and NG case are shown in figure 4.7.

With the compressor in its LG configuration (see figure 4.7 a)), a clear ramp-up in irregularity is observed when approaching ϕ_{stall} indicating that the average blade passing signal is being superimposed by an increasing pressure fluctuation. While the ramp-up is being initiated at about $\phi = 0.55$, the relative skewness significantly decreases from that point downwards giving an indication of the fluctuations properties. The rise in irregularity hints the rotor passage flow to be dominated by regions of distinct low pressures continuously growing in amplitude. By transferring the data into the frequency domain, the formation

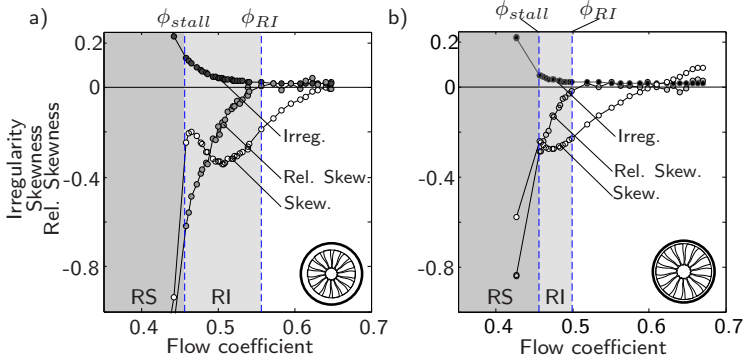


Figure 4.7: Irregularity, skewness and relative skewness as a function of flow coefficient, concentric LG (a) and NG (b) rotor running at 10 000 rpm - pressures recorded by the circumferential transducer array

of the spectral signature can also be observed at $\phi = 0.55$ (ϕ_{RI} in figure 4.8 a)), thus pointing to the link between the drop in relative skewness and RI inception. In contrast, the absolute skewness drops already from the beginning of the throttling process. This trend can be explained as follows: An increasing aerodynamic blade loading leads to an increased peak suction within the average blade passing signal. As a result, the pressure signal appears to be skewed as such. Between ϕ_{RI} and ϕ_{stall} an arising RI obviously has the effect of smoothening the pressure signal causing the skewness to rise again as long as the peak suction of the blades is dominating the negative pressure spikes. Just before approaching the stall limit the skewness drops steeply. The minimum and the maximum developing in the absolute skewness distribution under prestall conditions will later be used for stall warning assessment in section 4.10.

A quite similar behavior can be observed for the NG configuration (figure 4.7 b)). However, the ramp-up in irregularity and the drop in relative skewness is initiated at much lower flow coefficients ($\phi = 0.5$). Also, the level of both irregularity and relative skewness at ϕ_{stall} is lower compared to the one obtained for the LG setup. Another feature of the skewness distribution is the local maximum being absent at stable flow coefficients. Only a local minimum exists in close proximity to the stalling flow coefficient.

Summarizing, both gap configurations appear to be suffering from the prestall instability RI. However, not only does the pressure rise fall as the tip clearance is increased but the inception of prestall instability considerably moves to higher mass flows.

4.4 Spectral Characteristics

In order to unambiguously locate the exact point of RI inception and to allow a precise identification of rotating stall, Fourier transforms have been computed for all flow coefficients recorded. Results for both LG and NG concentric are depicted in figure 4.8 where the logarithmic scale on the y-axis helps identify initial signs of the spectral signature of RI even more precisely. With the compressor in its LG setup, the broad banded chain of peaks first arises at ϕ_{RI} from which the irregularity was rising and the relative skewness was dropping below zero thus proving the inception of RI to be ascribed to this very operating point. One can clearly recognize a gradual rise of amplitudes while the signature is shifted towards lower frequencies when decreasing the flow coefficient. Once stall is initiated, the overall amplitude level has increased disproportionately and the spectral signature drops below 50% BPF. All findings also apply for the NG albeit the power spectral density is much lower across the entire frequency range while the broad banded chain of peaks at stable operation of the compressor is recognized above 50% BPF. Furthermore, when transitioning into stall, a distinct peak attributed to RS arises just below the first engine order (EO). However, for the NG case the RS peak is quite distinct and much higher in

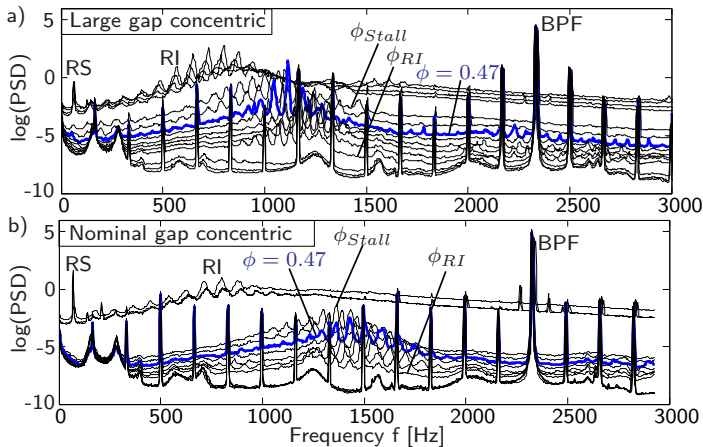


Figure 4.8: Fourier transforms as an average from all 20 circumferential sensors for different flow coefficients

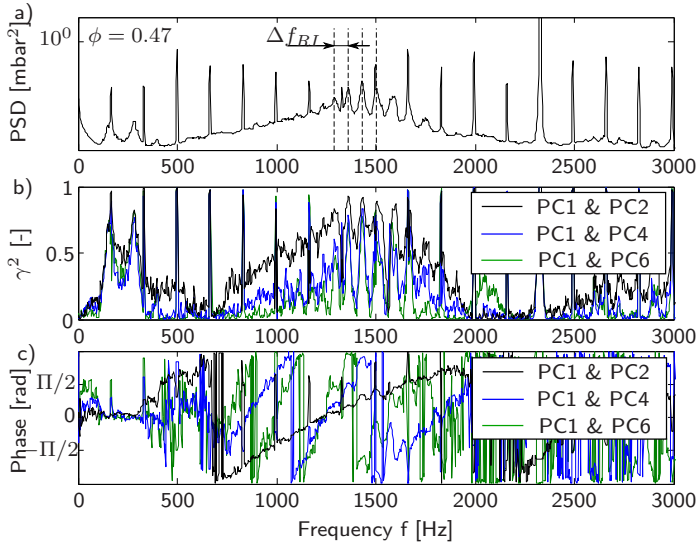


Figure 4.9: Fourier transforms, coherence and phase spectra for three selected combinations from the circumferential pressure transducers; NG at $\phi = 0.47$

amplitude even dominating the spectral signature of RI. As already presented for the compressor stator cascade, coherence and phase spectra have been applied to the data from the circumferential sensors in order to answer the question of whether the prestall disturbances do actually propagate around the annulus and at what speed they do so. An operating point corresponding to $\phi = 0.47$ has been considered for this purpose (see figure 4.9 a)). The set of three sensor combinations has been used to process coherence spectra each of them mirroring the broad banded chain of peaks (figure 4.9 b)). Within the affected frequency range the coherence always exceeds values of 0.6 clearly indicating disturbances being still tracable along the distance between each sensor pair considered. Unsurprisingly, the coherence reaches the highest values for those sensors being installed the closest to each other. Furthermore, the phase spectrum in figure 3.7 c) shows a step-wise slope in that area where the coherence exceeded values of 0.6 indicating the different wave numbers of circumferentially distributed pressure fluctuations. Thereby the spectral properties in the rotor were proved to be quite equal to those obtained in the stator (cf. figure 3.7). The peaks at $f = 130 \text{ Hz}$ and $f = 250 \text{ Hz}$ whose origin could not be determined in the scope of the present thesis must correspond to a zero mode since the coherence is above 0.6 and the phase is zero.

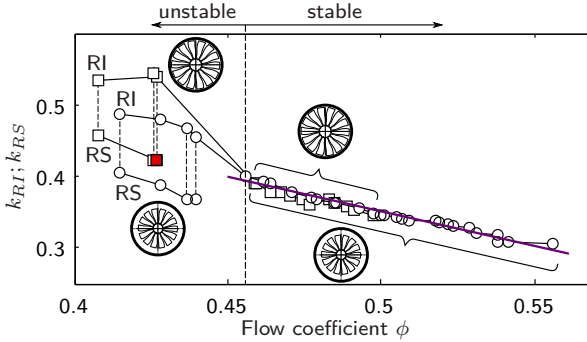


Figure 4.10: Convection speed of propagating prestall disturbances (RI) and stall cells (RS) for LG and NG rotor

4.4.1 Propagation Speed

Up to this point the question about a tangible link between the single peaks in the spectral signature and the negative pressure spikes is still unanswered. A first step to gain insight into this relationship is taken by calculating the propagation speed of the flow structure causing the signature. The speed can be derived from the Fourier transform by dividing the difference frequency between two neighboring peaks by the casing circumference. This procedure bases upon the reasonable assumption that all modal patterns do propagate at about the same speed.

The propagation speed k_{RI} has been calculated for each operating point at which the spectral signature could be noticed. While processing the Fourier transforms at discrete flow coefficients the difference in frequency Δf_{RI} has been extracted from the spectrum and quoted as a percentage of the first EO.

$$k_{RI} = \Delta f_{RI} / 1.EO \quad (4.6)$$

The parameter space covering the speed lines from NG and LG each running at 10 000 rpm also includes the in-stall part of the pressure rise characteristic. By reading out the frequency corresponding to the RS peak, the stall cell speed k_{RS} could also be investigated.

$$k_{RS} = f_{RS} / 1.EO \quad (4.7)$$

For both gap configurations, the propagation speed of prestall disturbances increases linearly as the flow coefficient is reduced (see figure 4.10). These find-

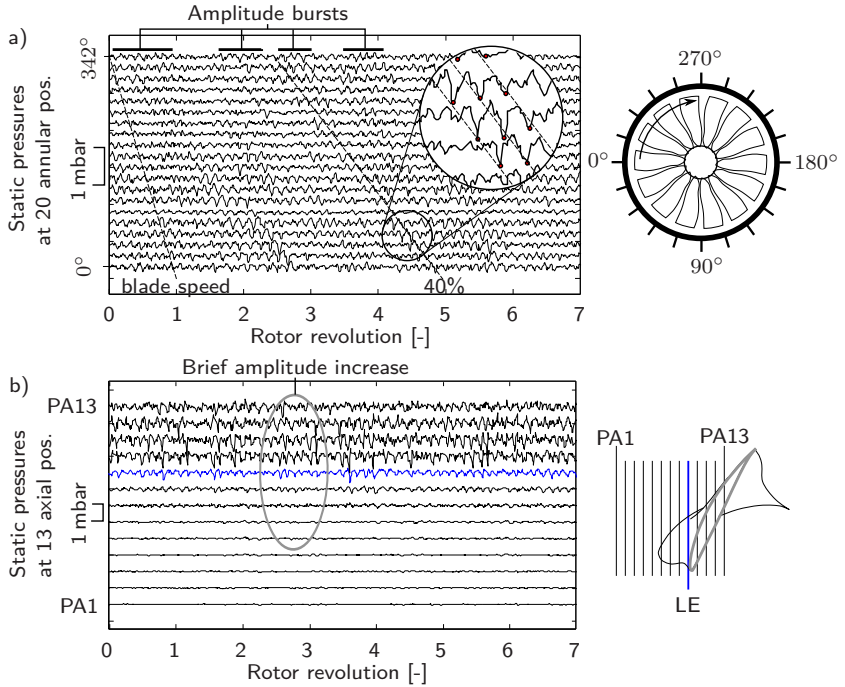


Figure 4.11: a) Casing static pressures at 20 annular positions; b) Casing static pressures at 13 axial positions (each reduced by the average blade passing signal), NG rotor operating at $\phi = 0.46$

ings are in good compliance with the ones obtained from investigations carried out in the stator cascade. Additionally, the speed appears to be independent from the clearance size apart from the circumstance that RI is initiated much later when the clearance is smaller. Also observable is a substantial difference between the stall cell speed and the convection speed of prestall disturbances raising the question as to how both phenomena interact and where each of them are to be located within the rotor. The preliminary conclusion would be that the disturbances must overtake the stall cell in some way. A final answer to this question will be provided in section 4.9.

Before continuing with the mode analysis, the following assessment of annular pressure data is used to verify the propagation speed at the last stable operating point (ϕ_{stall}). Beyond that, a first step is taken in the direction of clarifying

the nature of propagating prestall disturbances more closely. First of all, the average blade passing signal was removed from each pressure signal by applying the data reduction presented in section 4.1.2 and then plotted against rotor revolution (see figure 4.11 a)). Even though the spatial resolution is limited, the traditional approach of analyzing the 20 pressure data (PC1-PC20) helps identify stochastically distributed amplitude bursts. When connecting the trace of pressure minima, as it is demonstrated in the zoom, one can clearly recognize a propagation in the direction of rotor rotation. The resulting slope covering about 2.5 revolutions reveals a speed that is 40% of the blade speed which is in good agreement with the speed derived from the spectrum (cf. figure 4.10, at $\phi_{stall,NG}$). At this point, it should be noticed that the pressure fluctuation should not be mistaken with modal perturbations known from modal stall inception. In the present case, the modal RI oscillations are of sub-pitch dimension, they vary in amplitude, they propagate at much higher convection speeds than modes from modal stall inception and they are clearly arising on the negative slope of the pressure rise characteristic.

Additionally, the same analysis has been carried out for the static pressures recorded at several axial locations (see figure 4.11 b)). Considering the alignment of the probe installation (PA), the amplitude bursts observed between upstream to downstream of the leading edge plane appear to be in phase. However, the maximum amplitudes are recognized in the front half of the rotor passage. Also, the signal measured inside the passage is more of a spiky nature, whereas the upstream fluctuation is seen to be harmonical.

4.4.2 Study of Circumferential Modes

The following analysis serves for the purpose of assigning a certain mode order to each peak of the spectral signature. Using cross-spectral matrices and applying them to the data recorded by the circumferential sensors as it has been done in the compressor stator cascade leads to resolve mode orders up to $m = 9$. However, this method has been abandoned since much higher mode orders are being expected in the present rotor. To still get an equivalent to the classical mode spectrum, each frequency from the Fourier transforms has been divided by the frequency difference Δf_{RI} taken from the spectral signature.

In figure 4.12 the color-coded amplitudes are plotted over wave number (mode order) and all flow coefficients between inception of RI and stall onset. To ensure a better allocation of the mode spectra within the pressure rise characteristic, the speed line recorded at 10 000 rpm has been additionally inserted into the diagram. For the LG setup (see figure 4.12 a)), RI is initiated by wave numbers

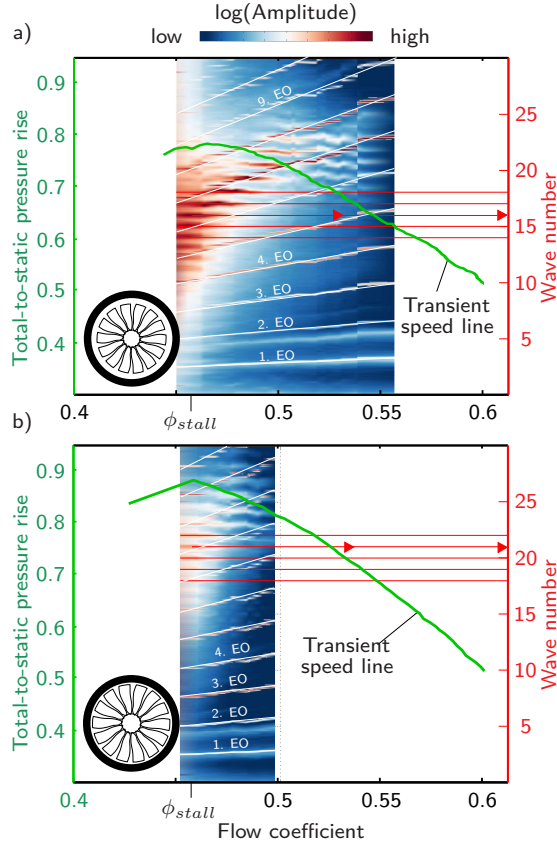


Figure 4.12: Total-to-static pressure rise characteristics, Fourier transforms as a function of wave number (circumferential count of prestall flow disturbances), LG (a) and NG (b)

developing at around $m = 22$. While approaching the stalling flow coefficient ϕ_{stall} , the wave number decreases with an almost linear trend. This appears to be an exceptional finding since the scale of the disturbances continuously grows with their speed increasing. This is in contrast to common theories in which small disturbances do propagate faster than large ones. At ϕ_{stall} one can clearly see a dominant wave number of $m = 16$. Quite similar trends can also be observed for the NG configuration in figure 4.12 b), however, the wave numbers are being located at much higher mode orders across the entire operating range.

4.5 Effect of Eccentricity on RI

There are only few investigations on rotor eccentricity enabling quantification of the effect on compressor efficiency and stall margin. A very recent paper by Young et al. [65] provided important insights into the stall margin in an eccentric rotor. The stall margin turned out to be previously estimated far too conservatively. The axisymmetric clearance has been properly discussed in terms of a redistribution of the flow coefficient around the annulus and the local stability. Taking into account the average clearance notably affecting the prestall instability RI, it is therefore even more surprising that an asymmetric clearance has not yet been considered regarding the local flow field as well as the overall inception of RI.

To examine the effect of tip clearance asymmetry in more detail, the flow coefficient dependent irregularity is processed as an average from all circumferential sensors for the respective concentric and eccentric case. In order to examine the variation in irregularity around the annulus, only selected circumferential locations (PC5, PC10, PC15 and PC20) have been considered. Figure 4.13 a) shows contradictory effects of rotor eccentricity on irregularity in the respective gap configuration. While the onset of the ramp-up remains unchanged in the respective eccentric cases, the level of irregularity in the eccentric NG setup in general has been raised across the entire operating range whereas the eccentric

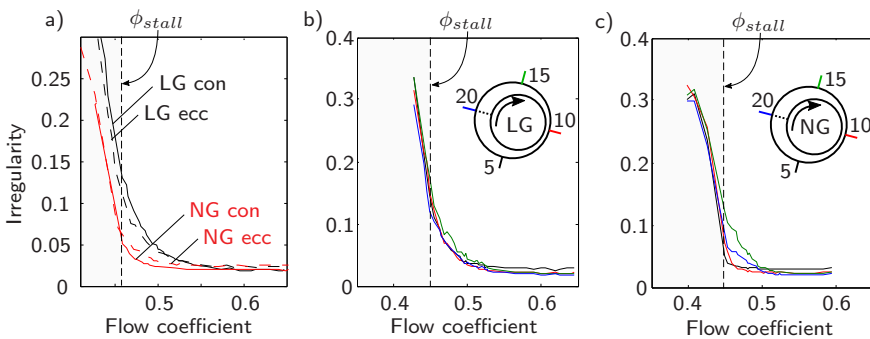


Figure 4.13: Irregularity as an average from all 20 circumferential sensors and selected Irregularities at four circumferential locations (5, 10, 15, 20) for the eccentric LG and NG rotor

LG rotor shows a lower level of irregularity compared to its concentric setup. Figure 4.13 b) shows that there is little variance around the annulus when the average clearance is large. A quite different behavior can be observed for the eccentric NG (see figure 4.13 c)). In the small tip clearance region (PC5, PC10) there is no discernable rise in irregularity prior to stall, whereas the signals recorded in and just after the maximum clearance already start rising from $\phi = 0.5$.

Concerning the relative skewness, the same analysis was performed as applied for the irregularity (see figure 4.14). An asymmetric clearance leads to a lowering of the relative skewness level especially within the operating range without RI (figure 4.14 a)). When approaching the stalling flow coefficient, eccentricity has a decreasing impact on the level of relative skewness. While there is no real variety of irregularity in figure 4.13 b), the relative skewness appears to be providing much more concrete information about the prestall instability developing in the eccentric LG rotor. Once RI is present, the relative skewness reveals the low pressure disturbances to be slightly increased in amplitude in that sector where the clearance is largest (figure 4.14 b)). A comparable, however much more pronounced trend applies to the NG case. Comparing the green colored distribution in figure 4.14 c) with the solid black line in figure 4.14 a), it becomes obvious that the maximum clearance in the eccentric NG rotor causes the same evolution of prestall instability as the average clearance does in the concentric LG rotor.

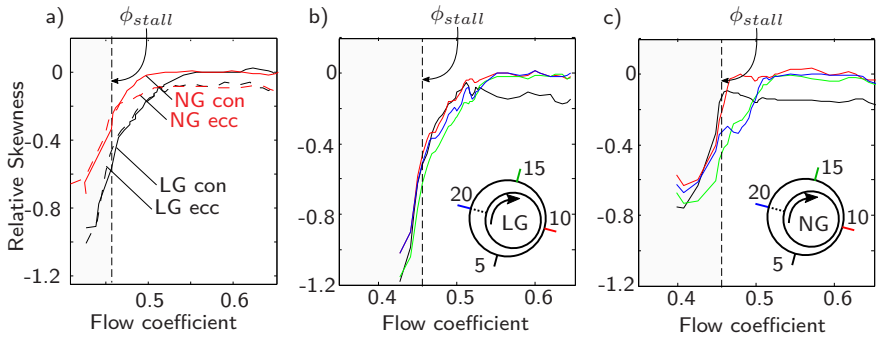


Figure 4.14: Skewness as an average from all 20 circumferential sensors and selected skewness distributions at four circumferential locations (5, 10, 15, 20) for the eccentric LG and NG rotor

This means that the local clearance within a certain annular sector of an eccentric rotor appears to be affecting the intensity of RI as much as an axisymmetric compressor with the same average clearance.

Since in the minimum clearance sector the relative skewness shows no drop just before stall onset (PC10 & PC5 in figure 4.14 c)), the following analysis answers the question of how the prestall disturbances actually change as they alternately pass through the large and the small clearance sector. Pressure traces shown in figure 4.15 have been recorded at ϕ_{stall} . Equivalent to figure 4.11 a), any disturbance arising within the amplitude bursts can be tracked while propagating around the annulus at 40% of the blade speed. However, the location showing the largest pressure amplitudes (red box) has a circumferential offset of about $\Delta\varphi = 70^\circ$ to the maximum clearance. At $\varphi = 90^\circ$ the pressure fluctuations are almost disappearing. Only a few discrete disturbances seem to be capable of passing through the minimum clearance area.

Moving on to consider the spectral signature at a certain circumferential location, each PC-data set has been individually assessed. The spectra processed at an operating point corresponding to $\phi = 0.46$ have been transferred into a polar plot in figure 4.16, where the frequency has been divided by the BPF and plotted on the radial axis. Starting with the concentric LG, there is no variety of the spectral signature around the annulus. Setting the LG rotor at $\varepsilon = 50\%$, the signature is still be seen at around 50% BPF while the amplitude becomes

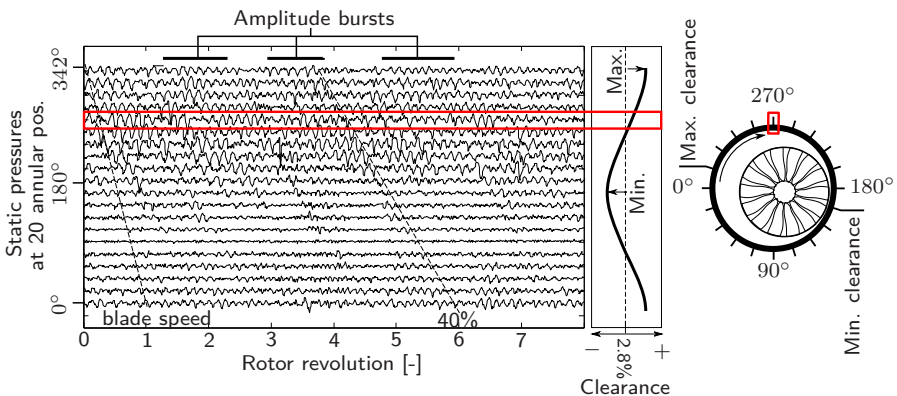


Figure 4.15: Casing static pressures at 20 annular positions in eccentric NG rotor operating at $\phi = 0.46$, (10 000 rpm)

little increased at sensor position $\varphi = 270^\circ$ which is about 70° circumferentially shifted with regard to the maximum clearance.

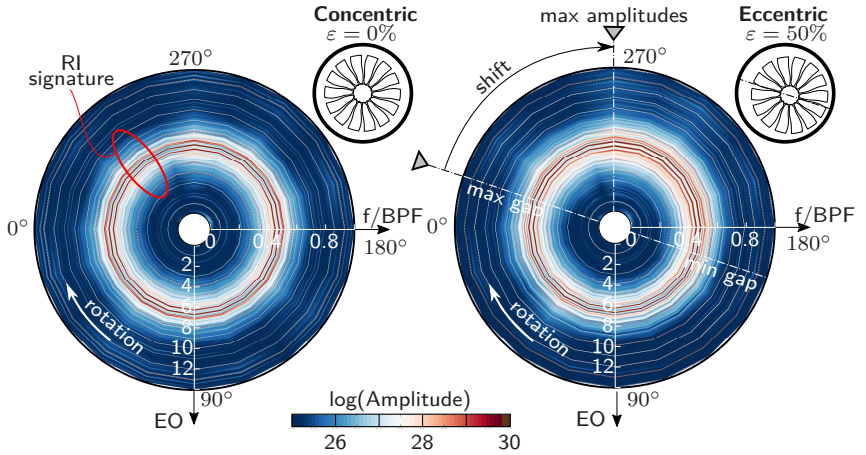


Figure 4.16: Fourier transforms at all 20 circumferential locations where the normalized frequency is plotted along the radius; LG ($\bar{\tau} = 5\%$) concentric (left) and eccentric (right) each operating at $\phi = 0.46$

Proceeding with the small clearance configuration in figure 4.17 there is little variety of amplitudes even under concentric conditions. Once the NG is eccentric, the redistribution of the spectral signature becomes even more explicit. The maximum amplitude within the signature is clearly exceeding the average one from the concentric case. Starting from the location of maximum clearance (at $\varphi = 342^\circ$), the maximum amplitudes are some 70° shifted in the direction of rotor rotation. Additionally, the signature is absent at sensor position PC7 which is just after the minimum tip gap. However, at each annular position, the single peaks remain within the same frequency range. This finding leads to a remarkable conclusion:

While changing the average clearance in a concentric rotor has an effect on shifting the signature into another frequency range, the local clearance in an eccentric rotor does not seem to do so.

The aim of the following analysis is to provide an overview of how the local signature of prestall instability in an eccentric rotor is changing while approaching the stall limit. For the respective configuration, only those operating ranges are

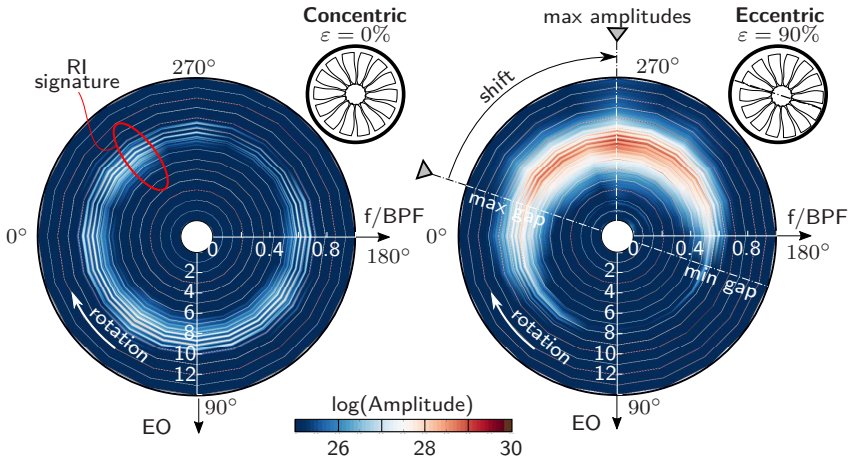


Figure 4.17: Fourier transforms at all 20 circumferential locations where the normalized frequency is plotted along the radius; NG ($\bar{\tau} = 2.8\%$) concentric (left) and eccentric (right) each operating at $\phi = 0.46$

shown in the total-to-static pressure rise characteristic at which the spectral signature could be noticed at any annular position (see figure 4.18).

What is already known from the analysis above is that RI is being initiated at higher flow coefficients when the average clearance is increased. When comparing the black and red colored speed lines, it turns out that an eccentric rotor has the preference to initiate RI slightly earlier. Considering the maximum clearance of the NG rotor to be almost equal to the average clearance from the concentric LG rotor, the inception point of RI is located at almost the same flow coefficient ($\phi \approx 0.54$). It is therefore suggested that, regardless of whether the rotor is concentric or eccentric, only the **local** clearance is specifying the overall onset of RI. However, to confirm a general validity of this statement, a combined clearance and eccentricity variation of increased parameter resolution would be necessary.

Further to this, when operating the eccentric NG at $\phi = 0.5$, the propagation area of RI is limited to a certain annular sector covering approximately 25% of the casing circumference. Also, the spectral pattern is only recognized just after the maximum clearance. While approaching stall, the annular sector affected by RI becomes successively widened, extending over almost 90% of the casing circumference at $\phi = 0.46$. The circumferential shift between the maximum clearance and the largest pressure amplitudes seems to be also depending on the flow coefficient. The time, the prestall instability needs to develop along a

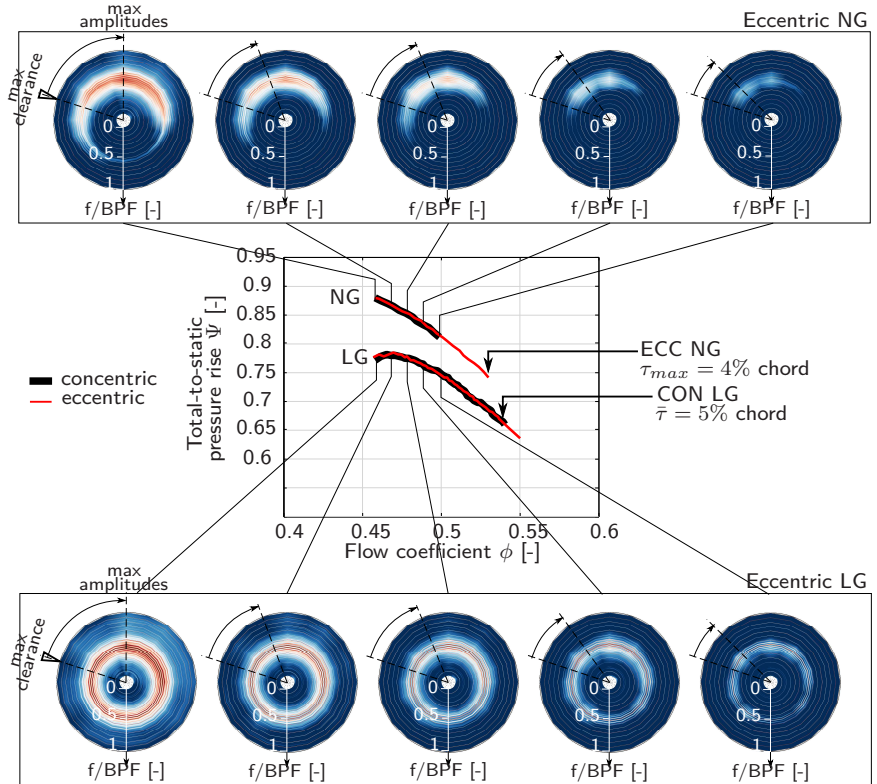


Figure 4.18: Operating ranges affected by the prestall instability RI; polar plots of Fourier transforms showing the uneven distribution of RI around the annulus when the rotor is eccentric

sinusoidal clearance distribution, appears to be linked to its own propagation speed since the spatial shift is almost equal for the NG and LG configurations.

4.6

Study of Prestall Disturbances

This section is aiming at improving the physical understanding of discrete flow disturbances causing the spectral signature of RI. For this purpose, data from the axially aligned sensor array was used to built quasi-instantaneous pressure

contours that cover at least multiple passages. Again, the phase-averaging presented in section 4.1.2 has been applied to the pressures recorded so that only the fluctuation in the rotor reference frame remain in the flow field.

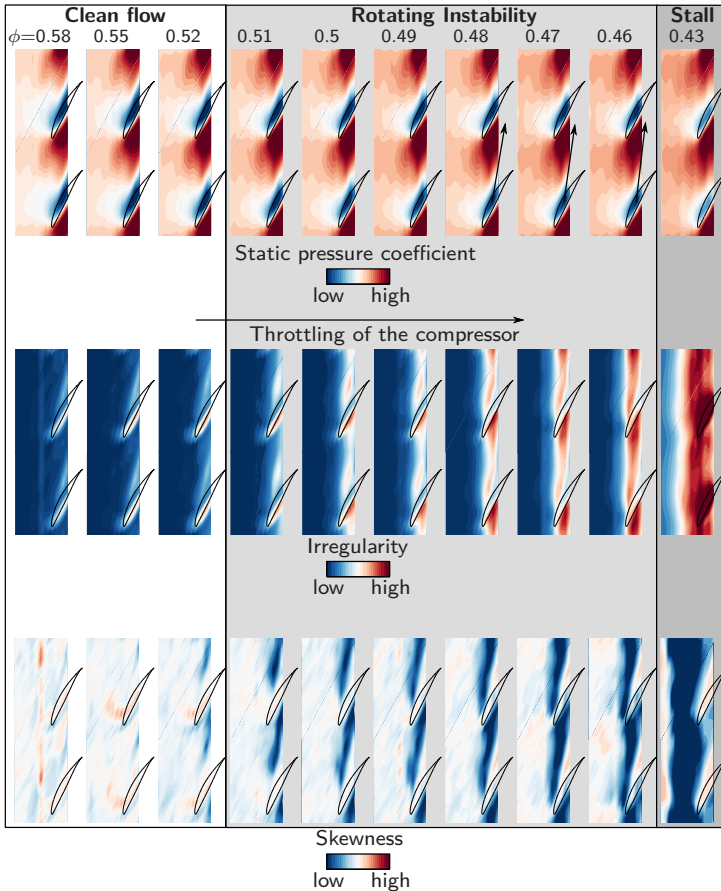


Figure 4.19: Phase-averaged static pressure, irregularity and skewness contour plots on the casing wall for different operating points; concentric NG rotor

In section 4.3, statistical moments "irregularity" and "relative skewness" have only been investigated as integral values. Using now the time-resolved pressures from the axial sensor array and repeating the step-wise procedure up to step (4) allows to obtain so-called irregularity and skewness contour plots

phase-locked to the rotor. Selected contour plots from operating points between $\phi = 0.43 - 0.58$ are shown in figure 4.19 whereby only two passages are presented. One can clearly see the peak suction which becomes abruptly reduced when transitioning into stall. While throttling the compressor, the axial static pressure built-up is successively increased. A traditional approach of assessing the alignment of the clearance vortex bases on identifying a thin trace of negative pressures originating from the peak suction of the compressor blades. Since the transducer array covers the front half of the rotor passage, the TCV trajectory can only be recognized unambiguously when the compressor is operating close to stall (at $\phi = 0.46 - 0.48$). However this trend applies to the nature of the TCV being shifted in the upstream direction when reducing the mass flow.

Moving on to consider the irregularity pattern, a thin trace of increased fluctuations originating from the suction surface of the blade and then extending in the downstream direction is already visible at $\phi = 0.58$. While approaching towards stall, the level of irregularity increases and the trace is continuously being shifted in the upstream direction even reaching the pressure side of the

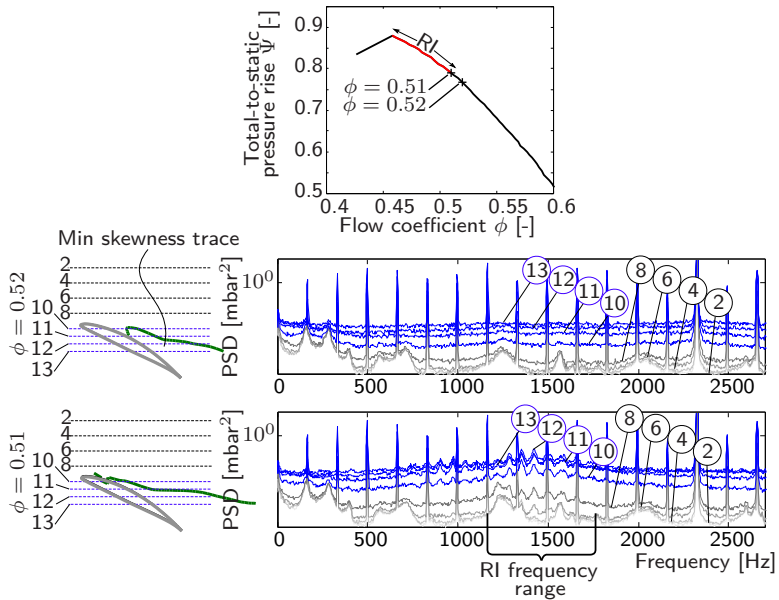


Figure 4.20: Fourier analysis at various axial locations at an operating point without RI ($\phi = 0.52$) and at RI inception ($\phi = 0.51$), concentric NG rotor

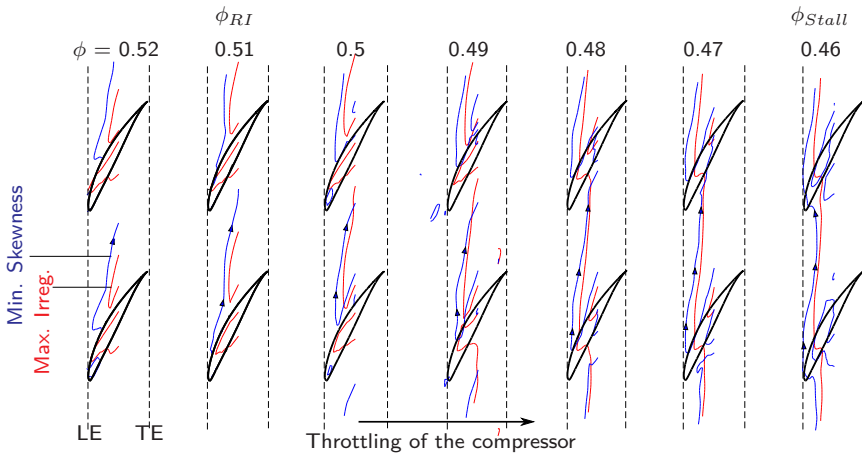


Figure 4.21: Phase averaged trajectories of minimum skewness and maximum irregularity (RMS) for various flow coefficients; concentric NG rotor

neighboring blade starting at $\phi = 0.48$. A similar trend also applies for the skewness indicating the propagation area of negative pressure spikes to be always located inside the passage except for the stall point. The abrupt change in flow pattern will be discussed in section 4.8. Also, taking into account the TCV trajectory, both irregularity and skewness traces appear to be extending upstream of the clearance vortex. This leads to the conclusion that the low pressure perturbations arise in the shearlayer between the TCV and the incoming main flow.

Another important finding can be made by turning back to the transition from undisturbed flow into RI. Two operating points representing exactly those flow conditions have been used for this purpose and a Fourier transformation was applied to the pressure data obtained from the PA array (see figure 4.20). Already at $\phi = 0.52$ first signs of emerging disturbances can be observed based upon the trace of negative skewness clearly developing inside the passage (PA10-PA13). However, the spectral signature of RI is missing in that area. The broad banded chain of peaks becomes only visible at $\phi = 0.51$ showing maximum amplitudes at position 12. Thus, the mere existence of discrete propagating flow disturbances does not necessarily lead to the initiation of prestall instability. To better comprehend the trajectory of propagating flow disturbances being shifted with throttling, a gradient based analysis method has been applied to the pressure contours which identifies the local minimum

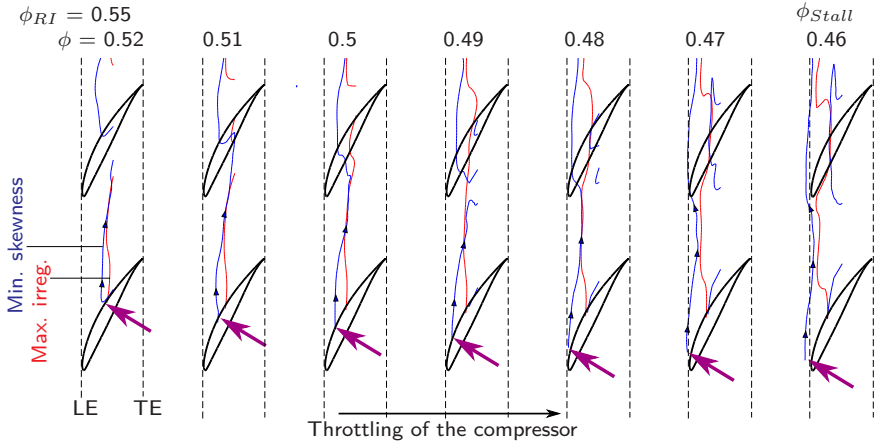


Figure 4.22: Phase averaged trajectories of minimum skewness and maximum irregularity (RMS) for various flow coefficients; concentric LG rotor

in skewness and the local maximum in irregularity. The results are shown in figure 4.21.

A feature which only becomes visible when analyzing the trajectories in one plot is that the skewness trace (blue line) is located slightly upstream of the one which belongs to the irregularity (red line). It is therefore suggested that the red line is indicating the exact location of the shear layer developing between the TCV and the main flow while the flow disturbances are moving along this shear layer. When considering the trajectory at ϕ_{stall} to be almost aligned in parallel to the rotor inlet plane, the reasonable conclusion is that stall is only being initiated once the prestall disturbances succeed in travelling around the leading edge of the neighboring blade. These results are quite delicate in the sense that they might hint a new type of stall inception. Regardless of that assumption, the propagation area tending to be more and more concentrated close to the leading edge plane will later be used to predict an upcoming stall event.

Another crucial finding can be made by analyzing the traces of minimum skewness for the LG configuration. Starting at $\phi = 0.52$, the true origin of minimum skewness on the suction side of the blade (indicated by a red arrow) is seen to be located at about 50% axial rotor chord. The origin is successively shifted in the upstream direction while throttling of the compressor. This leads to the fundamental conclusion that prestall disturbances **cannot** be caused by a

leading edge separation. If the latter was true, the origin of the trace would always be located on the rotor leading edge.

Facing the question of how the disturbances look like at discrete points in time and whether they are belonging to a more complex flow structure, casing pressure contours have been analyzed at discrete points in time. The creation of quasi-instantaneous pressure contours bases on measurements phase-locked to the rotor and can be described as follows: While keeping the flow coefficient ϕ constant, the axially aligned sensor array sampled the static pressures over the duration of one complete rotor revolution. The signal has then been plotted over an entire casing circumference resulting in a 360 deg pressure contour. Finally, the blade passing signal being an average from a total of 100 revolutions was removed from this contour plot so that only the fluctuation part remained.

The results for three selected operating points recorded in the NG rotor are summarized in figure 4.23. At $\phi = 0.52$ (figure 4.23 a)) the 360 deg scan on the left side shows an exemplary contour plot of the absolute static pressure coefficient. Removing the ensemble-averaged blade passing signal from this sequence leads to the pressure contour shown on the center of figure 4.23 a). Small-scale disturbances of low amplitude clearly emerge as patches of low pressure within a few rotor passages (1-2, 6-7, 8-9, 10-11). However, these local pressure minima are always located on the phase-averaged skewness trajectory which is depicted on the right side of the figure triplet 4.23 a).

A quite more complex flow topology can be observed when turning to the operating point $\phi = 0.51$ at which the spectral signature of RI could be noticed for the first time. While there is little variety of the static pressure coefficient from one passage to another (figure 4.23 b) left), however, the fluctuation contour in the center shows a certain number of circumferentially skewed flow structures not to be limited to the front half of the passages but also reaching up to almost 50% chord upstream of the rotor inlet plane. Any patches of low pressure still obtained just aft of the leading edges can be interpreted as part of these flow structures. When considering the last stable operating point with RI (figure 4.23 c)), the topology of the prestall flow structure becomes even more distinct. While the overall level of pressure fluctuations has significantly increased, the alignment of the TCV trajectory also appears to be noticeably affected by the discrete flow structures propagating around the annulus. Additionally, the latter now extends to almost 100 % axial rotor chord upstream of the leading edges. When comparing especially the operating points $\phi = 0.52$ and $\phi = 0.51$, the spectral signature seems to be strictly associated with the existence of circumferentially skewed flow structures rather than patches of intense low pressures exclusively arising inside the rotor passages.

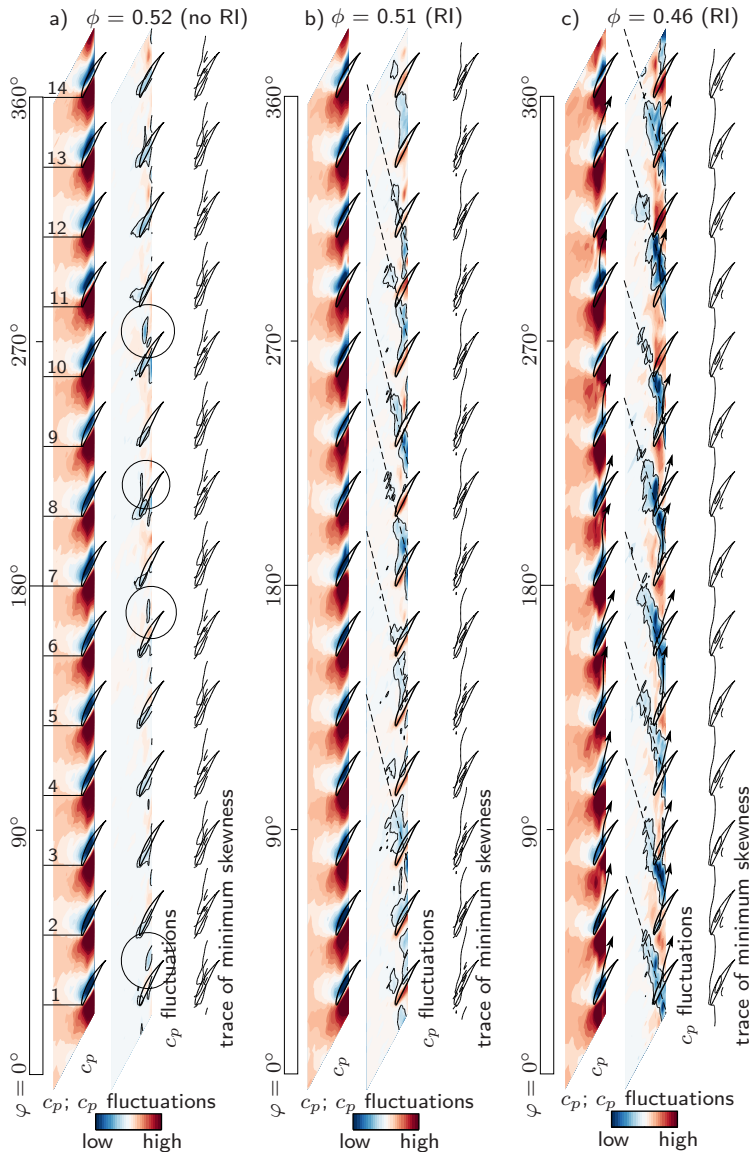


Figure 4.23: Quasi-instantaneous static pressure contours and trajectories of negative skewness; concentric NG rotor

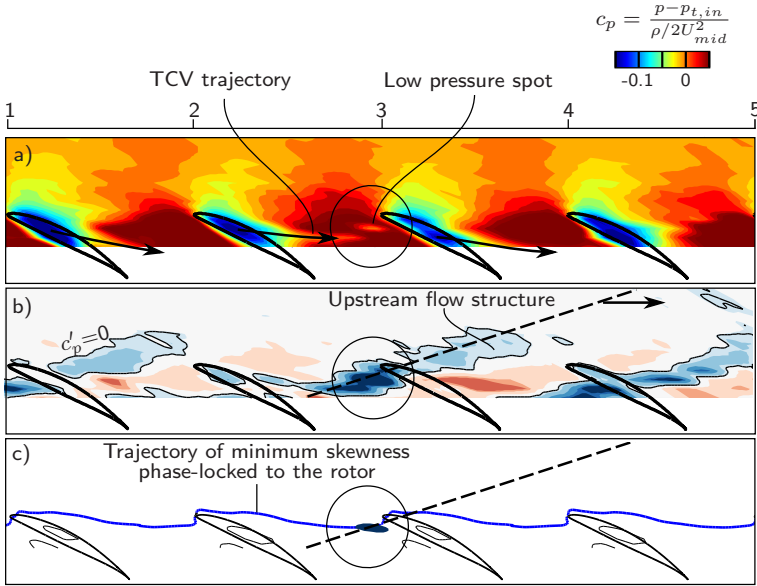


Figure 4.24: Detailed propagation mechanism of prestall flow disturbances and interaction with TCV; a) absolute casing static pressure contour at a quasi-instantaneous time, b) static pressure contour reduced by the phase-averaged blade passing signal, c) trajectory of minimum skewness; concentric NG rotor operating at $\phi = 0.46$

A cut-out from the set of contours at $\phi = 0.46$ is examined more closely (see figure 4.24). The local pressure spots appear to belong to a much more complex flow phenomenon than previously assumed by Young et al. (2013) [64]. A further advantage of this illustration is that it provides initial indications of the interaction mechanisms between the TCV and the discrete flow structure passing by. The first important thing to notice in the absolute static pressure contour in figure 4.24 a) is a local pressure minimum inside the passage 2-3. Right here, the TCV trajectory extends even along the rotor inlet plane while the neighboring passages are behaving quite differently. Since the local pressure minimum is located ahead of the TCV trajectory, the assumption about prestall disturbances arising in the interface between the TCV and the incoming flow is hereby confirmed. In figure 4.24 c), the travelling flow structure in its entirety becomes clearly visible by an isocontour line at $c_p = 0$ indicating its outer boundary. A dashed line supports a better comprehension of the alignment of the upstream flow structure. When considering the remaining passages in figure 4.24 b), the low pressure spot seems to be always flushed with the flow

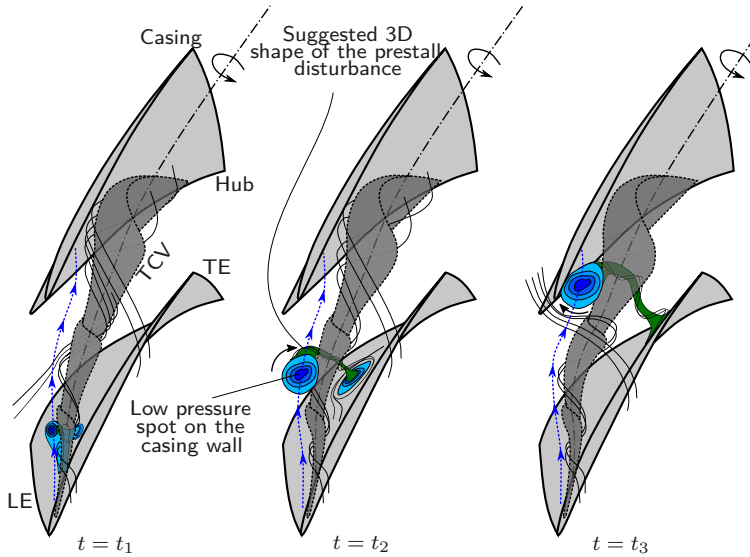


Figure 4.25: Schematic of the formation and the propagation of prestall vortex structures in a rotor blade passage at stable flow coefficients

structure while at the same time propagating along the trajectory of minimum skewness shown in figure 4.24 c). Also, it appears to be true that the flow structure is causing the displacement of the TCV trajectory and not vice versa. A clear indication can be found in passage 1-2 where the propagating flow structure covers almost one blade pitch while originating on the suction side at about 25% chord. Therefore, the formation of the local pressure minimum must be imminent at this point in time. However, there is no evidence at all that the TCV is turned in the upstream direction. This leads to the conclusion that the flow disturbance arises **first** and the replacement of the clearance vortex is initiated **afterwards**.

It has often been suggested that the prestall disturbances are linked to radial vortices whereby the negative pressures on the casing wall are caused by increased vortex induced velocities. Taking into account the aforementioned experimental results, the presumed time-resolved formation and propagation of prestall disturbances in a rotor blade passage is schematically shown in figure 4.25. At time step t_1 the TCV colored in dark grey extends in almost downstream direction without inducing forward spillage of the clearance flow. Formation of the prestall flow structure (colored in green) is seen to be initiated

near the leading edge as a consequence of the boundary between the TCV and the incoming main flow becoming destabilized. At step t_2 the suggested coherent structure becomes grown while continuously moving in pitch-wise direction. At this point in time, the highly three-dimensional disturbance shows exactly the same vortex flow topology as the so-called "separation vortex" reported by Inoue. While spanning across the TCV, the vortex tube behaves like a cylindrical roller bearing allowing the main flow to physically slide on the TCV. It is also assumed that the RI vortices represent the disturbances of a fully developed Kelvin-Helmholtz Instability forming in the highly three-dimensional shear layer that envelops the TCV. At time step t_3 the end of the vortex tube attached to the casing wall approaches the adjacent blade without entering the neighboring passage. However, the vortex induced velocities cause the main flow to be redirected into the neighboring passage where the predominant shear layer is likewise destabilized. Enclosed between the pressure side and the TCV, the casing end of the prestall vortex is most likely displaced or dissipated hereafter while the vortex end attached to the suction side finally migrates downstream.

Summarizing, prestall vortices are supposed to be representing the disturbances of a Kelvin-Helmholtz Instability developing in the shear layer between the TCV and the main flow. Since the shear layer enclosing the TCV is highly three dimensional, the trajectory of the prestall vortex filament must be equally three dimensional.

4.7

Statistics of Prestall Disturbances

In the previous section, it has been clarified how the flow disturbances causing the rise in irregularity look in detail and how they change in the course of throttling. By analyzing the casing static pressure contours covering the whole annulus, a finite number of disturbances unevenly distributed around the circumference could be identified. However, the question as to how the circumferential count can be related to the spectral signature is still partially unanswered. To address this, many sequences recorded at the last stable operating point have been used to repeatedly count the number of disturbances. Another step is being required in order to properly put this number into relation to the mode spectrum in figure 4.12. Again, the static pressure contour is a quasi-instantaneous one, representing a spatial pattern that also includes a time-domain. By recording an entire rotor revolution at this operating point close to stall only 40% of the disturbances passing by have been captured

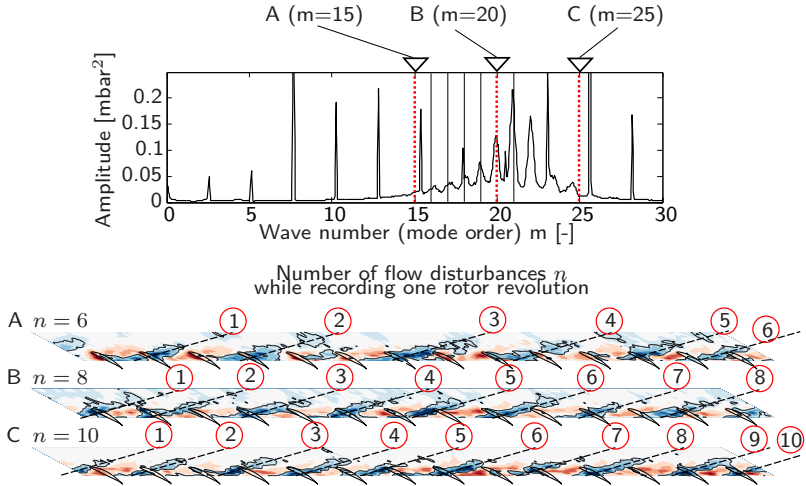


Figure 4.26: Mode spectrum and quasi-instantaneous pressure contours reduced by the phase-averaged blade passing signal - Changing circumferential count of prestall flow disturbances while keeping the flow coefficient constant at $\phi=0.46$; concentric NG rotor

since they are propagating at just 40% rotor speed. To get the number of disturbances m actually existing, the corresponding count n detected in the scan must therefore be multiplied by the reciprocal of their own speed k_{RI} .

$$m = n \cdot \frac{1}{k_{RI}} \quad (4.8)$$

Three randomly selected contours of static pressure fluctuation (A-C) are shown in figure 4.26, where the number n varies between 6 to 9 from plot to plot. When transferring the visible number into the one actually present, resulting mode orders of $m = 15, 20, 25$ are found to be part of the signature in the mode spectrum. The results just provide a first indication that a certain peak can be assigned to a certain number of propagating flow disturbances. To appropriately confirm this relationship, identifying the number was carried out for a total of 1500 rotor revolutions. In detail, an algorithm finding the prominent local pressure minima has been applied to the static pressures recorded at PA11, since almost the entire trajectory of minimum skewness is located at this axial position. At first, static pressures were recorded over one revolution and the ensemble-averaged blade passing signal was then removed from the data. The number of negative pressure spikes was determined based upon the

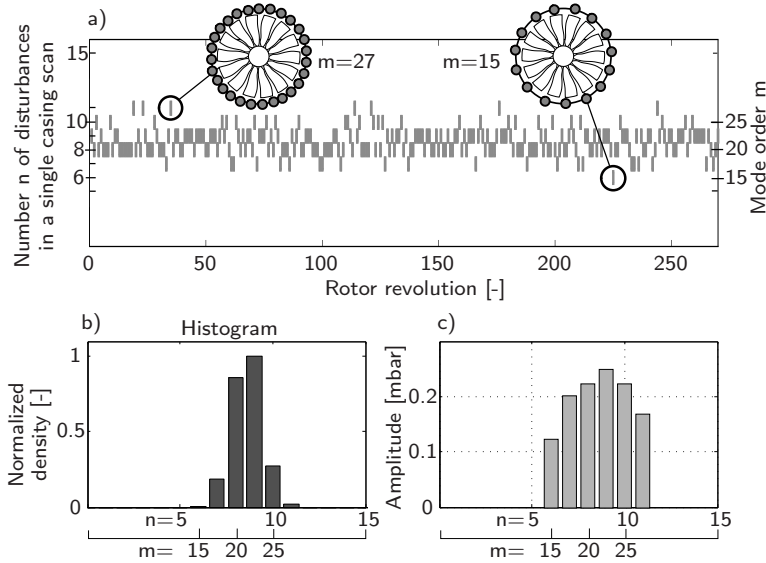


Figure 4.27: Detection of prestall disturbances- a) circumferential count of disturbances (N. of d.) identified at each rotor revolution; b) probability of circumferential counts (density normalized by the amount of the most likely number to occur); c) mode-dependent pressure amplitudes; NG rotor, $\phi=0.46$

aforementioned algorithm and subsequently saved as a single value representing the quasi-instantaneous number of disturbances for the first revolution. Considering figure 4.26 for example, six disturbances have been counted at revolution A, eight disturbances at revolution B and nine disturbances at revolution C. Additionally, the mean of all pressure values corresponding to each minimum has been calculated and saved as an equivalent to the mode amplitudes. Finally, the previous steps have been repeated for 1500 revolutions. The data series processed serve for the statistics presented in figure 4.27.

By plotting the number of disturbances over rotor revolution as depicted in figure 4.27 a) one can see a number that arises randomly distributed over time in a range between $n = 6 - 11$. The corresponding mode order m or the actual circumferential count can be investigated when multiplying the number by the reciprocal of their propagation speed k_{RI} . Resulting mode orders between $m = 15 - 27$ thus mirror the whole range which was also found within the signature of the mode spectrum. Although the approaches are completely different, the pattern in figure 4.27 a) reminds hardly of stochastically distributed mode

amplitudes obtained by Pardowitz (2018) [49]. Furthermore, the probability distribution in the histogram (figure 4.27 b)) shows that disturbances being arranged in a circumferential count of about $m = 22$ are arising most frequently. The following conclusion can be drawn:

The dynamics of prestall flow disturbances is not only represented by the constantly changing circumferential count but also in the probability distribution revealing the very count inducing the highest pressure amplitudes to be most likely over time.

4.8

Rotating Stall - Rotating Instability

This section aims at investigating the complex interaction mechanism between RI and stall cells along the stalled branch of the pressure rise characteristic. It has already been shown that both phenomena are existing simultaneously where the speed of prestall disturbances and cells are clearly differing from each other. This finding gave rise to question as to how both phenomena do actually interact and where both of them are to be located within the rotor section. Before taking a step in this direction, pressure data recorded at one annular position has been used to assess the stall cell dimension. Again, the ensemble-averaged blade passing signal has been removed for this purpose.

The operating point assigned to the peak of the pressure rise characteristic reveals there is no evidence of any stall cell structure (see figure 4.28 at $\phi = 0.46$). In contrast, when operating under stalled conditions at $\phi = 0.43$, the pressure trace has a non-uniform distribution of Irregularities. One can clearly derive the extent of the stall cell from the percentage of the period of time affected by a high level of pressure fluctuations. The stalled sector covers about 60% of the rotor circumference. Considering the in-stall part of the characteristic indicating part span stall, the cell extension must look very similar to the one shown in the schematic illustration (greyed area). A further throttling on the secondary characteristic leads to an increase in stall cell size. At $\phi = 0.42$ the average cell extension is about 75%. The casing static pressures measured simultaneously by the axially aligned transducer array are now investigated to get a first idea of how the discrete disturbances of sub-pitch dimensions are becoming redistributed caused by stall cell propagation (see figure 4.29). In detail, the unprocessed pressures recorded inside the passage (PA9-12) has

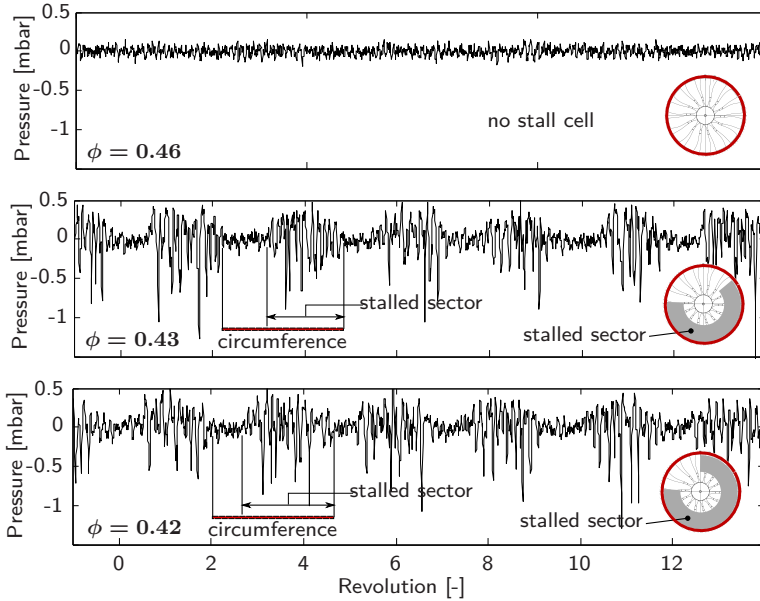


Figure 4.28: Static pressures recorded at PC1 (pressures low-pass-filtered at $f = BPF/2$). Increase of stall cell expansion while reducing the mass flow on the stalled branch of the pressure rise characteristic, concentric NG rotor

alternating periods of time where the peak suction of the blades is significantly reduced which means that the rotor flow is disturbed in these sections. Hence, they give an indication of the stall cell location. In contrast, groups of distinct low pressures are recognized in the signal obtained by the upstream sensors (PA1-8) in those periods of time where the stall cells are being present. Additionally, the spikes have largest amplitudes at PA5 which is 50% axial chord upstream of the rotor inlet plane. Taking into account the axially installed pressure transducers to be also placed a fraction of pitch apart from each other, however, the disturbances appear to be positioned upstream of the cells.

To receive an overall understanding of the chronological evolution of propagation, every second annular static pressure is plotted against rotor revolution (see figure 4.30). Despite the sacrifice of spatial resolution, both the cell and even the disturbances can be traced while moving from $\varphi = 342^\circ$ towards $\varphi = 0^\circ$ (indicated by the black arrows). Here the cell needs about 2.3 rotor revolutions to move along the whole annulus. The reciprocal value is 0.44 which is in very

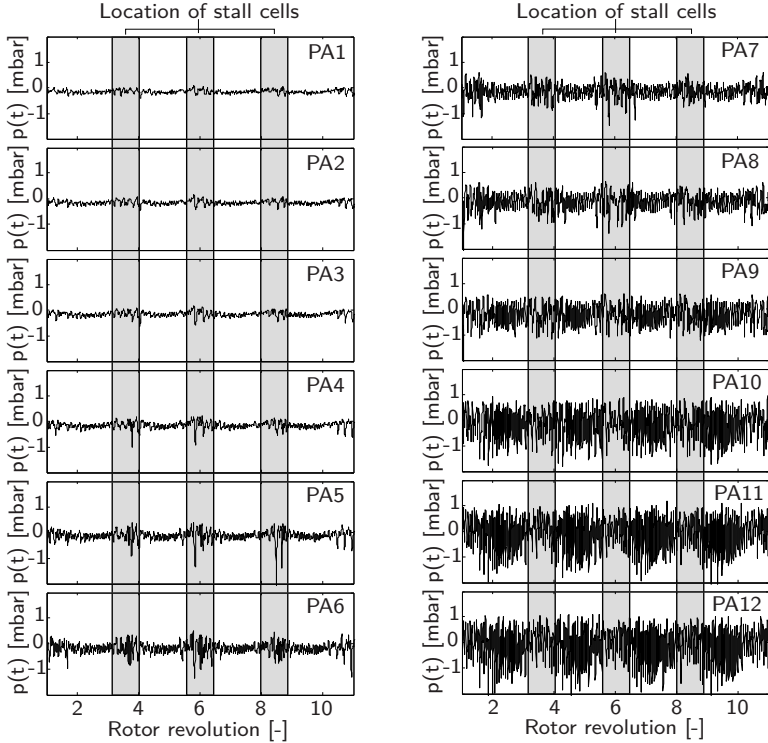


Figure 4.29: Unfiltered casing static pressures at 13 axial positions (PA), concentric NG rotor operating at $\phi = 0.43$

good compliance with the fraction of cell speed $f_{RS}/f_{rotor} = 0.44$ obtained in figure 4.10. The same applies for the disturbances that need about 1.8 revolutions resulting in $\Delta f_{RI}/f_{rotor} = 0.55$.

Since the slope of the trajectory left by the disturbances is marginally steeper than the one left from the cell, the difference in speeds is thus confirmed. Also, when entering the stalled sector, the intensity of disturbances seems to be successively increased. In contrast, once leaving the stalled sector, the disturbances are losing a considerable amount of pressure amplitude (circled in red).

Summarizing, the stall cell appears to be acting as an amplifier for the aerodynamic disturbances. The foregoing analysis provided the evidence of disturbances to be relocated upstream of the rotor. The interaction between part-span stall and prestall disturbances is vividly illustrated in the casing static pressure con-

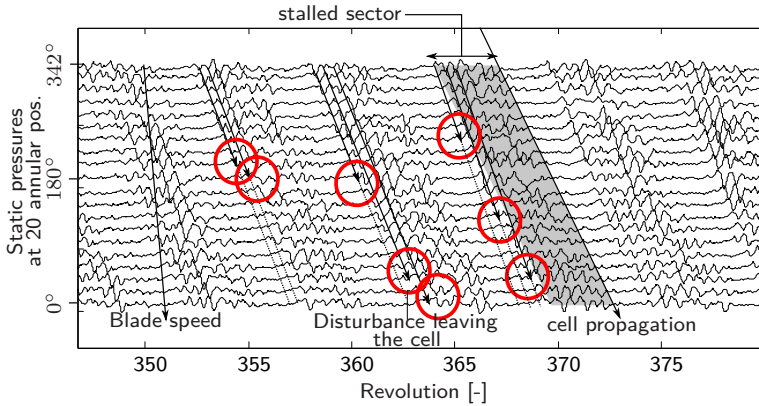


Figure 4.30: Casing static pressures at 20 annular positions each low-pass filtered at $f = BPF/2$, Differing propagation speed of prestall disturbances and stall cell, concentric NG rotor operating at $\phi = 0.43$

tours extending over three rotor revolutions (figure 4.31). While the sequence area showing compressor blades with a pronounced peak suction is representing the unstalled sector, however, every passage from the stalled sector (enclosed by the greyed shaded area) has a substantially reduced peak suction indicating a decreased aerodynamic blade loading. Also, each passage flow is disturbed in that area. Further to this, when comparing the different flow regimes, small patches of low pressure identified in the unstalled sector are clearly located inside the passages (zoom a)) whereas in the stalled sector, spikes of increased pressure amplitudes have been shifted upstream of the compressor rotor (zoom b)). This seems to be a remarkable finding since the disturbances in the unstalled sector (zoom a)) are behaving quite equal to the ones obtained at stable flow coefficients (figure 4.24).

It should be mentioned that the interaction shown might only be restricted to low pressure machines, however another few publications have already addressed the coexistence of RI and RS based upon frequency analyses [25, 51]. It is even suggested that the flow field presented at post stall operation is exactly the same Inoue et al. (2002) [33] investigated under the subject of "short-length scale stall cells". Accordingly, the superimposition presented in this work would be exactly what they described as a "long-length scale wave overlapping multiple short-length-scale waves".

Taking into account the vector flow maps in chapter 3, the low pressure spots observed in the rotor are virtually assured of being caused by a vortex

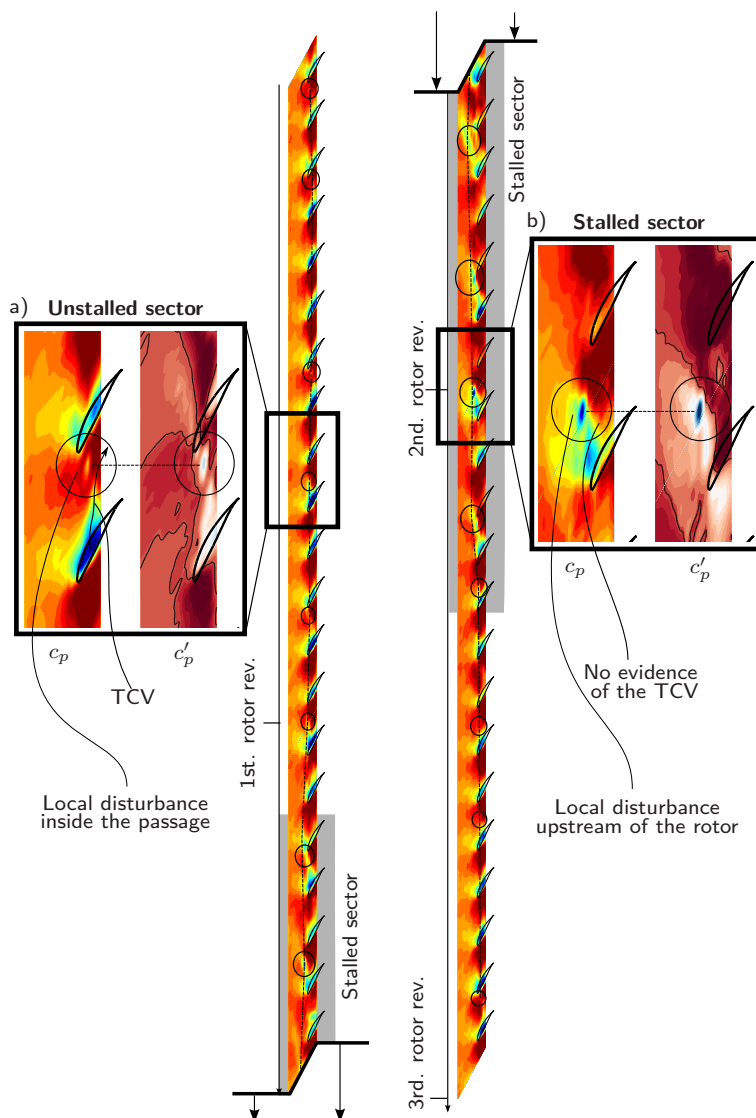


Figure 4.31: Quasi-instantaneous casing static pressure contours illustrating stall cell expansion and redistribution of prestall flow disturbances within the stalled sector, concentric NG rotor operating at $\phi = 0.43$

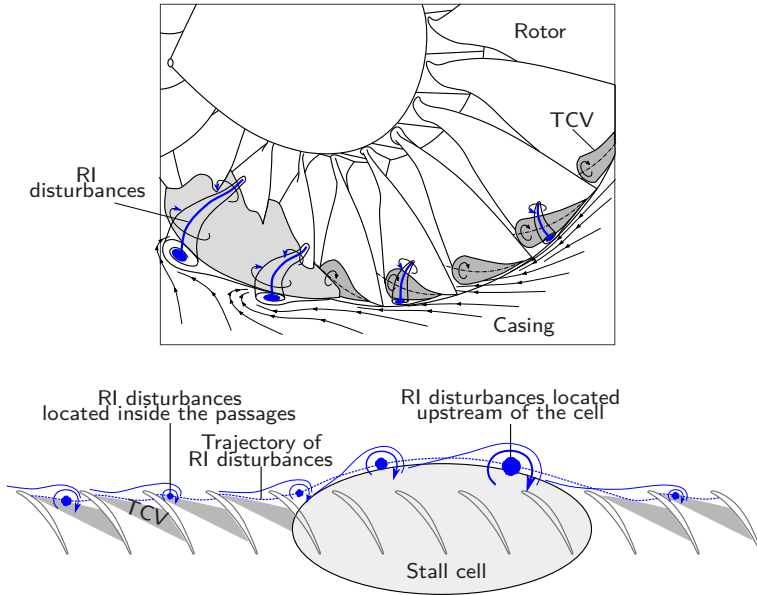


Figure 4.32: Schematic of interaction between stall cell and RI disturbances

that is of the same structure as an Inoue-type radial vortex. The coexistence, redistribution and reasonably suspected 3D shape of RI disturbances in a rotor is schematically summarized in figure 4.32. The propagation area therefore extends either along the interface between TCV and main flow (unstalled sector) or the interface between stall cell front and main flow (stalled sector).

4.9 Transition Into Stall

Since the prestall flow field is already characterized by considerable amount of pressure fluctuations and the pressure pattern of RI disturbances can hardly be distinguished from those of a classical spike, it is even more essential to study the precise inception type with RI present beforehand. The type of stall inception mechanism is traditionally detected using at least six sensors measuring at high temporal resolution (unsteady pressure transducers or hot wire sensors) in close proximity to the leading edge, evenly distributed around the casing circumference. Using a digital low-pass filter, the blade passing frequency is removed from each signal to resolve the first sign of any small disturbance and to subsequently track it while travelling from one probe position to the next.

The transient evolution from prestall instability to rotating stall can be appropriately investigated since the instrumentation used in the present setup is meeting all the requirements for the aforementioned traditional approach. While the compressor is slowly throttled, any signal has been recorded simultaneously including the ones from the Prandtl tube, the circumferential transducer array and the static pressure taps downstream of the compressor stage (sampling at 48 kHz). All signals except for the over-tip static pressures has been divided into sequences with a length of 300 samples, each of which was used for processing the total-to-static pressure rise coefficient. The length of 300 samples leads to an integral value over two full rotor revolutions.

The latter is shown in figure 4.33 a). One can clearly recognize the time of stall onset by the sudden drop of pressure rise between revolution 160 and 182. The inception process can now be studied in detail using the annular static pressures post-processed within this brief period of time. First, the low-pass filter was set to $f = BPF/2$ to remove the blade passing frequency from each signal. Resulting traces are plotted over rotor revolution as shown in figure 4.33 b).

It is quite ambitious, certainly impossible, to diagnose spike stall inception, as it is almost inconceivable to distinguish a spike from the numerous RI disturbances existing well before stall onset. What can be seen from positions PC7/PC8, though, is a small group of disturbances with increased amplitudes initiating stall cell formation (circled in red in figure 4.33 b)). The pattern subsequently grows into a fully developed cell just within 10 rotor revolutions. A reasonable explanation regarding the transition process into stall could be as follows: Due to the increasing aerodynamic blade loading, the TCV trajectory is more and

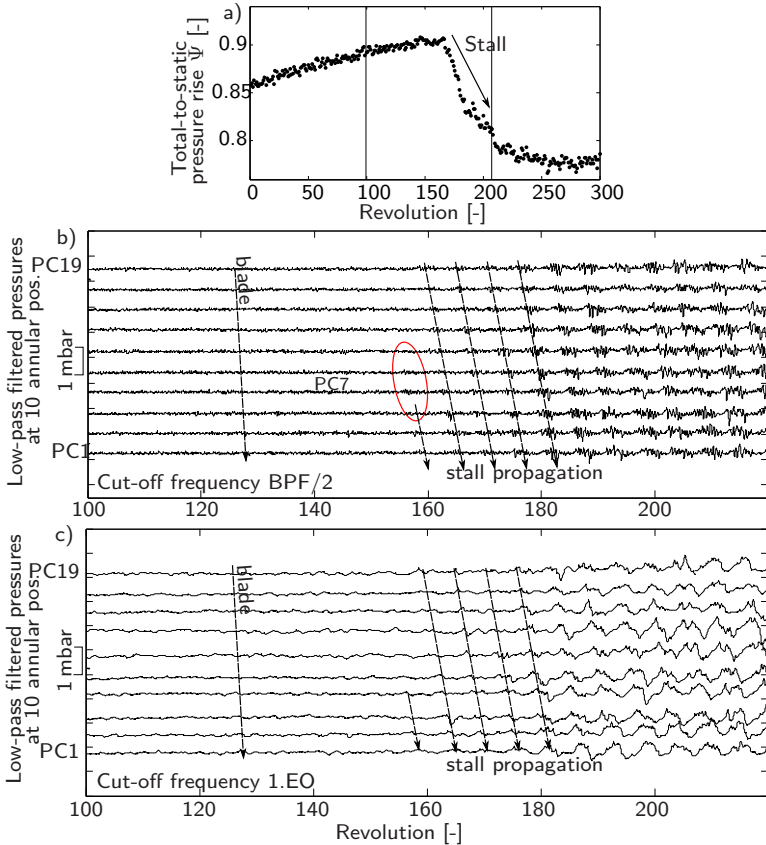


Figure 4.33: Transient low-pass filtered static pressures at 10 annular positions, traditional stall inception traces, concentric NG rotor

more aligned in parallel to the rotor inlet plane. Same is true for the trace of radial vortex structures relocated in the same direction until one, or much more likely, several disturbances are hitting the opposing leading edge causing flow separation on the respective blade. It is suggested that RI disturbances are adopting the physical mechanism of classical spikes at this particular moment. The subsequent propagation mechanism and growth into a stall cell would be according to what is already known from the spike stall inception. A quite similar observation, however, was made by Young (2017) [65] reporting the inception mechanism in an eccentric rotor much harder to identify due to the

formation of "large disturbances" developing in the large tip clearance sector. When applying a low-pass filter set at $f = 1.EO$ (figure 4.33 c)), the amplitude bursts of prestall flow disturbances become visible as harmonic waves. They should not be confused with modal stall inception since in the period of time between revolutions 100-160 their amplitudes are not growing exponentially with time but continuously decaying in a random order.

4.10 Potential for Stall Warning

To maintain safety and reliability in flight operations, the operating point of an axial compressor should be at a safe distance from the stability limit. Engine control systems are executing the task of keeping the operating point sufficiently far away from the surge line even at transient maneuvers. However, considering high levels of compressor efficiencies to be located close to the stall limit, the pursuit of reducing the unused safety margin is immense. This demand inevitably goes hand in hand with developing a reliable system that is warning of an imminent stall event. Over many decades, several stall warning systems emerged trying to detect modes or spikes involved in the early stage of stall inception. However, these systems achieved limited success since modes and spikes are extremely short-lived transitioning into a cell just within a brief period of time.

The present work shows an alternative approach by stepping back from the near stall operating point and seeking for any first sign of flow irregularities as the compressor is successively being throttled. The assessment of prestall instabilities seems to be most promising for this purpose. Remembering the distribution of irregularity plotted against the flow coefficient, a ramp-up was clearly indicating the rise of pressure fluctuations in the rotor reference frame. In a more recent paper, Young et al. (2013) [64] attempted to use this characteristic by introducing a threshold in the level of irregularity. Once crossing this threshold, the warning system gives an alarm. However, using the rise of irregularity this way appeared to be not as expedient as previously anticipated since both average tip clearance and rotor eccentricity turned out having a major impact on the ramp-up. So the threshold level defined at an instant of time becomes most probably invalid through the life of the engine. A much more promising indicator is found when assessing the absolute skewness applied to the casing pressure data measured at discrete flow coefficients. The

advantage of using this parameter is that it is not necessary to pre-process the pressure data based on the phase-averaging procedure presented in section 4.1.2. When plotting the skewness against flow coefficient, there is evidence of at least one critical point in the more or less continuous distribution. The respective minima and maxima are found by computing the piece-wise derivative of the skewness graph as shown by the red colored line in figure 4.34 a). The local minimum indicated by the first zero-crossing of the skewness' gradient is denoted as alarm level 1 (AL1). The second zero-crossing, if present, highlights warning level 2 (WL2) which is seen as much more progressive level as it is located in closest proximity to the stability limit.

To examine the variation of the stall warnings functionality around the whole circumference, the skewness gradient has been assessed at each PC location individually. The mere warnings levels (AL1 and AL2) have been transferred into the polar plot in figure 4.34 b). Both levels are a function of the stall margin quoted as a percentage of the stalling flow coefficient (adapted from Cumpsty [14]).

$$\text{Stall margin} = (\phi_{op} - \phi_{stall}) / \phi_{op} \cdot 100\% \quad (4.9)$$

While plotting the stall margin on the radial axis, the stability limit lies on the polar plots center. For the concentric LG rotor (figure 4.34 b)), there is only small variation of each warning level still present over the entire casing circumference.

Turning to the concentric NG rotor (figure 4.35 b)), only the conservative AL1 is present with AL2 absent at each annular position. Also, AL1 varies between 2% and 5% stall margin indicating the warning system to be more sensitive when the average clearance decreases. Though, the mean of each circumferential AL1 is located further apart from the stability limit than the AL2 does for the LG configuration. Summarizing, the intended preliminary stall warning is assured when considering at least AL1. In principle, the warning levels could also be used to assess the deterioration in tip gap height as part of an engine health monitoring system. Hence, an alarm level being shifted towards higher mass flow rates would indicate an increasing tip clearance.

4.10.1 Influence of Rotor Eccentricity

In section 4.5, a non-uniform clearance caused a significant redistribution of the spectral RI signature over the annulus. Complementary approaches revealed

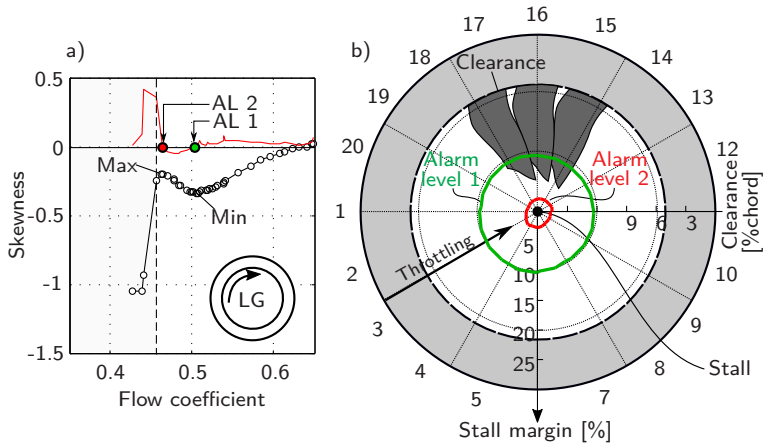


Figure 4.34: Absolute skewness as a function of flow coefficient / stall margin - left: average skewness from all 20 circumferential sensors, right: circumferential skewness as a function of stall margin (minimum marks location of alarm level 1 "AL1", maximum corresponds to alarm level 2 "AL2"); concentric LG rotor

the maximum pressure fluctuations induced by the prestall instability RI to be circumferentially shifted some 70 deg to the maximum clearance. This finding gives a first indication about the stall warning system strongly depending on the existence of RI to be seriously affected by rotor eccentricity. The procedure of investigating the stall warning levels based upon the polar plot is repeated for each eccentric setup. The average alarm level from all PC data is shown in figure 4.36 a) whereas the levels obtained at each circumferential location individually are displayed again in the polar plot in figure 4.36 b). Turning to the polar plot, both warning levels (AL1 and AL2) appear to behave quite similar to the concentric LG rotor. Anyhow, the warning levels are seen to occur just after the maximum tip gap having a circumferential offset between 40-100 deg in the direction of rotor rotation. This finding about the shift is in good compliance to the results presented in figure 4.18 where the phase lag of the non-uniform distributed spectral signature was found to be varying in range between 45-90 deg. A fundamentally different behavior can be observed for the eccentric NG case (see figure 4.37). Unfortunately, any stall warning is absent within the sector enclosed by PC7 and PC15. The sector affected is centered around the minimum clearance position.

While only AL1 is present in the lower right sector, AL2 is additionally appearing in the further course of the rotor direction. However, when averaging all warning

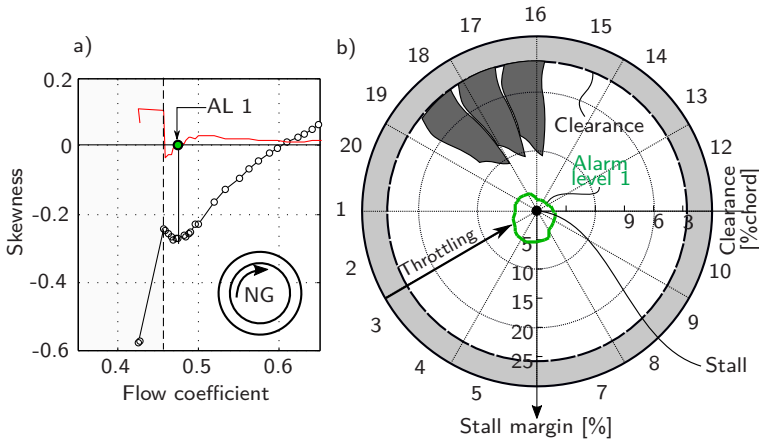


Figure 4.35: Absolute skewness as a function of flow coefficient / stall margin - left: average skewness from all 20 circumferential sensors, right: circumferential skewness as a function of stall margin (minimum marks location of alarm level 1 "AL1"); concentric NG rotor

levels from the 20 circumferential positions there is no stall warning at all (see figure 4.37 a)). This means that at least four pressure signals measured evenly distributed around the annulus need to be monitored individually to ensure reliable stall warning in case of an eccentric rotor.

4.10.2 Influence of Axial Measurement Position

Again, the primary attempt of the stall warning indicator presented is to reduce the required design safety margin which is only guaranteed if one of the warning levels is located as close as possible to the stability limit. For this reason, the objective is to verify whether there exists one particular axial position where this need is most satisfied. Giving a recommendation for an optimized measurement position is just one objective of this section alongside providing another approach of assessing an imminent stall event based upon evaluating the axial pressure data simultaneously.

The parametric study is mainly motivated by RI's property of shifting the propagation area from downstream to upstream during throttling of the compressor. It is suggested that this dependency must also be mirrored in the skewness obtained at various axial locations. Only the static pressures recorded by the axially aligned transducer array have been considered. Each pressure has been monitored individually and the skewness has been calculated for every flow

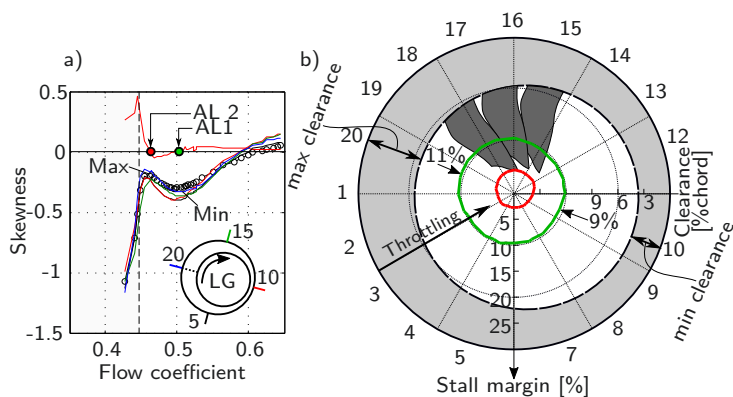


Figure 4.36: Absolute skewness as a function of flow coefficient / stall margin - left: average skewness from all 20 circumferential sensors and four selected skewness distributions from circumferential positions 5, 10, 15 and 20, right: circumferential skewness as a function of stall margin (minimum marks location of alarm level 1 "AL1", maximum corresponds to alarm level 2 "AL2"); eccentric LG rotor

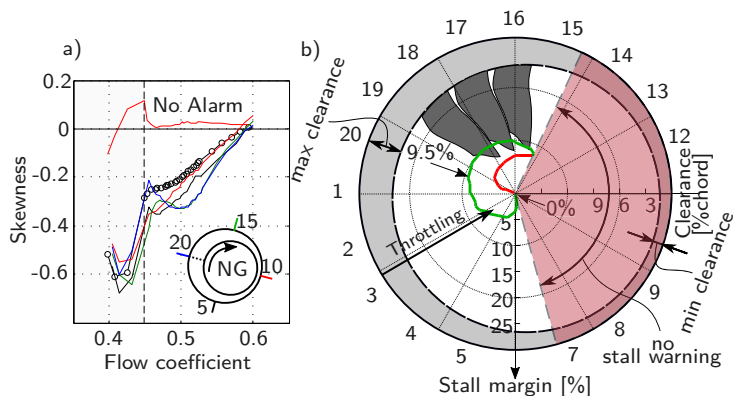


Figure 4.37: Absolute skewness as a function of flow coefficient / stall margin - left: average skewness from all 20 circumferential sensors and four selected skewness distributions from circumferential positions 5, 10, 15 and 20, right: circumferential skewness as a function of stall margin (minimum marks location of alarm level 1 "AL1", maximum corresponds to alarm level 2 "AL2"); eccentric NG rotor

coefficient at which measurements were obtained. Investigations begin with the concentric LG rotor.

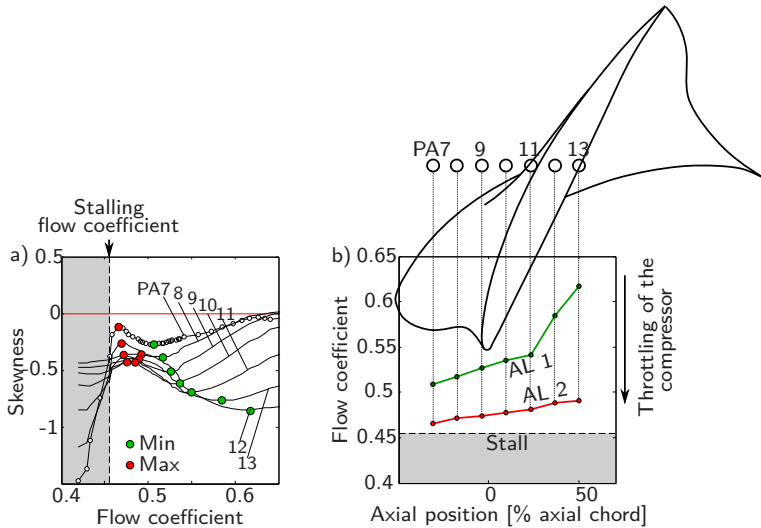


Figure 4.38: Flow coefficient dependent skewness for different axial measurement positions; concentric LG rotor

The series of skewness distributions in figure 4.38 a) are representing the axial positions from PA7 up to PA13. Only the flow coefficients corresponding to the warning levels have been read out from this series and then transferred into subfigure 4.38 b). Here, the operating range is displayed on the y-axis while throttling of the compressor is from top to bottom. Between 25% axial chord upstream and downstream of the leading edge, each warning level is linearly drifting away from the stability limit. While approaching 50% axial chord, the first stall warning (AL1) is provided in the almost unthrottled state, however, AL2 still triggers close to the stall limit. In the next step, all pressures have been post-processed individually again. However, this time, at each flow coefficient the relative skewness has been computed by applying the phase-averaging procedure presented in section 4.1.2. Figure 4.39 a) shows the series of relative skewness for different axial locations. In contrast to the foregone analysis, the pressures can now be evaluated in the rotor reference frame allowing to appropriately track the forward shift of the propagation area of prestall disturbances. One particular distribution can be read as follows:

By focussing on PA13 which is at 50% axial rotor chord inside the passage there is a global minimum in the relative skewness distribution at about $\phi = 0.54$.

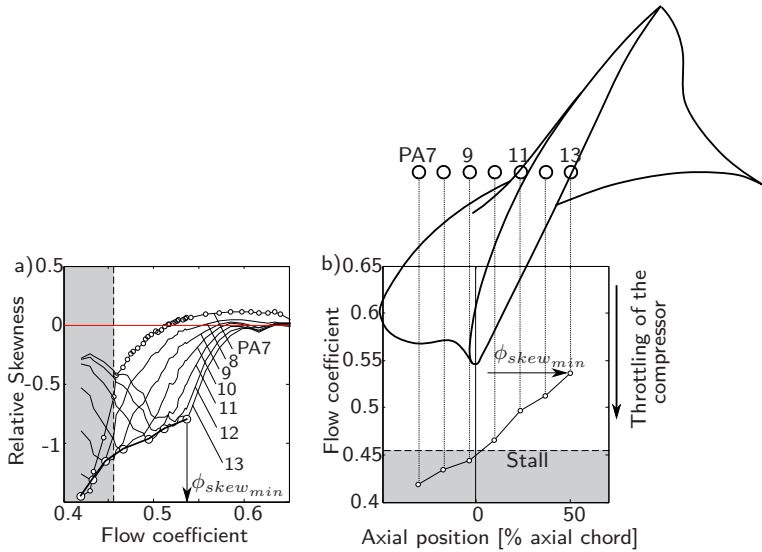


Figure 4.39: Flow coefficient dependent relative skewness for different axial measurement positions; concentric LG rotor

Considering that the level of relative skewness is indicating the intensity of negative pressure peaks, then the logical assumption is that the prestall disturbances are most pronounced at this position when the compressor is operating at $\phi = 0.54$. In other words, at $\phi = 0.54$ the trajectory of prestall flow disturbances is crossing the axial position PA13. In order to provide a clearer insight into this particular trend, the flow coefficients have been read out at each minimum and then transferred into subfigure 4.39 b) where the operating range is plotted against the axial coordinate. The almost linear distribution is clearly illustrating that the propagation area is continuously approaching the rotor inlet plane while throttling the compressor. The trajectory crosses the leading edge plane exactly at the moment stall occurs which has already been suggested in figure 4.21.

The NG configuration is examined equivalent to LG (see figure 4.40). Since the overall trends obtained for the LG setup also apply to the NG setup, the following analysis mainly focusses on the differences. Turning to subfigure 4.40 b), measuring the casing static pressures upstream of the leading edges provides only the first warning indicator (AL1) while AL2 lies on the stalling limit and is therefore inappropriate for reliable stall prevention. The second indicator (AL2) only comes apparent at stable compressor operation when considering

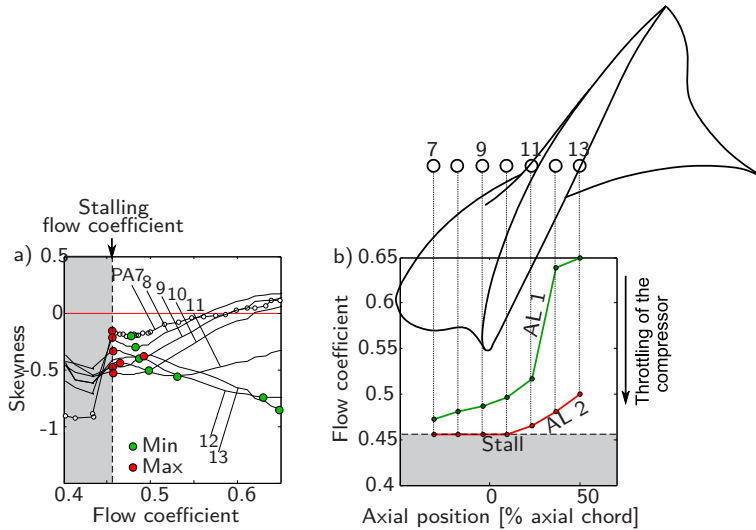


Figure 4.40: Flow coefficient dependent skewness for different axial measurement positions; concentric NG rotor

the measurement positions inside the rotor passage. Taking into account the results from the LG rotor, a reasonable recommendation would be to place the probe in closest proximity to the rotor inlet plane since the more conservative indicator (AL1) will at least be provided before entering into stall. Figure 4.41 b) shows that the feature of prestall disturbances crossing the leading edges in the moment of stall inception seems to be independent from the clearance size. Regarding the axial shift of disturbance propagation, the small clearance rotor appears to behave quite sensitively. While reducing the mass flow from top to bottom in subfigure 4.41 b), prestall disturbances arise close to the stability limit and from that point onwards their trajectory is very quickly displaced in the upstream direction.

The determination of stall warning indicators as presented in figures 4.38 b) and 4.40 b) based upon recording the casing static pressures within a certain operating range. One solution to overcome the need of running the whole speed line between open throttle and stall could be searching for the position of minimum relative skewness within the passage as shown in figure 4.41 b). If the minimum is about to cross the rotor inlet plane, then stall is imminent. However, this approach requires several sensors to be measuring the static wall

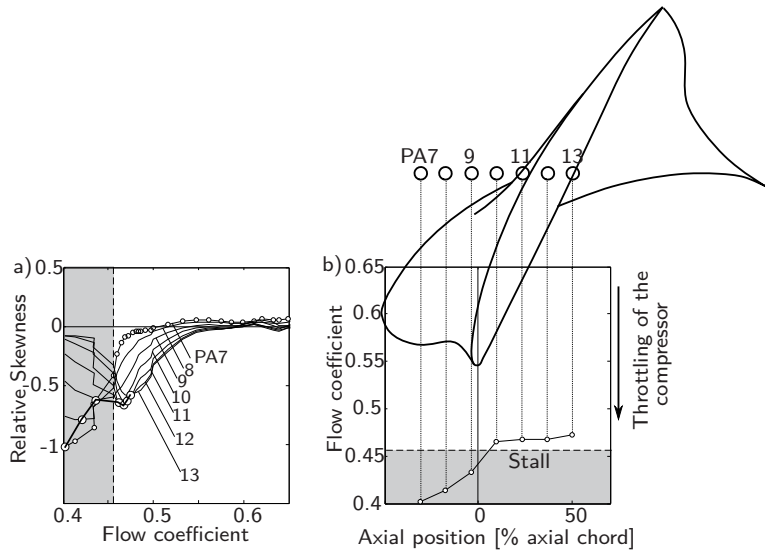


Figure 4.41: Flow coefficient dependent relative skewness for different axial measurement positions; concentric NG rotor

pressures along the axial chord simultaneously at high temporal and spatial resolution.

4.11 Conclusions

1. A new wind tunnel has been designed for the purpose of investigating the prestall phenomenon Rotating Instability (RI). A high concentration of instrumentation over the rotor blade tips was used to improve the physical understanding of RI. The investigations clearly demonstrated the importance of considering the area upstream of the rotor leading edges to provide an overall picture of the propagation mechanism of RI.
2. It was found that the inception of RI depends on both, clearance size and rotor eccentricity. The bigger the clearance, the earlier the prestall instability RI is initiated while throttling the compressor. When comparing a concentric rotor against an eccentric and both compressors having the same average clearance size, then the eccentric compressor is prone to suffering from RI first. If the clearance is nonaxisymmetric, the maximum level of tip gap height appears to be determining the inception of RI almost equal to an axisymmetric compressor with the same average clearance.
3. In an eccentric compressor there exists a large variation in the spectral signature of RI around the whole annulus. Also, there is a phase lag between the maximum clearance and the location of highest pressure fluctuations induced by RI. The measure of this displacement depends on the throttle setting of the compressor.
4. The prestall phenomenon RI is characterized by discrete flow disturbances mostly propagating in the forward half of the rotor passage. While reducing the mass flow through the compressor, the trajectory of prestall flow disturbances is successively shifted in the upstream direction. In the casing static pressure contour, the disturbances appear as patches of intense low pressure most likely arising in the interface between the main flow and the tip clearance vortex. In this regard, it is reasonably assumed that the aerodynamic disturbances of RI represent the disturbances of a Kelvin-Helmholtz-Instability.
5. It was found, that the local patches of intense low pressure can be actually seen as part of a much broader prestall flow structure circumferentially skewed and reaching up to almost 100% axial rotor chord upstream of the rotor inlet plane.

6. The propagation speed of the prestall flow disturbances is about 40 % of the rotor speed. The propagation speed increases linearly with decreasing flow coefficient, where the speed seems to be independent of the average clearance size.
7. Statistical investigations have shown that the circumferential count of prestall flow disturbances is continuously changing at a fixed throttle setting. The very circumferential count corresponding to the peak within the spectral signature having largest pressure amplitudes appears to be arising the most often over time.
8. After the onset of stall, the flow disturbances of RI might get into interaction with stall cell structures. In the present setup, the propagation speeds of stall cells and RI disturbances are clearly differing from each other, where the cell speed is lower compared to the one from RI disturbances. The inevitably overtaking is characterized by disturbances of significantly increased pressure amplitudes being relocated upstream of the cells.
9. Stall inception with RI present beforehand appears to be depending on the propagation area of prestall flow disturbances. Once any of the aerodynamic disturbances succeed in entering the neighboring passage for the first time, stall is initiated. Prestall flow disturbances are adopting the physical mechanism of the classical spike type stall inception at this specific instant.
10. Prestall flow disturbances are leaving a distinctive pattern in the blade passing signature of the rotor blades. An intriguing approach would be to take advantage of the prestall features changing while approaching the stability limit of the compressor. Given a time-resolved pressure recorded near the rotor tip leading edge and applying the third statistical moment (skewness) to the data, allows to define concrete stall warning indicators. When plotting the skewness against the flow coefficient, at least one critical point can be seen in the distribution well before stall onset. These critical points can be used for triggering an alarm. It has been shown that the margin between the trigger and the stability limit depends on the clearance size that is why the stall warning system is offering the potential for assessing the deterioration in tip gap height as part of an engine health monitoring system.

5

Discussion and Recommendation for Future Work

The present chapter discusses the physical propagation mechanism of RI in the light of observations made in both setups including suggestions for future research to further investigate the inception mechanism of RI.

Comprehensive instrumentation was used in the stator to acquire the intriguing flow pattern of RI at high temporal and spatial resolution in the physical location of most interest. That is implicitly why the parameter space had to be limited to an operating point with most pronounced prestall activity. However, discrete low pressure spots have been found to originate at the same location in the stator as in the rotor. This link has been used to study the behavior of prestall disturbances in the rotor during gradually throttling the compressor.

A special triggering method helped identify patches of intense low pressures propagating in closest proximity to the stator leading edges, however, predominantly located inside the passage. Using novel instrumentation, namely the unsteady sublayer fence probe, the low pressure spots could be explicitly linked to local vorticity which is assumed to be caused by an Inoue-type vortex (Inoue et al. (2002) [33]). Accordingly, the radial vortex is attached to the hub wall with one end and to the suction side surface of the blade with the other end while spanning across the leakage vortex. It can also be excluded that the unique approach of triggering modal events produces some kind of artificial flow structures since triggering on mere negative pressure peaks led to the same pattern of vorticity formation and decay within a single passage (see Eck et al. (2019) [21]).

Generally, a continuous propagation from one passage to the next was found without any vortex itself entering into the neighboring passage. In detail, the trajectory of prestall vortices originates near the stator leading edge and terminates at the leading edge pressure side of the adjacent blade. Using the path of minimum skewness in the skewness contour plots phase-locked to the rotor, a very similar trajectory could be tracked in the rotor operating close to the stability limit. However, while operating at lower blade loadings, the origin of the trajectory is seen to be located far off the blade leading edge suggesting that a leading edge separation *cannot* be the cause of prestall disturbances. If the latter was true, the trajectory would always originate from the leading edge at any operating point. A more logical conclusion is that prestall disturbances result from the shear layer between the main flow and the clearance flow becoming destabilized. Such an assumption is difficult to prove, though. Taking into account the idea of shear layer instabilities nonetheless, a propagation from one passage to the next could be explained as follows:

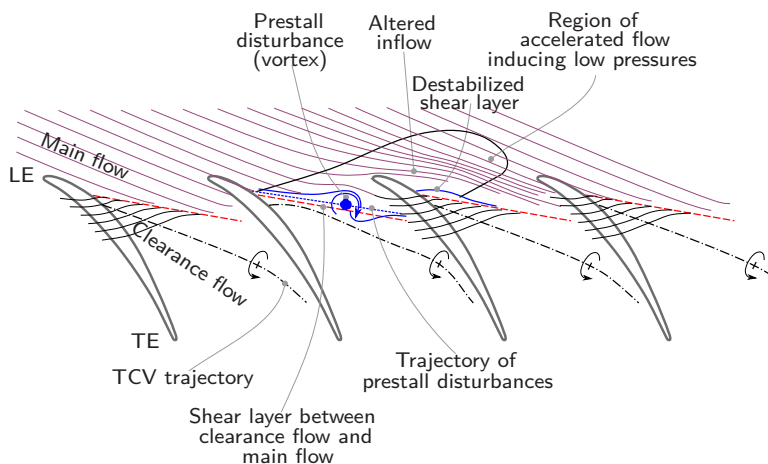


Figure 5.1: Schematic illustration of the propagation mechanism of RI

Given a prestall vortex approaching the neighboring blade, the inflow is most likely prevented from entering into the passage in which the prestall vortex has formed. Instead, the incoming main flow is redirected to the neighboring passage (see figure 5.1). Right here, the altered inflow is ascribed to be destabilizing the shear layer between the main flow and the clearance flow leading to the formation of a new prestall vortex. This process is repeated around the annulus without triggering the inception of rotating stall at any time. Assumptions about the flow redirection can be properly confirmed by investigations carried out in the rotor. The casing static pressure contours from which the average blade passing signal has been removed provide a clear hint on this. Skewed areas of negative static pressures were seen to be located upstream of the rotor inlet plane while always being flushed with the prestall vortices which on the contrary are located inside the rotor passages (see figure 4.24). The reasonable assumption is that the negative static pressures upstream of the rotor must have been induced by the redirected and thereby slightly accelerated inflow (illustrated in figure 5.1). Also, the skewed area was found to be reaching further upstream as the mass flow rate decreases (see figure 4.23). This trend could be explained as follows: The more the compressor is throttled, the further the TCV trajectory and thereby the trajectory of prestall vortices is being shifted in the upstream direction. Consequently, the vortex induced velocities of the prestall vortices have an increasing impact on the flow field ahead of the rotor.

Summarizing, figure 5.2 compares different operating points on the same speed line. The schematic illustration on the right side belongs to an operating

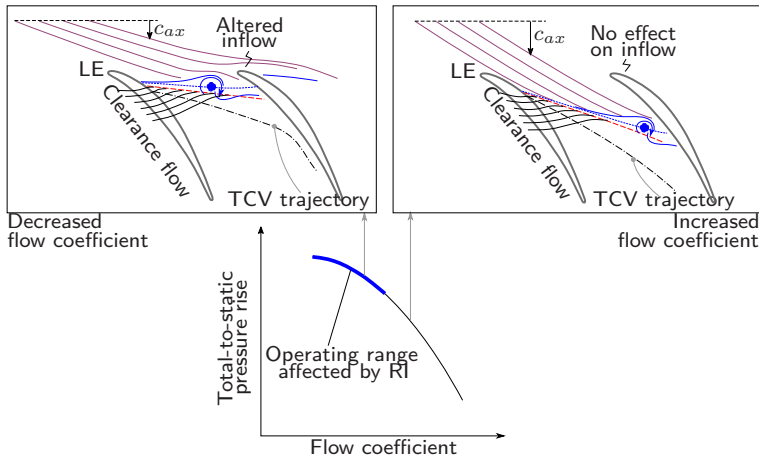


Figure 5.2: Development of RI while throttling of the compressor

point at an unthrottled state - the mass flow rate is comparatively high ($c_{ax} \uparrow$) and the TCV trajectory extends almost downstream. Even if the smallest disturbance forms within the interface, it has no effect on flow redistribution - any propagation is suppressed and no prestall instability is recognized. (This case can be considered to be very similar to the operating point presented in figure 4.23 a)). Throttling of the compressor ($c_{ax} \downarrow$) is accompanied by a TCV being more and more aligned in tangential to the rotor inlet plane. Any arising disturbance is now able to proceed around the annulus using the incoming main flow as a physical transmission from one passage to the next - the compressor is now suffering from RI. A very similar behavior of propagating prestall disturbances applies to a rotor positioned off center. The different flow conditions shown in figure 5.2 can be found in the maximum or the minimum clearance sector respectively. An appropriate explanation on this requires to give a general background on compressor performance with a non-axisymmetric tip clearance by introducing the parallel compressor model by Graf et al. (1998) [2]. The basic idea is that the operating point of an eccentric compressor can be resembled by two equivalent compressors each having an average clearance equal to the maximum and minimum clearance respectively.

In an eccentric compressor the pressure rise is physically constrained to be constant around the whole annulus. A concentric compressor with a clearance equal to the maximum gap, however, will provide a lower pressure rise than the one with the smaller clearance. Consequently, the inflow is being redistributed

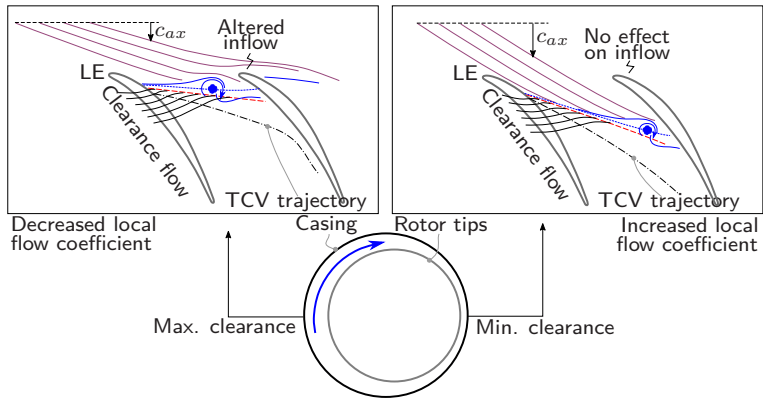


Figure 5.3: Progression of RI in an eccentric rotor

to fulfill the forgone requirement of constant pressure rise leading to a lower flow coefficient in the large clearance sector and a higher flow coefficient in the small clearance sector. This trend is basically represented by the varying flow velocities c_{ax} in figure 5.3. As a result, the large clearance sector complies with the boundary conditions necessary for the propagation mechanism of RI. In the minimum clearance sector, any propagation is suppressed by any disturbances migrating downstream. Transitioning towards the maximum clearance, a gradual formation of RI must be observed. This leads to a valuable conclusion:

Studying the inception of RI during transient throttling appears to be almost impossible since the circumferential position showing any first sign of propagating prestall disturbances is most likely changing from run to run. Without having vast instrumentation with high spatial resolution at least covering the entire circumference, studying the inception of RI is like searching for a needle in a haystack. One solution to overcome this challenge and to precisely capture the physical inception mechanism of RI in a strategic manner is to use an eccentric compressor. Taking into account the results presented in figure 4.18, the spectral signature of RI was seen to develop in a specific sector some 90 deg before reaching the maximum clearance. A recommendation for future research into RI inception would be to place concentrated over-tip instrumentation in this specific area.

A

Appendix

Contents

A.1	Analysis methods	124
A.1.1	Frequency Analysis	124
A.1.2	Mode Analysis	125
A.1.3	Statistics	125
A.2	Additional figures	127

A.1 Analysis methods

A.1.1 Frequency Analysis

A Fourier Transformation allows for converting a continuous signal (e.g. pressure $p(t_N)$) to the frequency domain. The approach helps identify spectral pattern caused by any periodical, deterministic or random fluctuation. Given a signal $p(t)$ that can be integrated, the Fourier Transform accords to:

$$p(f_m) = A_m(f) = \Delta t \sum_{n=0}^{N-1} p(t_N) e^{-i\Pi \frac{m n}{N}} \quad (\text{A.1})$$

Commonly, the Fourier series is transferred into the power spectral density (PSD) providing information about the energy content of a certain spectral component within an infinitesimal frequency range. For this, an auto-correlation is applied to the Fourier Transform in the form that $p(f_m)$ is being multiplied by its conjugated complex $p^*(f_m)$:

$$PSD_{xx} = \frac{2}{T} |p(f_m)|^2 = \frac{2}{T} p_x^*(f_m) p_x(m) \quad (\text{A.2})$$

The coherence function γ^2 provides information of how much a specific frequency component of two continuous signals do correlate. Using the auto- and cross spectra obtained from two signals measured at different locations, the coherence function accords to:

$$\gamma_{xy}^2 = \frac{|PSD_{xx}|^2}{PSD_{xx} PSD_{xy}} \quad (\text{A.3})$$

Further to this, the phase angle φ_{xy} answers the question about the relative phase lag between the frequency components considered for processing the coherence. The phase angle can be calculated by the corresponding imaginary and real part of the power spectral density function:

$$\varphi_{xy} = \text{atan} \frac{\text{Im}(PSD_{xy})}{\text{Re}(PSD_{xy})} \quad (\text{A.4})$$

A.1.2 Mode Analysis

Given a ring of evenly distributed pressure transducers at a count of j , an azimuthal mode analysis is feasible up to mode orders $m = j/2 - 1$. Equivalent to a Fourier Transformation each pressure signal $\tilde{p}(\varphi_j, t)$ measured at a certain annular position φ_j , can be expressed through an integral over the frequencies ω :

$$\tilde{p}(\varphi_j, t) = \int_{-\infty}^{\infty} p(\varphi_j, \omega) \cdot e^{i\omega t} d\omega \quad (\text{A.5})$$

Accordingly, the frequency-dependent pressure signal $p(\varphi_j, \omega)$ is represented by the sum of azimuthal modes of order m having an amplitude of $A_m(\omega)$:

$$p(\varphi_j, \omega) = \sum_{m=-\infty}^{\infty} A_m(\omega) \cdot e^{im\varphi_j} \quad (\text{A.6})$$

Applying a least-square-fit based on the cross spectral matrix of azimuthal mode amplitudes to the data $p(\varphi_j, \omega)$ delivers the frequency dependent mode amplitudes $A_m(\omega)$. To properly investigate the time-resolved mode amplitudes, a spatial discrete Fourier Transformation (DFT) needs to be applied to the real part of $\tilde{p}(\varphi_j, t)$, according to:

$$\tilde{A}_m(t) = \frac{1}{N_\varphi} \sum_{j=0}^{N_\varphi-1} \tilde{p}(\varphi_j, t) \cdot e^{-im\varphi_j} \quad (\text{A.7})$$

The auto-correlation technique can be carried out for the time-resolved mode amplitudes to obtain the unique "modal events".

A.1.3 Statistics

Given a continuous pressure signal $p(t)$ sampled at discrete points in time t , the Reynolds decompositions allows for decomposing the signal into its mean value \bar{p} and its fluctuation part p' , according to:

$$p(t) = \bar{p} + p' \quad (\text{A.8})$$

where the arithmetic mean can be calculated by using

$$\bar{p} = \lim_{N \rightarrow \infty} \frac{1}{N} \sum_{i=1}^N p_i(t). \quad (\text{A.9})$$

The root mean square (RMS) being the square root of the variance (Var) is a common tool for assessing the quantity of any pressure deviating from its arithmetic mean value. Here, the variance, also known as the second statistical moment, provides information about the broadness of the probability distribution. The RMS accords to:

$$RMS = \sqrt{Var} = \sqrt{\frac{1}{N-1} \sum_{i=1}^N [p(t) - \bar{p}]^2} \quad (A.10)$$

The third statistical moment, also referred to as the skewness (S), quantifies the asymmetry of the probability distribution. Since the tail can be located on the left or the right side of the mean, the skewness can therefore be positive or negative. If the signal contains pressure values being significantly smaller than the arithmetic mean, the skewness becomes negative ($S < 0$) - the opposite is true for a positive skewness ($S > 0$). In fluid mechanics, the skewness has widely been used successfully for assessing shear layers and helps locate the boundary layer transition. The skewness is being defined as:

$$S = \frac{1}{N} \sum_{i=1}^N \frac{[p(t) - \bar{p}]^3}{RMS^3} \quad (A.11)$$

A.2 Additional figures

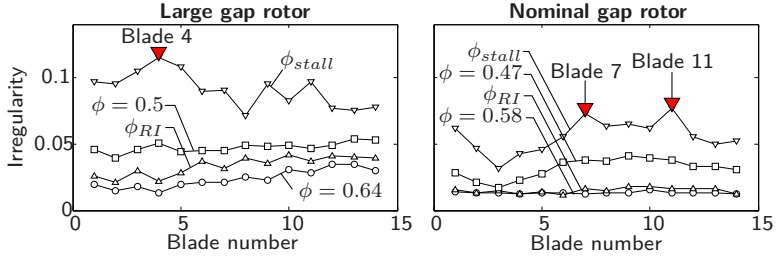


Figure A.1: Passage-to-passage variation of Irregularity for selected flow coefficients

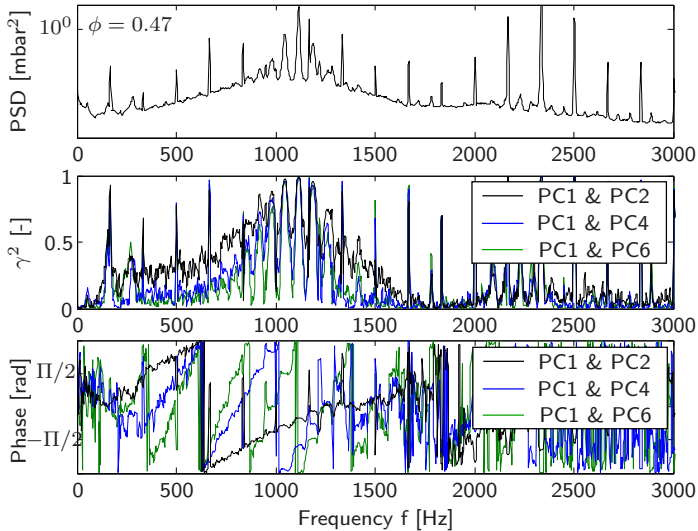


Figure A.2: Fourier transforms, coherence and phase spectra for three selected combinations from the circumferential pressure transducers; LG at $\phi = 0.47$

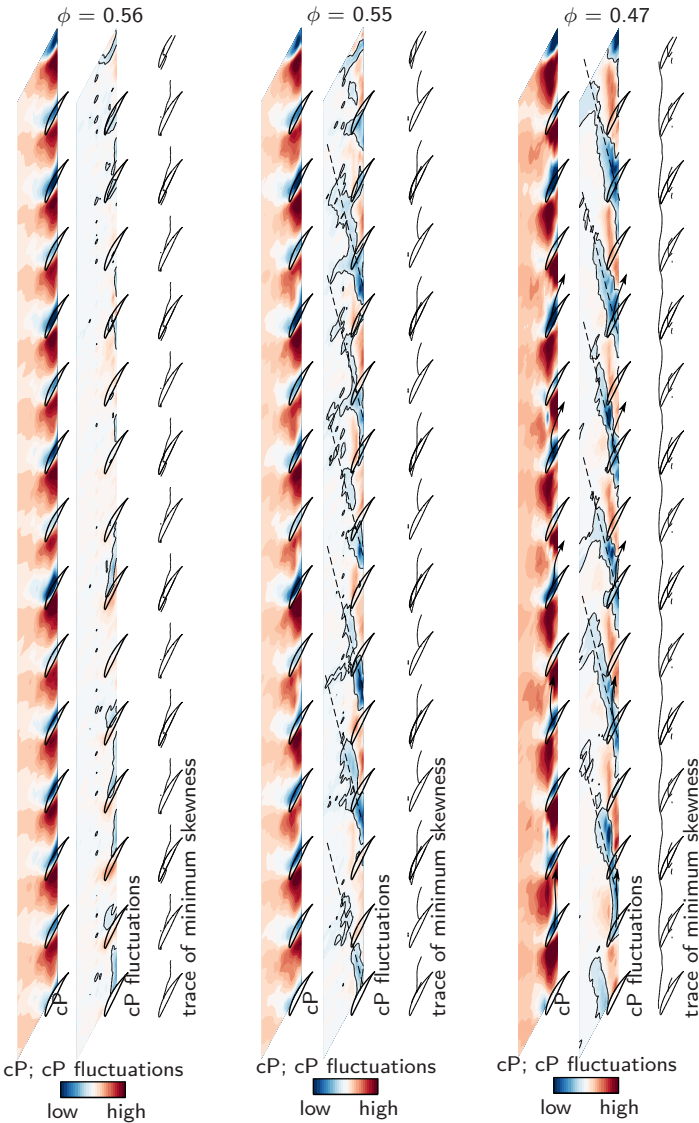


Figure A.3: Quasi-instantaneous static pressure contours and trajectories of negative skewness; concentric LG rotor

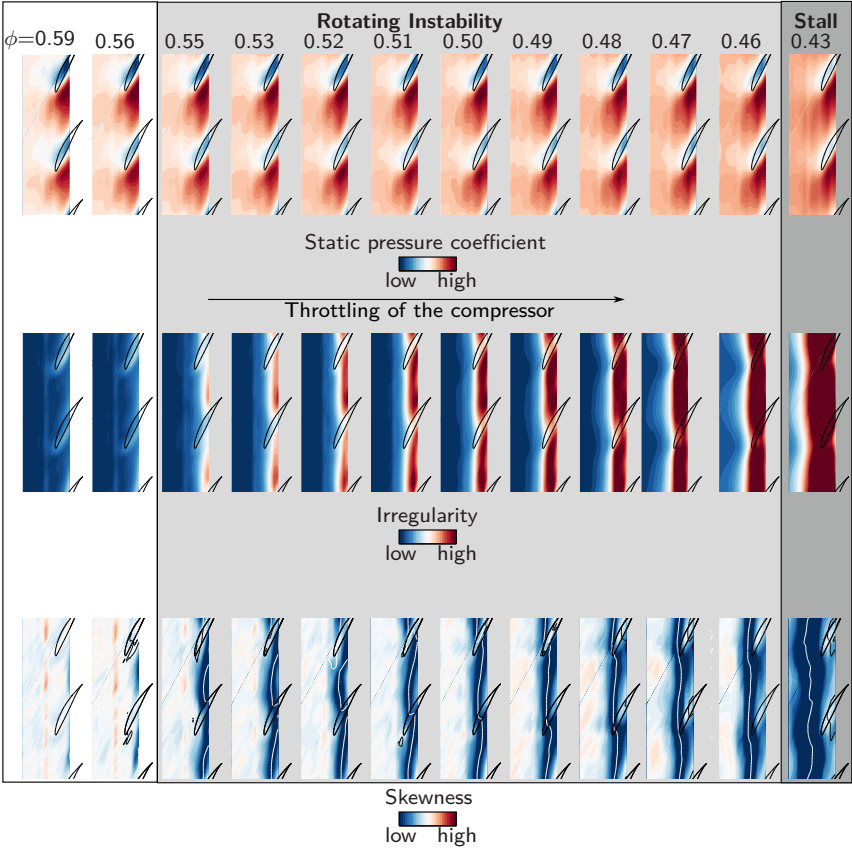


Figure A.4: Phase-averaged static pressure contours on the casing wall, irregularity and relative skewness; concentric LG rotor

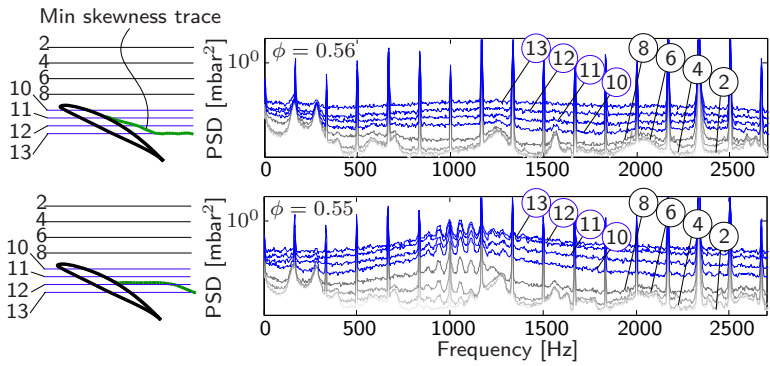


Figure A.5: Fourier analysis at various axial locations at an operating point without RI ($\phi = 0.56$) and at RI inception ($\phi = 0.55$), concentric LG rotor

Bibliography

-
- [1] M. A. Bennington, J. Cameron, S. C. Morris, C. Legault, S. T. Barrows, J.-P. Chen, G. S. McNulty, and A. Wadia. Investigation of tip-flow based stall criteria using rotor casing visualization. *ASME Conference Proceedings*, 01 2008. doi: 10.1115/GT2008-51319.
 - [2] M. B. Graf, T. S. Wong, E. Greitzer, F. E. Marble, C. S. Tan, H.-W. Shin, and D. C. Wisler. Effects of non-axisymmetric tip clearance on axial compressor performance and stability. *ASME Journal of Turbomachinery*, 120, 10 1998. doi: 10.1115/1.2841774.
 - [3] C. Beselt. *Experimentelle Untersuchung von Sekundärströmungsphänomenen in einer Verdichter-Stator-Kaskade*. PhD Thesis, Technische Universität Berlin, epubli, October 2016.
 - [4] C. Beselt, B. Pardowitz, R. Rennings, R. Sorge, D. Peitsch, L. Enghardt, F. Thiele, K. Ehrenfried, and P. U. Thamsen. Influence of the clearance size on rotating instability in an axial compressor stator. *10th European Conference on Turbomachinery Fluid Dynamics and Thermodynamics, ETC 2013*, 04 2013.
 - [5] C. Beselt, D. Peitsch, R.v. Rennings, and F. Thiele. Impact of hub clearance on endwall flow in a highly loaded axial compressor stator. *Turbo Expo: Power for Land, Sea, and Air*, Volume 6C: Turbomachinery, 2013. doi: 10.1115/GT2013-95463.
 - [6] C. Beselt, R. Rennings, D. Peitsch, F. Thiele, and K. Ehrenfried. Experimental and numerical investigation of the unsteady endwall flow in a highly loaded axial compressor stator. *Proceedings of the ASME Turbo Expo*, 2, 06 2014. doi: 10.1115/GT2014-25944.
 - [7] M. Binner and J. Seume. Flow patterns in high pressure steam turbines during low-load operation. *Journal of Turbomachinery*, 136:061010, 06 2013. doi: 10.1115/1.4025162.
 - [8] C. Brandstetter, M. Juengst, and H.-P. Schiffer. Measurements of radial vortices, spill forward and vortex breakdown in a transonic compressor. *ASME Journal of Turbomachinery*, 140, 01 2018. doi: 10.1115/1.4039053.
 - [9] J. C. R. Hunt, A. Wray, and P. Moin. Eddies, streams, and convergence zones in turbulent flows. *Proceedings of the 1988 CTR Summer Program*, 2:193–208, 1988.
 - [10] T. Camp and I. J. Day. A study of spike and modal stall phenomena in a low-speed axial compressor. *ASME Journal of Turbomachinery*, 120, 07 1998. doi: 10.1115/97-GT-526.

- [11] G.-T. Chen. *Vortical structures in turbomachinery tip clearance flows*. PhD Thesis, Massachusetts Institute of Technology (MIT), 1991.
- [12] J.-S. Choi, D. McLaughlin, and D. Thompson. Experiments on the unsteady flow field and noise generation in a centrifugal pump impeller. *Journal of Sound and Vibration - J SOUND VIB*, 263:493–514, 06 2003. doi: 10.1016/S0022-460X(02)01061-1.
- [13] D. Christensen, P. Cantin, D. Gutz, P. N. Szucs, A. R. Wadia, J. Armor, M. Dhingra, Y. Neumeier, and J. V. Prasad. Development and demonstration of a stability management system for gas turbine engines. *ASME Journal of Turbomachinery*, 130, 03 2008.
- [14] N. A. Cumpsty. *Compressor Aerodynamics*. Number 10. Krieger Pub., 2004. ISBN 9781575242477.
- [15] R. Dambach and H. Hodson. A new method of data reduction for single-sensor pressure probes. *Proceedings of the ASME Turbo Expo*, 4, 06 1999. doi: 10.1115/99-GT-304.
- [16] I. Day. Stall, surge and 75 years of research. *ASME Journal of Turbomachinery*, 138, 08 2015. doi: 10.1115/1.4031473.
- [17] I. J. Day and N. A. Cumpsty. The measurement and interpretation of flow within rotating stall cells in axial compressors. *Journal of Mechanical Engineering Science*, 20(2):101–114, 1978. doi: 10.1243/JMES_JOUR_1978_020_017_02.
- [18] J. D. Denton. Loss mechanisms in turbomachines. *ASME Journal of Turbomachinery*, 115:4, 10 1993. doi: 10.1115/93-GT-435.
- [19] A. Deppe, H. Saathoff, and U. Stark. Spike-type stall inception in axial-flow compressors. Proceedings of the 6th European Conference on Turbomachinery, Lille, France, 03 2005.
- [20] M. Dhingra, Y. Neumeier, and J. Prasad. Stall and surge precursors in axial compressors. *AIAA 2003-4425*, 2003.
- [21] M. Eck, R. Rückert, and D. Peitsch. Advanced application of a sublayer fence probe in highly instationary turbomachinery flows: observations on prestall instabilities. *Experiments in Fluids*, 60, 03 2019. doi: 10.1007/s00348-019-2686-5.
- [22] H. Emmons, C. Pearson, and H. Grant. Compressor stall and surge propagation. *ASME 53-A-65; Trans. ASME*, 77, 1955.
- [23] J. R. Foley. Compressor surge topic at sae round table. *SAE Journal*, 59:46–50, 09 1951.

- [24] M. Furukawa, M. Inoue, K. Saiki, and K. Yamada. The role of tip leakage vortex breakdown in compressor rotor aerodynamics. *ASME Journal of Turbomachinery*, 121, 07 1999. doi: 10.1115/1.2841339.
- [25] N. Gourdain, S. Burguburu, F. Leboeuf, and G. Jean Michon. Simulation of rotating stall in a whole stage of an axial compressor. *Computers and Fluids*, 39: 1644–1655, 10 2010. doi: 10.1016/j.compfluid.2010.05.017.
- [26] V. H. Garnier, A. H. Epstein, and E. Greitzer. Rotating waves as a stall inception indication in axial compressors. *ASME Journal of Turbomachinery*, 113, 04 1991. doi: 10.1115/1.2929105.
- [27] H. Hoenen and H.-E. Gallus. Monitoring of aerodynamic load and detection of stall in multistage compressors. *ASME Journal of Turbomachinery*, 117, 1995.
- [28] F. Holzinger, F. Wartzek, H.-P. Schiffer, S. Leichtfuss, and M. Nestle. Self-excited blade vibration experimentally investigated in transonic compressors: Acoustic resonance. *ASME Journal of Turbomachinery*, 138, 11 2015. doi: 10.1115/1.4032042.
- [29] D. A. Hoying, C. S. Tan, H. Vo, and E. Greitzer. Role of blade passage flow structures in axial compressor rotating stall inception. *ASME Journal of Turbomachinery*, 121, 10 1999. doi: 10.1115/1.2836727.
- [30] T. Hynes and E. Greitzer. A method for assessing effects of circumferential flow distortion on compressor stability. *ASME Journal of Turbomachinery*, 109, 08 1987. doi: 10.1115/1.3262116.
- [31] M. Inoue, M. Kuroumaru, T. Iwamoto, and Y. Ando. Detection of a rotating stall precursor in isolated axial flow compressor rotors. *ASME Journal of Turbomachinery*, 113, 04 1991. doi: 10.1115/1.2929102.
- [32] M. Inoue, M. Kuroumaru, T. Tanino, and M. Furukawa. Propagation of multiple short-length-scale stall cells in an axial compressor rotor. *ASME Journal of Turbomachinery*, 122, 01 2000. doi: 10.1115/1.555426.
- [33] M. Inoue, M. Kuroumaru, S. Yoshida, and M. Furukawa. Short and long length-scale disturbances leading to rotating stall in an axial compressor stage with different stator/rotor gaps. *ASME Journal of Turbomachinery*, 124, 07 2002. doi: 10.1115/1.1458022.
- [34] T. Iura and W. Rannie. Experimental investigation of propagating stall in axial-flow compressors. *ASME 53-SA-69; Trans. ASME*, 76, 1954.
- [35] I. J. Day. Stall inception in axial flow compressors. *ASME Journal of Turbomachinery*, 115, 01 1993. doi: 10.1115/1.2929209.

- [36] I. J. Day, E. Greitzer, and N. A. Cumpsty. Prediction of compressor performance in rotating stall. *Journal of Engineering for Power*, 100:1, 01 1978. doi: 10.1115/1.3446318.
- [37] A. Jackson. Stall cell development in an axial compressor. *ASME Journal of Turbomachinery*, 109, 1986.
- [38] M. Jüngst, F. Holzinger, H.-P. Schiffer, and S. Leichtfuss. Analysing non-synchronous blade vibrations in a transonic compressor rotor. *11th European Conference on Turbomachinery Fluid Dynamics and Thermodynamics, ETC 2015*, 01 2015.
- [39] F. K. Moore. A theory of rotating stall of multistage axial compressors: Part 1 - small disturbances. *Journal of Engineering for Gas Turbines and Power*, 106, 04 1983. doi: 10.1115/1.3239565.
- [40] F. K. Moore and E. Greitzer. A theory of post-stall transients in axial compression systems: Part 1 - development of equations. *Journal of Engineering for Gas Turbines and Power*, 108, 04 1985. doi: 10.1115/1.3239887.
- [41] F. Kameier. *Experimentelle Untersuchung zur Entstehung und Minderung des Blattspitzen-Wirbellärms axialer Strömungsmaschinen*. PhD Thesis, VDI-Verlag, 1994.
- [42] K. L. Suder and M. L. Celestina. Experimental and computational investigation of the tip clearance flow in a transonic axial compressor rotor. *ASME Journal of Turbomachinery*, -1, 07 1995. doi: 10.1115/1.2836629.
- [43] N. M. McDougall, N. A. Cumpsty, and T. Hynes. Stall inception in axial compressors. *ASME Journal of Turbomachinery*, 112:116–123, 01 1990. doi: 10.1115/1.2927406.
- [44] R. Mailach, I. Lehmann, and K. Vogeler. Rotating instabilities in an axial compressor originating from the fluctuating blade tip vortex. *ASME Journal of Turbomachinery*, 123, 07 2001. doi: 10.1115/1.1370160.
- [45] K. Mathioudakis and F. A. E. Breugelmans. Development of small rotating stall in a single stage axial compressor. page V001T03A064, 03 1985. doi: 10.1115/85-GT-227.
- [46] N. M. McDougall. *Stall inception in axial flow compressors*. PhD Thesis, University of Cambridge, 1988.
- [47] W. Nitsche and A. Bruun. *Strömungsmesstechnik*, volume 2. Springer-Verlag Berlin Heidelberg, 2006. doi: 10.1007/3-540-20990-4.
- [48] International Standard Organization. Industrial fans - performance testing using standardized airways. ISO 5801:2017, 2017.

- [49] B. Pardowitz. *Rotierende Instabilität in Axialverdichtern: Experimentelle Evaluation einer neuen Entstehungshypothese*. PhD Thesis, Technische Universität Berlin, DLR Forschungsbericht DLR-FB-2018-08, 2018.
- [50] B. Pardowitz, U. Tapken, and L. Enghardt. Time-resolved rotating instability waves in an annular cascade. *18th AIAA/CEAS Aeroacoustics Conference*, 06 2012. doi: 10.2514/6.2012-2132.
- [51] B. Pardowitz, A. Moreau, U. Tapken, and L. Enghardt. Experimental identification of rotating instability of an axial fan with shrouded rotor. *11th European Conference on Turbomachinery Fluid Dynamics and Thermodynamics*, 03 2015.
- [52] B. Pardowitz, U. Peter, J. and Tapken, P. U. Thamsen, and L. Enghardt. Visualization of secondary flow structures caused by rotating instability: Synchronized stereo high-speed piv and unsteady pressure measurements. 06 2015. doi: 10.2514/6.2015-2930.
- [53] B. Pardowitz, U. Tapken, L. Neuhaus, and L. Enghardt. Experiments on an axial fan stage: Time-resolved analysis of rotating instability modes. *Journal of Engineering for Gas Turbines and Power*, 137:062505, 06 2015. doi: 10.1115/1.4028686.
- [54] G. Pullan, A. M. Young, I. J. Day, E. Greitzer, and Z. Spakovszky. Origins and structure of spike-type rotating stall. *ASME Journal of Turbomachinery*, 137, 06 2012. doi: 10.1115/GT2012-68707.
- [55] T. Raitor and W. Neise. Sound generation in centrifugal compressors. *Journal of Sound and Vibration*, 314:738–756, 07 2008. doi: 10.1016/j.jsv.2008.01.034.
- [56] M. Schober, E. Obermeier, S. Pirskawetz, and H.-H. Fernholz. A mems skin-friction sensor for time resolved measurements in separated flows. *Experiments in Fluids*, 36(4):593–599, Apr 2004. ISSN 1432-1114. doi: 10.1007/s00348-003-0728-4. URL <https://doi.org/10.1007/s00348-003-0728-4>.
- [57] H. Schrapp. *Experimentelle Untersuchung zum Aufplatzen des Spaltwirbels in Axialverdichtern*. PhD Thesis, Technische Universität Carolo-Wilhelmina zu Braunschweig, 2008.
- [58] F. Truckenmüller. *Untersuchungen zur aerodynamisch induzierten Schwingungsanregung von Niederdruck-Laufschaukeln bei extremer Teillast*. PhD thesis, 01 2003.
- [59] H. Vo, C. S. Tan, and E. Greitzer. Criteria for spike initiated rotating stall. *ASME Journal of Turbomachinery*, 130, 01 2008. doi: 10.1115/1.2750674.
- [60] H. D. Vo. *Role of Tip Clearance Flow on Axial Compressor Stability*. PhD Thesis, MIT, Cambridge, MA, May 2001.

-
- [61] S. Weichert. *Tip clearance flows in axial compressors: Stall inception and stability enhancement*. PhD thesis, University of Cambridge, 09 2011.
- [62] S. Weichert and I. Day. Detailed measurements of spike formation in an axial compressor. *ASME Journal of Turbomachinery*, 136, 06 2012. doi: 10.1115/GT2012-68627.
- [63] D. C. Wisler. Loss reduction in axial-flow compressors through low-speed model testing. *ASME Journal of Engineering for Gas Turbines and Power*, 107:354–363, 2 1985. doi: 10.1115/1.3239730.
- [64] A. Young, I. Day, and G. Pullan. Stall warning by blade pressure signature analysis. *ASME Journal of Turbomachinery*, 135, 01 2011. doi: 10.1115/GT2011-45850.
- [65] A. Young, T. Cao, I. J. Day, and J. P. Longley. Accounting for eccentricity in compressor performance predictions. *ASME Journal of Turbomachinery*, 139: 091008–091008–10, 9 2017. doi: 10.1115/1.4036201.